Transport under coordinate-dependent diffusion: An Itô Perspective

विद्या वाचस्पति की
उपाधि की अपेक्षाओं की आंशिक पूर्ति में प्रस्तुत शोध प्रबंध

A thesis submitted in partial fulfillment of the requirements of the degree of Doctor of Philosophy

द्वारा / By
मयंक शर्मा / Mayank Sharma
पंजीकरण सं. / Registration No.: 20172027

शोध प्रबंध पर्यवेक्षक / Thesis Supervisor:
प्रो. अरिजीत भट्टाचार्य / Prof. Arijit Bhattacharyay

भारतीय विज्ञान शिक्षा एवं अनुसंधान संस्थान पुणे

INDIAN INSTITUTE OF SCIENCE EDUCATION AND RESEARCH PUNE

2025

Dedicated to My beloved Parents, Grandparents and Sister.

Declaration

I declare that this written submission represents my ideas in my own words and where others' ideas have been included, I have adequately cited and referenced the original sources. I declare that I have acknowledged collaborative work and discussions wherever such work has been included. I also declare that I have adhered to all principles of academic honesty and integrity and have not misrepresented or fabricated or falsified any idea/data/fact/source in my submission. I understand that violation of the above will be cause for disciplinary action by the Institute and can also evoke penal action from the sources which have thus not been properly cited or from whom proper permission has not been taken when needed.

The work reported in this thesis is the original work done by me under the guidance of Prof. Arijit Bhattacharyay.

Date: July 5, 2025

Mayank Sharma
Reg. No. 20172027

Certificate

Certified that the work incorporated in the thesis entitled "*Transport under coordinate-dependent diffusion: An Itô Perspective*", submitted by *Mayank Sharma* was carried out by the candidate, under my supervision. The work presented here or any part of it has not been included in any other thesis submitted previously for the award of any degree or diploma from any other university or institution.

Date: July 5, 2025

Prof. Arijit Bhattacharyay
Thesis Supervisor

Acknowledgements

First of all, I would like to thank the *Almighty God* who gave me *everything*. I believe without his blessings, nothing would have been possible. I thank him for watching over me and taking care of my health.

I express my deepest and most sincere gratitude towards Professor *Arijit Bhattacharyay* for giving me the opportunity to work with him. I feel very lucky to have a Supervisor like him who is not only brilliant, but also kind, understanding, and considerate. I have always enjoyed discussing Physics with him. He has been like a father figure to me. His calm and reassuring presence has always put me at ease. I will always remain grateful for the freedom he gave me to learn and grow, especially during the early years of my Ph.D. I deeply appreciate that he never responded with anger when I made mistakes, but instead reminded me that such things are a natural part of research, encouraging me to simply move forward and not repeat them. I can recall many instances during my Ph.D. when he has been a pillar of strength and support for me. His emphasis on clarity of thought, calmness and intellectual honesty has had a lasting impact on me, both as a researcher and as a person. I would also like to thank Prof. Santhanam and Prof. Apratim for their support and encouragement.

I owe a deep debt of gratitude to my grandparents and parents for the hard work and sacrifices they made throughout their lives, which laid the foundation for the opportunities I have today. My *Dadaji* lived a life marked by service and unwavering discipline. He served as a part of the *Azad Hind Fauj* in the war with courage and commitment, and despite the many struggles he faced, remained a strong, calm, and principled man throughout his life. His resilience and sense of duty have always inspired me deeply. My *Dadi*, a remarkably strong woman who held the family together through difficult times. She managed the household with quiet strength,

grace, and resilience, often making do with very little but never letting their children feel any lack.

I am especially grateful to my *father*, a deeply disciplined and principled man whose sacrifices and commitment to our education shaped my life. He devoted major part of his salary towards our education, never once thinking twice about it, because he firmly believed that education is the most powerful investment one can make in a child's future. He placed our learning and growth above all else, even at the cost of personal comfort. His quiet determination, tireless support, and belief in the transformative power of education have shaped not just my academic path, but also my values and sense of purpose. I owe a great deal of my life to his unwavering commitment and selflessness. I am equally thankful to my *mother*, whose cheerful spirit and gentle smile could lift the mood of any room. She has always been a joyful and caring presence, lightening even the most stressful moments with warmth and humour. Her ability to stay positive and keep the household balanced has been invaluable throughout my journey. I am also thankful to my *sister* for her support.

I would also like to thank my teachers from my school days. I am greatly indebted to *Rajeev sir*, whose classes not only sparked but continually nurtured my curiosity in physics. His encouragement during those early years played a pivotal role in shaping my interest in the subject and inspiring me to pursue it further. I am also grateful to *Narender Sir* for laying down foundations for my mathematics. I would also like to thank *Sameer* and *Siddharth sir*, who provided me with unwavering support. I have been truly fortunate to meet wonderful people throughout my journey. I am grateful to *Rajat Dev*, my school friend, whose early conversations about Physics sparked my interest in the subject. I also fondly remember my B.Sc. friends *Poorvi, Sanjeev, Rishabh, and Arpan* who brought laughter, mischief, and perspective during that formative phase. My sincere thanks to *Hemant sir, Sachin sir, Haldar sir*, and the physics lab staff at my college, whose encouragement left a lasting impression on me.

Life at IISER was unimaginable without the friendship and support of *Aakash, Sagar, Shaunak, Abhishek, Hitendra, Bittu, Tushar, Ritam, Ramya Narayan, Dipanshu, Sushant, Aanjaneya, Prajna, Sandipan Manna, Jitendra, Sandipan Mohanta, Rajeev, Abrar, Karan, Madhusudan, Projjwal, Prajjwal, Deep and Karthikeyan.* Their companionship made this journey vibrant and meaningful. A special thanks

to *Karthikeyan* for generously taking us to *JD (Juice destination)* in his car so many times over the course of this Ph.D. Those rides in his car meant a lot and created many cherished memories. A special mention to *Abhishek and Ritam* for their constant help with tough computational problems. I am grateful to *Aakash* for our discussions on Physics, which were always thought-provoking and encouraging.

Playing *Badminton* at IISER was more than just a sport, it was a source of joy, a way to unwind, unleash the masculinity by continuously smashing the shuttle, and a great way to connect with friends. I made many friends in the court. The evening matches and spontaneous games helped me stay balanced, sane, and energized, and many cherished memories were made on the court. It meant more than a sport in the end, it was a way to display self that with persistence, smart work one can improve. I am grateful to *Tushar*, my badminton partner at IISER, for spending so much time with me discussing psychology if sports, having long discussions on tactics, coming early mornings to coach me on holidays, and helping me improve the game. *Tushar* was a tactical genius with very strong analysis who used to see patterns and played very smartly often positioning himself exactly where the opponent was about to play, even before they hit the shot. He relied on 80 percent smart work and 20 percent hard work. I improved a lot thanks to his inputs and insights. I also sincerely thank *Diganta sir and Krishanpal sir* for teaching me badminton, playing with me, and setting an example of how a good person and a sportsperson carries themselves both in and out of court, with humility, kindness, and grace. I would like to thank *Sagar* because of whom I eventually started playing badminton. I would also like to thank *Aakash* for teaching me how to play doubles, revolutionize the way we play now at IISER by introducing the concept of flat drives, partner position, reply to services and a faster, more dynamic style. Playing this way brought a new excitement and rhythm to the game, making us feel like Professional players at times, even though we are not all. I am also thankful to him for his insightful inputs.

I would also like to express my gratitude to individuals whose work and character have deeply inspired me. I thank *late Shri Ratan Tata* for his exemplary service and unwavering commitment to the betterment of our country. His integrity and compassion are truly admirable. I am also grateful to *Prof. V. Balakrishnan* for his insightful and lucid lectures on Physics, especially Statistical Mechanics, which have shaped my understanding of the subject. I extend my thanks to *Prof. Jordan*

Peterson for his thought-provoking lectures on *personality and its transformation, maps of meaning*, the idea of strengthening the individual and having a discussion on the meaning of duty and responsibility. I would also like to thank *Khabib Nurmagomedov* for being a very good role model for young men. I would like to thank *Kento Momota, Tai Tzu-Ying, Hendra Setiawan, M.S. Dhoni* for being exemplary sportspersons, not only for their exceptional skills on the court (pitch) but also for their humility, grace, and kindness. Their sportsmanship, resilience, and quiet strength have deeply inspired me, reminding me that greatness is as much about character as it is about hard work and talent.

I am also thankful to the academic staff of IISER Pune especially *Sayali mam, Sneha mam, Nayana mam, Rohit sir, Ranjan sir, Swapnil sir, Dipali mam* for always helping me. I would also like to thank *Dhanashree mam, Prabhakar sir, Palash sir and the Department of Physics* for always being so caring and helpful.

Lastly, I gratefully acknowledges financial support from the CSIR-SRF-Direct fellowship (Grant No. 09/0936(18027)/2024-EMR-I). I would also like to express my deep gratitude to the countless freedom fighters of India, both celebrated and unsung, who made immense sacrifices for the nation's independence. Visionaries and revolutionaries such as *Subhas Chandra Bose, Lala Lajpat Rai, Bhagat Singh, Chandrashekhar Azad, Sardar Vallabhbhai Patel* along with innumerable unnamed individuals who laid the foundations of the free India in which we are able to pursue knowledge and scientific inquiry today. I sincerely thank them all for their courage, sacrifice, and enduring legacy. I also thank visionary leadership, *Shri Atal Bihari Vajpayee, Dr Manmohan Singh, and Dr A. P. J. Abdul Kalam*, whose commitment to science, education, and nation-building has profoundly shaped India's scientific and technological aspirations. I furthur express my sincere gratitude to the *Government of India*, the people of India, and the Hon'ble Prime Minister *Shri Narendra Modi* for their steadfast commitment to promoting and supporting basic scientific research. The support and the resources provided by Param Brahma Facility under the National Supercomputing Mission, Government of India, at the Indian Institute of Science Education and Research Pune, are gratefully acknowledged.

Mayank Sharma

"In sterquiliniis invenitur"
A powerful reminder that growth and discovery often require venturing into the uncomfortable, the avoided, and the unknown.

Contents

Abstract

Biological systems at micrometer scales and below often operate in crowded, highly viscous environments characterized by persistent stochastic thermal fluctuations. Diffusion is incessant and plays an important role in transporting these entities in crowded environments. The presence of membranes/pores and multiple biological entities in a constricted space can make the damping/diffusion inhomogeneous. This effect of inhomogeneity is presented by the diffusion becoming coordinate-dependent. Coordinate dependence of damping/diffusion arises near a boundary or interface due to the presence of slow hydrodynamic modes generated by thermal fluctuations of a Brownian particle. Existence of this coordinate/state dependence of damping/diffusion entails new physics for structured mesoscopic objects evolving through an Itô process under uncorrelated white-noise fluctuations of a heat bath.

In this thesis, we analyze the consequences of coordinate-dependent diffusion on Brownian systems within the Itô framework. We investigate how spatially varying damping, even in the absence of external driving or correlated noise, can give rise to rich and unexpected transport phenomena. We begin by studying a single Brownian dimer in one dimension with broken damping symmetry and demonstrate that sustained spontaneous directed motion can emerge purely from equilibrium fluctuations. We then extend this framework to a weakly non-equilibrium scenario, where a small external force is applied. In this case, we demonstrate that the symmetry-broken dimer can exploit thermal fluctuations to extract energy from the external drive. In the next part of our work, we move beyond the single-dimer case and examine the transport behavior of many-body systems composed of interacting dimers. We show that collective rectified spontaneous transport can arise purely from equilibrium fluctuations, driven by homogeneous, isotropic fluctuations of the bath in the presence of spatially varying damping/diffusion. Finally, we explore the thermodynamic implications of Itô-type evolution for mesoscopic objects in inhomogeneous

media and identify transient non-equilibrium mechanisms such as entropic pulling and the diffusion diode effect. This thesis offers new insights into how passive systems subject to spatial variation in diffusivity/damping in complex environments can generate effective transport without any active input when viewed through the Itô lens.

List of Publications

(i) Mayank Sharma and Arijit Bhattacharyay, *Conversion of heat to work: An efficient inchworm*, Physica Scripta, Volume **95**, Number (10) (2020).

(ii) Mayank Sharma and Arijit Bhattacharyay, *Spontaneous collective transport in a heat-bath*, Physica A: Statistical Mechanics and its Applications Volume **626**, 15 September 2023, 129082 (2023).

(iii) Mayank Sharma and Arijit Bhattacharyay, *Entropic pulling and diffusion diode in an Itô process*, Physics Letters A 553 (2025) 130709.

The supplementary visualization videos associated with this thesis are publicly available at the author's academic website: https://mayankandhouse.github.io

1

Introduction

The physical world operates across distinct yet interconnected length scales, each governed by its own set of principles. Understanding phenomena across these scales is central to fundamental physics and for technological applications. Broadly, physical behavior can be categorized into three regimes based on the characteristic length scales involved: *microscopic*, *mesoscopic*, and *macroscopic*.

Microscopic physics deals with phenomena at the scale of atoms and subatomic particles, typically below 10^{-9} meters. In this regime, the fundamental laws of quantum mechanics govern the behavior of matter. Systems are described in terms of wavefunctions. Microscopic physics provides the foundation for understanding atomic structure, chemical bonding, and fundamental interactions.

Macroscopic physics, in contrast, describes systems at the bulk scale, ranging from millimeters to thousands of kilometers and above. These systems are easily visible to the naked eye. In this regime, systems are typically modeled using deterministic continuum theories such as classical mechanics, thermodynamics, and fluid dynamics. Thermal and quantum fluctuations are averaged out, and physical quantities like pressure, temperature, and density are treated as smooth fields.

Mesoscopic physics bridges these two regimes. It focuses on systems whose characteristic sizes lie between the microscopic and macroscopic scales, typically ranging from 10^{-9} to 10^{-6} meters (nanometers to micrometers). Unlike macroscopic systems, where fluctuations average out, mesoscopic systems are strongly influenced

by thermal fluctuations and surface/interface interactions. These systems often display rich, complex phenomena that cannot be fully captured by classical continuum theories or purely microscopic descriptions.

At the mesoscopic scale, systems are small enough that *thermal fluctuations* play a significant role in their behavior. **Brownian Motion** is one such phenomenon where thermal fluctuations play a versatile role and dictate the physics.

1.1 Brownian Motion

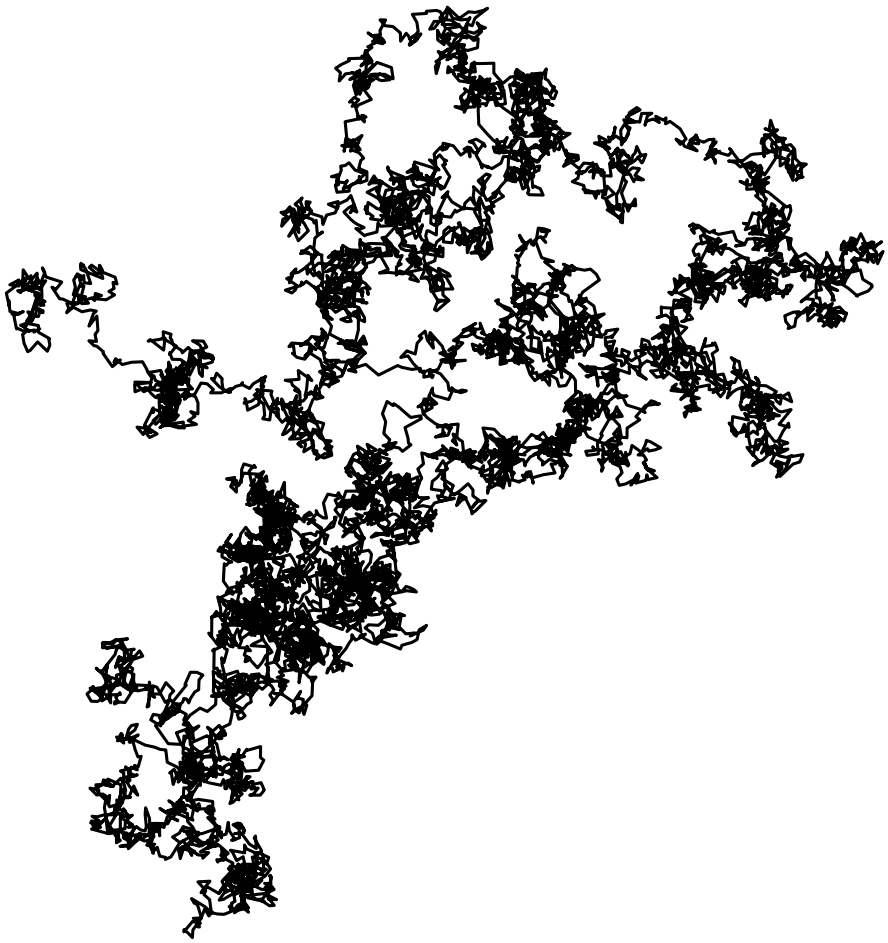

Figure 1.1: Motion of particle undergoing Brownian Motion

One of the earliest and most careful observations of the random motion of mesoscopic particles was made by Robert Brown in 1827 [1]. While examining pollen

grains of the plant *Clarckia pulchella* under a microscope, Brown noticed that tiny particles within the pollen grains exhibited a *continuous, erratic motion* when suspended in water. To determine whether this phenomenon was specific to living material, Brown extended his observations to a variety of inorganic substances, including powdered minerals, volcanic ash, and fragments of glass, all of which displayed similar random motion. This crucial step ruled out any biological origin (or vital force) and pointed toward a universal physical cause. Describing his observations, Brown wrote,

"While examining the form of these particles immersed in water, I observed many of them very evidently in motion; their motion consisting not only of a change of place in the fluid, manifested by alterations in their relative positions, but also not unfrequently of a change of form in the particle itself."

Further emphasizing the non-biological nature of this motion, he concluded, *"These motions were such as to satisfy me, after frequently repeated observation, that they arose neither from currents in the fluid, nor from its gradual evaporation, but belonged to the particle itself."*

Brown's insistence on the *spontaneous, non-biological motion* of these particles was radical at the time. He suggested that the motion was universal and not exclusive to living material, challenging the prevailing notions that associated internal motion solely with vitality. Although he could not determine the underlying mechanism, his meticulous observations laid the experimental foundation for future developments. This phenomenon, known today as Brownian motion, is named in his honor.

In 1905, Albert Einstein [2–4] proposed a theoretical explanation by showing that Brownian motion could be attributed to incessant collisions between suspended particles and the molecules of the surrounding fluid with the molecular kinetic theory as its basis. Einstein's theory connected the macroscopic long-time diffusion coefficient D with microscopic quantities such as temperature and particle size, providing one of the first quantitative proofs of the molecular nature of matter. In parallel, Marian Smoluchowski [5–8], in 1906, independently developed a complementary sta-

tistical approach, analyzing the random walk behavior of particles and emphasizing the probabilistic nature of their displacement over time. Further theoretical refinement came in 1908 when Paul Langevin [9–11] introduced a dynamic description of Brownian motion through what is now known as the Langevin equation. Langevin modeled the motion of a particle under the combined effects of systematic viscous drag and rapidly fluctuating random forces, successfully bridging Newtonian mechanics and stochastic behavior.

Jean Perrin's subsequent experiments in 1908–1909 [12–16], provided empirical confirmation of Einstein's theory, establishing Brownian motion as direct evidence for the molecular nature of matter. Jean Perrin was later awarded the Nobel Prize in physics in 1926 for this experimental study of colloids and the Brownian motion of particles suspended in liquids. Incidentally, Einstein was also awarded a Nobel Prize in 1921, not for his theoretical work on Brownian motion, but for the discovery of the law of the Photoelectric effect and services to theoretical physics.

Brownian Motion and Self-Diffusion

Brownian motion refers to the incessant, random movement of mesoscopic-sized particles suspended in a fluid, driven by collisions with the rapidly moving molecules of the medium. Brownian motion forms the physical basis of *self-diffusion*, the spontaneous spreading of particles within a medium due to their intrinsic thermal motion, even without any net concentration gradient or external force.

1.2 Langevin's Phenomenological Approach

In 1908, Paul Langevin [9–11, 17–19] proposed a classical phenomenological model for describing the Brownian motion of a mesoscopic particle, an approach he characterized as "infinitely more simple." For a single, structureless, free Brownian particle, in a stationary, homogeneous, isotropic, unbounded medium, in one dimension, he began with Newton's second law, assuming that the particle experiences two types of forces from the surrounding solvent molecules:

1. **Systematic viscous drag :** This force represents the mean effect of the solvent molecules on the particle. This viscous friction force acts in the direction opposite to the particle's motion, resisting its velocity. It arises due to the

Figure 1.2: Photograph of Paul Langevin (source: Linda Hall Library)

friction between the particle and the surrounding fluid molecules, which slows down the particle's movement over time. The drag force is often modeled by Stokes' law as $-\Gamma\vec{v}$, where Γ is the friction/damping coefficient and $\vec{v}$ is the particle's velocity. It corresponds to the systematic/deterministic component of the dynamics.

2. **Random rapidly fluctuating force (thermal noise) :** This force accounts for the fluctuating contribution due to particle-solvent interactions arising from random collisions of the particle with the solvent molecules. This fluctuating force accounts for the residual force exerted by the heat bath (solvent molecules) after subtracting the frictional (viscous) drag. This force is assumed to be independent of particle velocity and is also sometimes called the Langevin force or thermal noise.

Langevin further assumed that the macroscopic hydrodynamic damping formula $\Gamma = 6\pi\eta a$ holds for the Brownian particle (BP), where η is the dynamic (or absolute) viscosity of the fluid (heat-bath) and a is the radius of the particle, which he assumed spherical for simplicity. He also assumed that the fluctuating force should be equally likely to take both positive and negative values, meaning its mean is zero. This assumption reflects the idea that, on average, the random thermal impacts from the solvent molecules on the particle should not favor any particular direction, embodying the symmetric nature of the fluctuations. We discuss below Langevin's approach and elaborate on the details in our own words.

Consider a BP in one-dimensional space, where its mass and position are denoted by m and x, respectively. Langevin used X to denote the random, rapidly fluctuating force and called it the complementary force. Based on the above assumptions, he wrote the following equation of motion, ingeniously dividing the particle-bath interaction into deterministic and time-fluctuating (stochastic) parts:

$$m\dot{v} = \underbrace{-6\pi\eta a v}_{\text{systematic}} + \underbrace{X(t)}_{\text{stochastic}} \tag{1.2.1}$$

Multiplying both sides by x, yielding:

$$mx\dot{v} = -6\pi\eta a\, xv + X(t)\, x$$

Using $\frac{d}{dt}(xv) = v^2 + x\dot{v}$, we can rewrite the left-hand side as:

$$m\left[\frac{d}{dt}(xv) - v^2\right] = -6\pi\eta a\, xv + X(t)\, x$$

$$\frac{m}{2}\frac{d^2x^2(t)}{dt^2} - mv^2 = -3\pi\eta a\frac{dx^2(t)}{dt} + X(t)\, x(t), \quad \text{using} \quad \frac{1}{2}\frac{d}{dt}\left(x^2\right) = xv. \tag{1.2.2}$$

Because $X(t)$ is a random (stochastic) force representing thermal fluctuations, each realization of the Langevin equation produces a different trajectory $x(t)$. Therefore, rather than analyzing individual realizations, we focus on ensemble-averaged quantities, i.e., averages taken over many independent realizations of the stochastic

process at each instant in time (or equivalently, averages over a large number of independent, identical particles, each experiencing an independent instance of the stochastic force). We denote ensemble averages using angle brackets $\langle * \rangle$.

$$\left\langle \frac{m}{2} \frac{d^2 x^2(t)}{dt^2} \right\rangle - m \left\langle v^2(t) \right\rangle = -3\pi\eta a \left\langle \frac{d}{dt} x^2(t) \right\rangle + \langle X(t)\, x(t) \rangle \tag{1.2.3}$$

Ensemble Average and Time Derivative Commutation

Let us consider an ensemble of N independent systems (or realizations) evolving under the same stochastic dynamics. For each system $i = 1, 2, \ldots, N$.

The **ensemble average** of $\mathcal{Y}(t)$ is defined as:

$$\langle \mathcal{Y}(t) \rangle = \frac{1}{N} \sum_{i=1}^{N} \mathcal{Y}_i(t)$$

Here, N is the total number of systems in the ensemble. Each system follows its own trajectory due to stochasticity (e.g., noise, random initial conditions), and $\mathcal{Y}_i(t)$ captures the outcome of the i^{th} realization at time t.

Taking the time derivative of the ensemble average gives:

$$\frac{d}{dt} \langle \mathcal{Y}(t) \rangle = \frac{d}{dt} \left(\frac{1}{N} \sum_{i=1}^{N} \mathcal{Y}_i(t) \right) = \frac{1}{N} \sum_{i=1}^{N} \frac{d}{dt} \mathcal{Y}_i(t) = \left\langle \frac{d\mathcal{Y}(t)}{dt} \right\rangle$$

Thus,

$$\frac{d}{dt} \langle \mathcal{Y}(t) \rangle = \left\langle \frac{d\mathcal{Y}(t)}{dt} \right\rangle$$

One can interchange the order of differentiation and summation for a finite sum due to the linearity of both operations. Since an ensemble average corresponds to the limit of the sum as the number of realizations tends to infinity, this interchange is justified provided the ensemble sum converges uniformly.

$$\frac{m}{2}\frac{d^2\left\langle x^2(t)\right\rangle}{dt^2} - m\left\langle v^2(t)\right\rangle = -3\pi\eta a\frac{d\left\langle x^2(t)\right\rangle}{dt} + \left\langle X(t)\,x(t)\right\rangle \tag{1.2.4}$$

Langevin further made two more assumptions:

1. **Statistical independence assumption:** Langevin argued that, for a large number of identical particles, take the mean of the equations (1.2.2) written for each one of them, (which corresponds to an ensemble average). In his own words, "by the irregularity of the complementary force X, the average value of the term $\langle X(t)\,x(t)\rangle$ is evidently null." This means $\langle X(t)\,x(t)\rangle = 0$. This says that the particle's position $x(t)$ at time t is independent and hence uncorrelated with the random force acting on it at the same instant. Since the position at time $x(t)$ has resulted from stochastic forces existing in earlier intervals, this basically means that Langevin noise X is independent at different times. This tells us that the correlation time of noise is very small in comparison to *slow time scale* at which BP evolves.
   Thus, the equation becomes

$$\frac{m}{2}\frac{d^2\left\langle x^2(t)\right\rangle}{dt^2} - m\left\langle v^2(t)\right\rangle = -3\pi\eta a\frac{d\left\langle x^2(t)\right\rangle}{dt} \tag{1.2.5}$$

2. **Particle has equilibrated:** Since Langevin was interested in the long-time behavior of the system, he focused on time scales much larger than the characteristic velocity relaxation time. On such scales, the fast velocity degrees of freedom is assumed to have already equilibrated with the thermal bath. This assumption justifies him invoking the classical equipartition theorem, according to which the particle's kinetic energy reflects the bath temperature: $m\left\langle v^2(t)\right\rangle = k_BT$.

Thus,

$$\frac{m}{2}\frac{d^2}{dt^2}\left\langle x^2(t)\right\rangle + 3\pi\eta a\frac{d}{dt}\left\langle x^2(t)\right\rangle = k_BT, \tag{1.2.6}$$

This equation reduces to a first-order differential equation in $z(t) = \frac{d}{dt}\left\langle x^2(t)\right\rangle$.

$$\frac{m}{2}\frac{dz(t)}{dt} + 3\pi\eta a\,z(t) = k_BT \tag{1.2.7}$$

The solution to this equation is :

$$z(t) = \frac{2k_BT}{6\pi\eta a} + C\, e^{-\frac{6\pi\eta a}{m}t}, \tag{1.2.8}$$

where, $\zeta^{-1} = \frac{m}{6\pi\eta a}$ is the velocity relaxation time and C is an integration constant fixed by initial conditions. The exponential term decays rapidly over a timescale ζ^{-1}, which is approximately $10^{-8} - 10^{-6}$ seconds for BP depending on its size. After this short transient, $z(t)$ approaches a constant value, equal to the first term in the equation (1.2.8). Langevin then shows by integration of (1.2.8) for large times that:

$$\left\langle x^2(t)\right\rangle - \left\langle x(t_0)^2\right\rangle = \frac{2k_BT}{6\pi\eta a} \cdot (t - t_0)$$

Now, the displacement Δx is related to position as : $x(t) = x(t_0) + \Delta x$

$$\left\langle x^2(t)\right\rangle = \left\langle (x(t_0) + \Delta x)^2\right\rangle = \left\langle x^2(t_0)\right\rangle + 2\left\langle x(t_0)\Delta x\right\rangle + \left\langle \Delta x^2\right\rangle .$$

since the displacements Δx are random with equal probability of positive and negative values, the mean displacement is zero: $\langle \Delta x\rangle = 0$, and $\langle x(t_0)\Delta x\rangle = \langle x(t_0)\rangle \langle \Delta x\rangle = 0$, due to causality (or statistical independence).

Thus, the equation reduces to

$$\left\langle x^2(t)\right\rangle = \left\langle x^2(t_0)\right\rangle + \left\langle \Delta x^2\right\rangle ,$$

or equivalently,

$$\left\langle \Delta x^2\right\rangle = \left\langle x^2(t)\right\rangle - \left\langle x^2(t_0)\right\rangle .$$

The mean squared displacement takes the form,

$$\boxed{\left\langle \Delta x^2\right\rangle = \frac{2k_BT}{6\pi\eta a}(t - t_0).}$$

This shows that after a very short initial transient, the Brownian particle enters a diffusive regime where the mean squared displacement grows linearly in time,

consistent with the classical diffusion behavior, with diffusion coefficient D

$$D = \frac{k_B T}{6\pi\eta a}.$$

This relation is called the Stokes-Einstein relation, which relates the diffusivity of the particle to its damping and the temperature of the bath (equal to the temperature of a particle in equilibrium). Note that D here is a long-time global diffusion constant.

1.3 The Langevin Equation

The framework discussed in the previous section was Langevin's original phenomenological approach, introduced in 1908, to describe the dynamics of a BP. Although this approach was insightful and captured the essential physics, the random force remained heuristically defined, lacking a precise mathematical formulation. It was only much later, with the development of a formal mathematical treatment of stochastic processes, that Langevin's approach was formalized and the Langevin equation acquired its modern stochastic differential equation (SDE) form.

The Langevin equation [17, 18, 20, 21] in its modern form is an SDE that captures the dynamics of a BP by incorporating both dissipation and thermal fluctuations into a unified mesoscopic framework. Its genesis relies on the assumption that the mass (and size) of BP is substantially more than that of surrounding molecules, allowing for clear separation of the relaxation timescale for fluid and BP. This separation enables the formulation of a *fluctuation-dissipation relation* (FDR) [17, 18, 20, 22, 23] for BP, which establishes the damping (Γ) experienced by BP due to the surrounding fluid is intrinsically linked to the intensity of the bath induced stochastic forces ($F_{stoc}(t)$) acting on it, thereby ensuring that the particle equilibrates thermally with the fluid molecules.

$$\Gamma = \frac{1}{2k_B T}\int_{-\infty}^{\infty} ds\, \langle F_{stoc}(0) F_{stoc}(s)\rangle. \tag{1.3.1}$$

This equality is called the fluctuation-dissipation theorem of the second kind, which quantifies the intrinsic balance between energy loss due to damping and energy input from thermal fluctuations [17, 18, 20, 22, 23], where k_B is the Boltzmann constant. This relation ensures that the BP thermalizes locally with the heat bath

at time scales larger than $\zeta^{-1} = \frac{m}{\Gamma}$.

In its most simplistic form in one dimension, the Langevin equation for a free, structureless BP of mass m, instantaneous velocity v, constant damping Γ, in a quiescent, unbounded, homogeneous, isotropic fluid (heat-bath) at temperature T reads:

$$m\frac{dv}{dt} = -\Gamma v + F_{stoc}(t), \tag{1.3.2}$$

where $F_{stoc}(t)$ denotes a fluctuating stochastic force imparted by bath molecules to the particle. This stochastic force was represented by X in Langevin's phenomenological approach. This bath-induced stochastic force is modeled as Gaussian noise, representing the cumulative effect of a large number of rapid, random microscopic collisions with fluid molecules.

Since the fluctuating bath forces relax on a timescale of $\mathcal{O}(10^{-12})$ seconds, which is much shorter than BP's typical timescale of $\mathcal{O}(10^{-6} - 10^{-7})$ seconds (see Appendix A), the Gaussian noise becomes statistically uncorrelated at different time instants. This leads to a *Markovian* description of the dynamics, where the system (BP) has no memory of past fluctuations [17, 18]. In the *frequency domain*, this delta-correlated noise exhibits a *flat power spectral density*, meaning all frequencies contribute equally to the noise. Such a noise is termed as *white noise*.

Based on Eq. (1.3.1), the stochastic force is often expressed as $F_{\text{stoc}}(t) = \sqrt{2\Gamma k_B T}\,\eta(t)$, where the prefactor is the strength of fluctuation that ensures thermal equilibration at long times, as a consequence of FDR. The noise term $\eta(t)$ represents a continuous, Markovian, Gaussian white noise process with the statistical properties:

$$\langle \eta(t) \rangle = 0, \quad \langle \eta(t)\eta(t') \rangle = \delta(t - t').$$

Here, the noise $\eta(t)$ is a Gaussian white noise in the strong sense, i.e., a jointly Gaussian stochastic process with statistically independent noise values at different times. These conditions reflect isotropic, uncorrelated fluctuations with zero memory, capturing the rapid and random nature of microscopic collisions in the fluid.

Langevin Equation with Coordinate-Dependent Damping: In mesoscopic systems, spatial variations in damping naturally arise due to local heterogeneities [24, 25]. Under the assumption of local thermal equilibrium with the heat bath,

the position-dependent damping coefficient $\Gamma(x)$ can be related to the local temporal autocorrelation of the stochastic force via a more general form of the second fluctuation-dissipation relation [22, 23]:

$$\Gamma(x) = \frac{1}{2k_BT}\int_{-\infty}^{\infty} ds\, \langle F_{\text{stoc}}(x,0)F_{\text{stoc}}(x,s)\rangle. \tag{1.3.3}$$

This relation ensures that the Brownian particle remains in local thermal equilibrium with the fluid at temperature T, on timescales longer than the local velocity relaxation time $\zeta^{-1}(x) = \frac{m}{\Gamma(x)}$ [23]. This form of FDR ensures that **no additional drift term needs to be added to ensure local equilibrium of BP with the heat bath.** When the damping for such a system depends on position, the Langevin equation generalizes to:

$$\boxed{m\frac{dv(t)}{dt} = -\Gamma(x)v(t) + \sqrt{2\Gamma(x)k_BT}\,\eta(t),} \tag{1.3.4}$$

where $F_{\text{stoc}}(x,t) = \sqrt{2\Gamma(x)k_BT}\,\eta(t)$, and $\eta(t)$ is a Gaussian white noise with same properties as for constant damping case.

When an external force F_{ext} acts on the Brownian particle and varies slowly enough so as not to disrupt the underlying fluctuation–dissipation balance, the Langevin equation generalizes to

$$m\frac{dv}{dt} = -\Gamma(x)v(t) + F_{\text{ext}} + \sqrt{2\Gamma(x)k_BT}\,\eta(t). \tag{1.3.5}$$

Neglecting Inertia: Overdamped approximation

In mesoscopic systems, such as biological entities ranging from nanometers to micrometers in size, the interplay between forces is fundamentally different from that at macroscopic scales. The characteristic energy scale for such systems is of the order k_BT, where thermal fluctuations are significant [26, 27]. Here, viscous forces dominate the motion due to the highly resistive fluid environment, while inertial effects become negligible. At these scales, the Reynolds number, a dimensionless quantity expressing the ratio of inertial to viscous forces, is extremely small ($\text{Re} \ll 1$). As a consequence, any acceleration of a particle is rapidly damped by viscous forces, caus-

ing its velocity to relax almost instantaneously compared to the slowest timescale of position degree of freedom. It is thus physically justified and mathematically convenient to approximate the dynamics by neglecting inertia entirely, which is called the overdamped approximation for such systems.

An overdamped or viscous limit of the Langevin dynamics corresponds to the regime of slowest temporal evolution. In this limit, the BP is always in local equilibrium with the heat bath because the dynamics evolves slower than its own momentum relaxation time $\zeta(x)^{-1}$. The contribution from the inertial term in the Langevin equation becomes negligible compared to the other terms. Formally, this overdamped limit is taken by letting $m \to 0$ and $\zeta(x) \to \infty$, while keeping the product $\Gamma(x) = m\zeta(x)$ finite. Taking this limit in Eq. (1.3.4), the following overdamped-Langevin equation (also called as Brownian equation) emerges:

$$\boxed{\frac{dx}{dt} = \sqrt{2D(x)}\eta(t),} \tag{1.3.6}$$

where the local diffusivity $D(x)$ is related to the local damping coefficient $\Gamma(x)$ as $D(x) = k_B T/\Gamma(x)$ by the local Stokes-Einstein relation.

In the presence of $F_{ext}(x)$ (which is weak enough not to disrupt the local fluctuation-dissipation balance), the overdamped Langevin equation becomes:

$$\frac{dx}{dt} = \frac{F_{\text{ext}}(x)}{\Gamma(x)} + \sqrt{2D(x)}\,\eta(t). \tag{1.3.7}$$

Accordingly, in the chapters that follow, we will focus exclusively on the overdamped regime, which accurately captures the behavior of mesoscopic particles under thermal fluctuations in low Reynolds number environments.

The Shift from Homogeneous to Inhomogeneous Damping in Brownian Motion

For much of the 20th century, Einstein, Smoluchowski, and Langevin's description of Brownian motion, featuring a constant damping coefficient, proved remarkably successful in describing particle dynamics in homogeneous fluids. In such systems, far from boundaries or interfaces, the viscous drag experienced by a particle is well-approximated by Stokes' law with constant damping, leading to a constant

diffusivity and a linear time dependence of the mean-squared displacement (MSD). This prediction was not only confirmed in countless experiments but also played a pivotal role in validating the atomic hypothesis, by linking mesoscopic thermal fluctuations to macroscopic observables [3, 13].

However, by the late 1980's, it had become increasingly evident that this assumption of uniform damping breaks down in spatially inhomogeneous environments. Experiments and theoretical studies showed that proximity to boundaries or other Brownian particles could induce spatial variations in hydrodynamic drag, leading to coordinate-dependent diffusivity [25, 28, 29]. A notable demonstration came from Faucheux and Libchaber in 1994 [24], who studied the Brownian motion of microspheres (1–3 μm diameter) suspended in ultrapure water between two horizontal glass plates. They measured the decrease in particle's diffusivity as it approached the walls, showing clear evidence of position-dependent damping. These observations highlighted that damping can become position-dependent, even in equilibrium systems, motivating plenty of experiments in this direction [30–32].

In the following section, we delve into the case of state-dependent diffusion, where the system (in the overdamped regime) is in local thermal equilibrium with the bath and the diffusivity depends explicitly on the particle's position. This phenomenon is also referred to in the literature as heterogeneous diffusion or diffusion in inhomogeneous media.

1.4 Noise-Induced Drift in State-Dependent Diffusion

Consider the overdamped equation of motion of a BP in one-dimensional space with position coordinate x, in the presence of a potential $U(x)$ due to a conservative force, local diffusivity $D(x)$, and local damping $\Gamma(x)$, in contact with a heat bath in equilibrium at temperature T. The local Stokes–Einstein relation holds $D(x) = \frac{k_B T}{\Gamma(x)}$.

The stochastic dynamics is governed by the overdamped Langevin equation:

$$\frac{dx}{dt} = -\frac{1}{\Gamma(x)}\frac{\partial U(x)}{\partial x} + \sqrt{2D(x)}\,\eta(t), \tag{1.4.1}$$

where $\eta(t)$ is a Gaussian white noise with

$$\langle \eta(t) \rangle = 0, \quad \langle \eta(t)\eta(t') \rangle = \delta(t - t').$$

In the absence of potential, Eq. (1.4.1) reduces to

$$\frac{dx}{dt} = \sqrt{2D(x)}\,\eta(t). \tag{1.4.2}$$

Integrating over a time interval Δt, the increment in position is

$$\Delta x = \int_{t_0}^{t_0+\Delta t} \sqrt{2D(x(t'))}\,\eta(t')\,dt', \tag{1.4.3}$$

where $\Delta x = x(t_0 + \Delta t) - x(t_0)$.

Here, the noise term $\sqrt{2D(x)}\,\eta(t)$ is *multiplicative noise* since its amplitude depends explicitly on the state x, also called state-dependent noise. However, $\eta(t)$ is not a regular function but a generalized function (distribution), characterized by infinite variance and undefined pointwise values. As a result, the standard rules of calculus, such as those governing Riemann or Lebesgue integration do not apply in this context. For ordinary (smooth) functions, the precise point at which the integrand is evaluated within an interval $[t_0, t_0 + \Delta t]$ does not affect the value of the integral in the limit $\Delta t \to 0$. However, in stochastic integrals involving multiplicative noise, the choice of evaluation point becomes crucial. It matters at what point in the time interval $[t_0, t_0 + \Delta t]$ should the integrand $\sqrt{2D(x)}$ be evaluated.

Thus, the stochastic integral in Eq. (1.4.3) remains mathematically ill-defined unless one specifies the precise interpretation of the integral, that is, the rule governing how the state-dependent noise coefficient $\sqrt{2D(x)}$ is evaluated relative to the stochastic increments of $\eta(t)$. The question then becomes: at what point in the time interval $[t_0, t_0 + \Delta t]$ should the function $D(x)$ be evaluated? The answer depends on the choice one chooses. That is, the stochastic integral can have different values depending on the *interpretation of the integral* i.e., the rule used to evaluate the integrand within each infinitesimal time interval. This leads to the need for a *stochastic calculus convention*, also referred to as the *sense* of the stochastic

differential equation. To parameterize this choice, we define

$$t' = t_0 + \lambda \Delta t,$$

and evaluate the diffusion coefficient as

$$D(x(t_0 + \lambda \Delta t)) \equiv D\big(x(t_0) + \lambda \Delta x\big),$$

where $\lambda \in [0, 1]$ is the interpolation parameter. Following three common conventions are prevalent in Physics literature:

- **Itô interpretation** ($\lambda = 0$), where the noise coefficient is evaluated at the beginning of each time step, i.e., at $t = t_0$; equivalently, the diffusion coefficient is taken as $D(x(t_0))$.

- **Stratonovich interpretation** ($\lambda = 1/2$), where the noise coefficient is evaluated at the midpoint [1] , i.e., at $t = \frac{t_0 + \Delta t}{2}$; equivalently, the diffusion coefficient is taken as $D\big(x(t_0) + \frac{1}{2}\,\Delta x\big) = D\Big(\frac{x(t_0) + x(t_0 + \Delta t)}{2}\Big)$.

- **Anti-Itô interpretation** ($\lambda = 1$), where the coefficient is evaluated at the end of the time step, i.e., at $t = t_0 + \Delta t$; equivalently, the diffusion coefficient is taken as $D(x(t_0 + \Delta t))$. Note that it is also called in literature as Hänggi–Klimontovich, Isothermal and the kinetic interpretation [35].

Thus, Eq. (1.4.3) can be written as

$$\Delta x = \int_{t_0}^{t_0 + \Delta t} \sqrt{2D\big(x(t_0 + \lambda \Delta t)\big)}\, \eta(t')\, dt'. \tag{1.4.4}$$

Discretizing for small Δt (see Appendix C), we have

$$\Delta x = \sqrt{2D(x + \lambda \Delta x)\Delta t}\, \xi_R, \tag{1.4.5}$$

[1] In standard textbooks [11], the Stratonovich choice is described as evaluating the diffusion coefficient at the midpoint in position, $D\big(x(t_0) + \frac{1}{2}\Delta x\big)$. For Brownian motion, this is equivalent to evaluating diffusivity at the time midpoint. See Theorem V-5.30 in Protter [33] and also Øksendal [34].

where $\xi_R \sim \mathcal{N}(0,1)$ is a standard Gaussian random variable, and for brevity we write $x \equiv x(t_0)$.

Expanding $D(x + \lambda\Delta x)$ to linear order:

$$D(x + \lambda\Delta x) \approx D(x) + \lambda \frac{dD}{dx}\Delta x + \mathcal{O}(\Delta x^2).$$

Substituting into eq. (1.4.5):

$$\begin{aligned}
\Delta x &\approx \xi_R \sqrt{2\left(D(x) + \lambda\frac{dD}{dx}\Delta x\right)\Delta t} \\
&= \xi_R\sqrt{2D(x)\Delta t}\left(1 + \lambda\frac{dD}{dx}\frac{\Delta x}{D(x)}\right)^{1/2} \\
&\approx \xi_R\sqrt{2D(x)\Delta t}\left(1 + \frac{\lambda}{2}\frac{\Delta x}{D(x)}\frac{dD}{dx}\right) \\
&= \xi_R\sqrt{2D(x)\Delta t} + \underbrace{\frac{\lambda}{2}\frac{dD}{dx}\frac{\Delta x}{D(x)}\xi_R\sqrt{2D(x)\Delta t}}.
\end{aligned}$$

Rearranging to isolate Δx:

$$\begin{aligned}
\Delta x &= \xi_R\sqrt{2D(x)\Delta t}\left(1 - \frac{\lambda}{2}\frac{dD}{dx}\frac{\xi_R\sqrt{2D(x)\Delta t}}{D(x)}\right)^{-1} \\
&\approx \xi_R\sqrt{2D(x)\Delta t}\left(1 + \frac{\lambda}{2}\frac{dD}{dx}\frac{\xi_R\sqrt{2D(x)\Delta t}}{D(x)}\right) \\
&= \xi_R\sqrt{2D(x)\Delta t} + \lambda\frac{dD}{dx}\xi_R^2\Delta t.
\end{aligned}$$

Using $\langle\xi_R\rangle = 0, \langle\xi_R^2\rangle = 1$, the average displacement for small Δt becomes

$$\langle\Delta x\rangle = \lambda\frac{dD}{dx}\Delta t + \mathcal{O}(\Delta t^{3/2}). \tag{1.4.6}$$

This corresponds to an effective *noise-induced drift velocity* [36]

$$v^{\lambda}_{\text{drift}} = \lambda\frac{dD}{dx}, \tag{1.4.7}$$

also known as *spurious flow*, *spurious drift* or *noise-induced drift*. Note that even without external forces, the spatial variation of diffusivity generates a deterministic drift whose direction is in that of the diffusivity gradient and magnitude depends on the stochastic interpretation parameter λ.

Noise-induced drift is the measure of correlation introduced in the noise. For any $\lambda \neq 0$, one is explicitly introducing correlation because the noise is being calculated at a future times. *Only under the Itô prescription, the noise remains correlation-free.* The noise term in Itô prescription is evaluated using the state at the beginning of the time interval, ensuring that it is uncorrelated with the future evolution of the system. Therefore, Itô prescription is also called *non-anticipating*. All other prescriptions, be it Stratonovich ($\lambda = \frac{1}{2}$), Anti-Itô ($\lambda = 1$) or any other, are anticipatory in nature.

Note that from Eq. (1.4.6), it is clear that even under the generalised λ (also called as generalized Stratonovich) architecture, the local average of the diffusion term vanishes $\left(\langle \xi_R \sqrt{2D(x(t_0))\Delta t} \rangle = 0\right)$ as *diffusion (normal) is locally isotropic*. Thus, the total stochastic displacement Δx over small time Δt becomes,

$$\Delta x = \lambda \frac{dD}{dx}\Delta t + \xi_R \sqrt{2D(x)\Delta t} + \mathcal{O}(\Delta t^{3/2}), \quad x \equiv x(t_0).$$

In the presence of a conservative force derived from a potential $U(x)$, the displacement update rule over a small time interval Δt becomes:

$$\Delta x = -\frac{\Delta t}{\Gamma(x)}\frac{\partial U}{\partial x} + \lambda \frac{dD}{dx}\Delta t + \sqrt{2D(x)\Delta t}\,\xi_R + \mathcal{O}(\Delta t^{3/2}), \quad x \equiv x(t_0). \tag{1.4.8}$$

Thus, the total drift velocity in λ architecture is:

$$v_d(x) = \lambda \frac{dD}{dx} - \frac{1}{\Gamma(x)}\frac{\partial U}{\partial x}.$$

Note that the diffusion term remains unchanged in any architecture.

1.5 Fokker Planck for Generalized Stratonovich Process

Now, one can immediately write a corresponding Fokker–Planck equation for the probability density $P(x,t)$ for the generalized Stratonovich process.

$$\begin{aligned}\frac{\partial P(x,t)}{\partial t} &= -\frac{\partial}{\partial x}\left[v_d(x)P(x,t) - \frac{\partial}{\partial x}\big(D(x)P(x,t)\big)\right] \\ &= -\frac{\partial J(x,t)}{\partial x},\end{aligned} \tag{1.5.1}$$

where $J(x,t)$ is the total probability current density with, $J(x,t) = v_d(x)P(x,t) - \frac{\partial}{\partial x}(D(x)P(x,t))$.

Equilibrium steady state solution corresponds to $\frac{\partial P(x,t)}{\partial t} = 0$, that is probability distribution becomes time independent. Along with that, the condition of local detailed balance also has to be satisfied, i.e., setting of the probability current to zero, $J(x) = 0$, yielding the equilibrium distribution $P(x)$ corresponding to generalized Stratonovich as:

$$P(x) = \frac{C}{D(x)^{1-\lambda}} \exp\left(-\frac{U(x)}{k_B T}\right), \tag{1.5.2}$$

where, diffusivity and damping obey local Stokes-Einstein relation, $D(x) = k_B T/\Gamma(x)$ and C is the normalization constant.

We list the corresponding equilibrium distributions for different choices of λ:

- **Itô interpretation** ($\lambda = 0$):

$$P(x) = \frac{C}{D(x)} \exp\left(-\frac{U(x)}{k_B T}\right)$$

- **Stratonovich interpretation** ($\lambda = \frac{1}{2}$):

$$P(x) = \frac{C}{\sqrt{D(x)}} \exp\left(-\frac{U(x)}{k_B T}\right)$$

- **Anti-Itô interpretation** ($\lambda = 1$):

$$P(x) = C \exp\left(-\frac{U(x)}{k_B T}\right)$$

These expressions clearly demonstrate that the steady-state distribution is sensitive to the choice of stochastic interpretation when the diffusivity $D(x)$ is position-dependent. Note that under the Itô interpretation ($\lambda = 0$), the equilibrium distribution includes an inverse dependence on the diffusivity, leading to an effective accumulation of probability in low-diffusivity regions. The Stratonovich case ($\lambda = \frac{1}{2}$) yields a milder dependence, involving a square root of $D(x)$. The Anti-Itô interpretation ($\lambda = 1$) gives the distribution dependent only on the potential $U(x)$, independent of the diffusivity profile.

It is worth noting that different scientific communities often favor different stochastic interpretations based on their respective priorities. **Mathematicians** tend to prefer the *Itô interpretation* due to its rigorous mathematical framework, particularly the martingale property and the non-anticipative nature of Itô integrals, which are foundational in stochastic analysis and financial mathematics. In contrast, most **physicists** often favor the *Anti-Itô* interpretation because it naturally yields the most familiar form of canonical Boltzmann distribution [37].

Imposing Boltzmann Distribution by Hand

To reconcile deviations from the canonical Boltzmann distribution in interpretations other than Anti-Itô, it has sometimes become practice in the statistical physics community to introduce an additional *ad-hoc drift term by hand* to the right-hand side of the Langevin equation. This term is not derived from microscopic dynamics but is inserted *a posteriori* to ensure Anti-Itô distribution.

Under the generalized stochastic interpretation parameterized by λ, the probability current density reads:

$$J(x,t) = -\frac{1}{\Gamma(x)}\frac{\partial U(x)}{\partial x} P(x,t) - \frac{\partial}{\partial x}\left(D(x)\, P(x,t)\right) + \lambda \frac{\partial D(x)}{\partial x} P(x,t).$$

This expression can be rewritten as:

$$J(x,t) = -\frac{1}{\Gamma(x)}\frac{\partial U(x)}{\partial x}\,P(x,t) - D(x)\frac{\partial P(x,t)}{\partial x} - (1-\lambda)\frac{\partial D(x)}{\partial x}\,P(x,t)$$

An *ad-hoc term* $+(1-\lambda)\frac{\partial D(x)}{\partial x}$is added by hand to the Langevin equation [37] to cancel the term $-(1-\lambda)\frac{\partial D(x)}{\partial x}$. This adjustment alters the stochastic dynamics so that the corresponding Fokker–Planck equation yields the Anti-Itô distribution, regardless of the chosen λ.

This practice, while common, reveals a deeper issue: the equilibrium distribution is not uniquely determined by the physical ingredients $U(x)$ and $D(x)$, but also by the interpretive framework. The widespread imposition of the familiar Boltzmann form, even when it does not arise naturally from the dynamics, reflects a bias toward the canonical distribution's appearance. In this sense, the Anti-Itô distribution is often *imposed adhoc*, raising conceptual concerns about the physical legitimacy of such procedures in spatially inhomogeneous systems.

Discussion on Boltzmann Distribution

The Boltzmann distribution characterizes the equilibrium of a system in the thermodynamic limit, where inhomogeneity in the bulk is due to some conservative force. This conservative force breaks the homogeneity of the space, biasing the distribution and is hence reflected in the distribution from a uniform one to $P(x) = C\exp\left(-\frac{U(x)}{k_BT}\right)$.

Mesoscopic systems operate away from the thermodynamic limit. In such systems, boundary-induced inhomogeneities are often present, which a conservative force cannot capture. In the context of Brownian particles, in a confinement or in the vicinity of each other, the net effect is that the damping/diffusivity becomes coordinate-dependent, bringing itself as an additional agent which breaks the homogeneity of space. It is thus plausible to expect this source of inhomogeneity to be captured by the equilibrium probability distribution.

In the following sections, we make a case for why the Itô distribution is a legitimate candidate to describe the equilibrium of BP in the presence of coordinate-dependent damping.

1.6 Discussion on Itô Equilibrium Distribution

We first discuss the physical basis of probability currents following the discussion by Bhattacharyay in [23, 38]. For a stationary equilibrium solution of a generalized Stratonovich process, detailed balance demands that the probability current must vanish:

$$\underbrace{-\frac{1}{\Gamma(x)}\frac{\partial U(x)}{\partial x}P(x)}_{\text{drift due to potential}}+\underbrace{\lambda\frac{\partial D(x)}{\partial x}P(x)}_{\text{noise induced drift/ spurious drift}}-\left(\underbrace{D(x)\frac{\partial P(x)}{\partial x}}_{\text{fickian term}}+\underbrace{P(x)\frac{\partial D(x)}{\partial x}}_{\text{additional term}}\right)=0. \tag{1.6.1}$$

As shown in previous sections, $\lambda = 0$ corresponds to an Itô process, which is correlation-free or non-anticipitating, and the equilibrium distribution for an Itô process is:

$$P(x) \propto \frac{1}{D(x)} e^{-U(x)/k_B T},$$

owing to the presence of the additional diffusion current term $-P(x)\,\frac{\partial D(x)}{\partial x}$ that arises from the coordinate dependence of the diffusivity. This is also referred to as diffusion gradient-induced current density. This term is *convention-independent* and *persists regardless of the stochastic calculus convention used [23, 39].*

For $\lambda = 1$, corresponding to the Anti-Itô convention, the equilibrium distribution becomes:

$$P(x) \propto e^{-U(x)/k_B T},$$

because the *spurious drift density term* $P(x)\,\frac{\partial D(x)}{\partial x}$ exactly cancels the additional diffusion current, restoring the distribution to a familiar-looking form of the canonical distribution (Anti-Itô). For intermediate α, the steady-state equilibrium distribution lies between the Itô and Anti-Itô forms.

Now, to understand how and why current density (probability flow) emerges in such systems, it would be helpful to look at a discrete version of diffusion, which is a jump process. This is exactly the path employed in [23, 38] to understand the meaning associated with each term.

We consider a linearly increasing diffusivity profile $D(x)$ as in Fig. 1.3 for simplicity. We have already established in the previous sections that diffusion (normal)

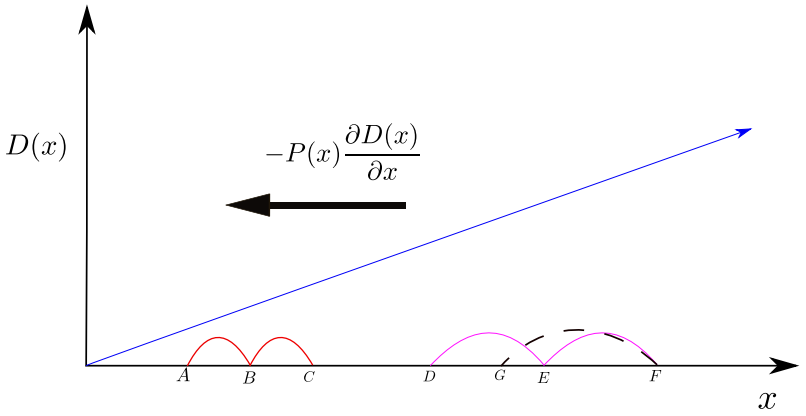

Figure 1.3: Schematic to understand the origin of additional current arising from global broken symmetry in the presence of a diffusivity gradient for Itô prescription. Adapted from [23, 38].

is locally isotropic. Because of this local isotropy in diffusion, a particle at position B makes symmetric jumps to positions A and C. At another point E with higher diffusivity, the particle jumps to D, and F are larger in size but still symmetric. Although each individual jump is locally isotropic (unbiased), the global gradient in diffusivity implies that over an ensemble, asymmetric effective currents arise. For instance, a forward jump from E to F followed by a backward jump to G results in a net backward displacement, giving rise to a current in the direction opposite to the gradient. Such processes accumulate to generate the additional diffusion current $-P(x)\frac{\partial}{\partial x}D(x)$. It is very important to note that this current is *not a drift current* since it does not stem from local breaking of isotropy due to a force. Rather, it arises from the spatial variation of diffusivity and is present in all interpretations, be it Itô, Stratonovich, or Anti-Itô.

We compare this with Anti-Itô convention with $\lambda = 1$, illustrated in Fig. 1.4. Note that, noise is *anticipating*. This means that particles preferentially make longer jumps toward regions of higher diffusivity. This local asymmetry in jump size mimics the effect of a force and induces a *spurious drift current* in the direction of the diffusivity gradient $J_{\text{spurious drift}} = P(x)\,\frac{\partial D(x)}{\partial x}$. This spurious drift current exactly cancels the legitimate "additional" diffusion current $-P(x)\,\frac{\partial D(x)}{\partial x}$ when $\lambda = 1$, resulting in the canonical equilibrium distribution. However, this cancellation is purely mathematical and does not correspond to any underlying physical mechanism or

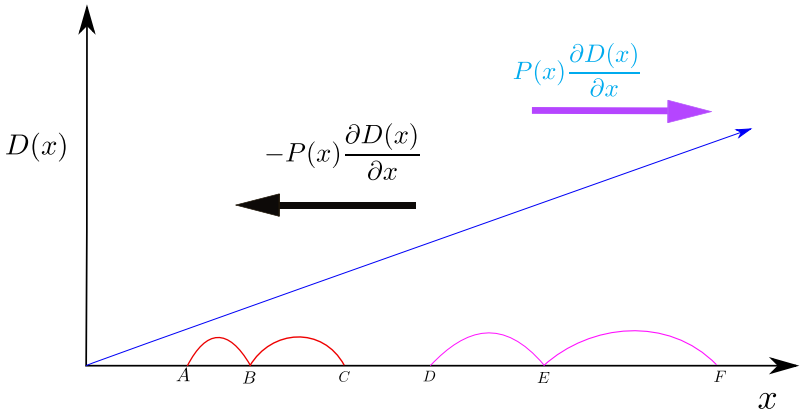

Figure 1.4: Schematic to understand the origin of spurious current along with additional currents in the presence of a diffusivity gradient due to anticipating noise for Itô prescription. Adapted from [23, 38].

conservative force.

Related works

The work by Escudero and Rojas [35] investigates how different interpretations of stochastic calculus impact the kinetic energy dynamics of a Brownian particle with constant damping (and diffusivity) in Langevin dynamics. They demonstrate that only the Itô interpretation consistently captures the physical behavior expected in thermal environments, such as kinetic energy growth from rest due to thermal fluctuations. In contrast, Stratonovich and Anti-Itô interpretations can lead to unphysical outcomes, like absorbing states at zero energy or non-real (complex) fluctuations/ negative kinetic energy. They extend their finding to relativistic systems and highlight the Itô convention as the physically robust choice for modeling energy evolution in stochastic processes since it possesses a unique global, physical solution as a consequence of the Watanabe-Yamada theorem [40].

There have also been other approaches that support the Itô framework as physically meaningful. In particular, Bhattacharyay [23] demonstrates that multiplicative noise in systems with coordinate-dependent damping can be transformed into an effective additive noise form through local rescaling of space and time, performed in a way that preserves the particle's velocity and, consequently, the temperature of the bath. This analysis reveals that the Itô steady-state distribution emerges natu-

rally as the equilibrium distribution in such systems. Furthermore, the same work interprets the $\frac{1}{D(x)}$ factor in the Itô distribution as the local density of states, which reduces to the standard Boltzmann distribution when the diffusivity $D(x)$ is spatially uniform. This will also be discussed in chapter 5. Escudero [41] has explored the problem in a different way, where he uses the theory of backward stochastic differential equations and shows that some solutions originating from the Stratonovich interpretation are unphysical in nature; however, such a problem does not arise in Itô. In the lattice model by Maniar and Bhattacharyay [42], the authors compare the Itô process with Anti-Itô for a weakly non-equilibrium process and their findings reveal that Itô process gives more physically meaningful results than Anti-Itô. There has been similar line of work which can be found in ref [23, 43–45]. The author and coworkers have demonstrated in ref.[46] that non-Fickian transport currents, emerging naturally within the Itô framework of stochastic dynamics, successfully explain the experimentally observed trends in the thermophoresis of colloidal proteins like Lysozyme, BLGA, and Poly-l-lysine in aqueous solution. In a different context, the superiority of Itô has been argued over Stratonovich even for a stochastic cosmological model [47].

1.7 Main Research Questions Addressed

The central aim of this thesis is to understand the transport of mesoscopic objects in the presence of coordinate-dependent damping. We explore the consequences of modeling the coordinate-dependent damping as an Itô process.

1.7.1 Outline

This thesis is organized as follows.

Chapter 2 We begin by introducing a damping symmetry-broken structured mesoscopic object placed in a heat bath in one-dimensional space in the absence of any external force, where interactions in the system depend only on relative separation. We derive an equilibrium distribution in position space under the Itô setting. Our analysis demonstrates that the symmetry-broken dimer can spontaneously filter isotropic, homogeneous bath fluctuations in equilibrium. As a consequence, the object moves with a non-zero constant velocity in a

force-free situation, signifying that steady-state mechanical equilibrium with directed motion is possible for a symmetry-broken object in thermal atmosphere. We further discuss how the system is in accordance with principles like energy conservation, the second law of thermodynamics, and detailed balance. Publication related to this project– (i).

Chapter 3 We extend our study to now account for an external force against which the dimer could move and store energy. We analyze how the equilibrium position distribution of the dimer system changes due to the presence of a force. We also display how various system parameters contribute to the efficiency of ratcheting, converting heat to work. Publication related to this project– (i).

Chapter 4 We broaden our purely equilibrium single symmetry-broken dimer framework to a many-body system consisting of multiple symmetry-broken dimers interacting in two-dimensional space. Here, the collective behavior emerges from the interplay of coordinate-dependent damping and thermal fluctuations. We explore how these many-body interactions lead to spontaneous collective transport phenomena such as swarming, flocking, and coherent rotation, all occurring in thermal equilibrium without external driving. The study provides new insights into how broken damping symmetry can give rise to rich emergent dynamics in higher dimensions. Publication related to this project—(ii).

Chapter 5 We study the transient dynamics of mesoscopic objects within the Itô framework. This chapter focuses on the evolution towards Itô equilibrium steady states, analyzing transient processes under the influence of coordinate-dependent damping. We highlight how inhomogeneity in diffusivity within the Itô framework leads to the emergence of a new source of entropy, which generates a diffusivity-dependent entropy gradient that influences the transport. We talk about novel effects of entropic pulling and diffusion diode, which emerge as a consequence of it. Publication related to this project—(iii).

Chapter 6 Finally, we conclude this thesis with closing remarks and future prospects.

2

Symmetry-Broken Dimer Model

Biological systems are inherently structured and asymmetric. Inside living cells, motor proteins like kinesin and myosin (consisting of two heads) walk along molecular tracks, playing a vital role in transport and other biomechanical processes. To understand their motion, various ratcheting models have been proposed [48, 49]. However, these simple models often predict much lower efficiencies than those observed in real motor proteins [50].

Real biological systems are far more complex than any simplified model. But when the efficiency gap is significant, it suggests that something fundamental might be missing. One common assumption in many ratcheting models is that motor proteins are structureless particles, overlooking their internal mechanics and asymmetries. Yet, biological transport mechanisms rely on intricate structural features that significantly impact efficiency.

To explore the role of structure in transport, we consider a simple structured system, a dimer. We consider this because it is one of the most basic ways to introduce internal structure while keeping the problem manageable. To model asymmetry, we consider a dimer with broken damping symmetry. Such a model based on coordinate-dependent diffusion was first proposed by Bhattacharyay in 2012 [51]. In this chapter, we study how this system, constrained in one-dimensional space, behaves in an equilibrium bath, examining how its internal properties influence its motion. This chapter is adapted from Ref. [52].

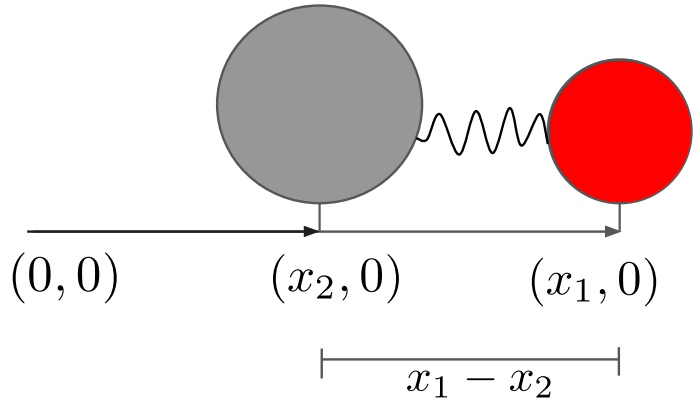

Figure 2.1: Schematic of a dimer in one dimension.

2.1 Dimer model with Broken damping symmetry under Itô formulation

Consider two Brownian particles constrained in one-dimensional space with coordinates x_1 and x_2 ($x_1 > x_2$), in contact with an isotropic, homogeneous heat bath in thermal equilibrium at a temperature T. These two Brownian particles constitute a dimer, interacting via an attractive potential that ensures cohesion, except at very short distances, where repulsion accounts for excluded volume effects.

It is common knowledge that biological systems at submicrometer scales operate in a regime dominated by high friction, making inertia's contribution negligible. Thus, we describe the system in the over-damped limit(inertia-less limit), where the dynamics of the particles is governed primarily by dissipative forces and thermal fluctuations. The over-damped equations of motion for the two particles are:

$$\begin{aligned} \frac{dx_1}{dt} &= -\frac{1}{\Gamma_1(z)}\frac{\partial V(z)}{\partial x_1} + \sqrt{\frac{2k_BT}{\Gamma_1(z)}}\,\eta_1(t), \\ \frac{dx_2}{dt} &= -\frac{1}{\Gamma_2(z)}\frac{\partial V(z)}{\partial x_2} + \sqrt{\frac{2k_BT}{\Gamma_2(z)}}\,\eta_2(t). \end{aligned} \tag{2.1.1}$$

where $z = x_1 - x_2$ is configuration/internal coordinate, $\eta_i(t)$ is Gaussian white noise of unit strength with zero mean $\langle \eta_i(t) \rangle = 0$ and no temporal and inter-particle correlation i.e. $\langle \eta_i(t_1)\eta_j(t_2) \rangle = \delta_{ij}\delta(t_1 - t_2)$ and k_B is the Boltzmann constant. Particles

are characterized by different damping coefficients $\Gamma_i(z)$ $(i = 1, 2)$ which depend on the configuration coordinate z of the system, and therefore can differ between the particles. For instance, a particle close to a wall experiences altered hydrodynamic drag, causing its damping to vary with the distance from the boundary [24, 53]. Similarly, nearby particles can influence damping, making it a spatially dependent property. $V(z)$ is the interaction potential between these particles. Considering the centre of mass (CM) of the dimer to be $x = \frac{x_1+x_2}{2}$. Although this is technically the center of the system rather than a true center of mass, we refer to it as CM throughout the thesis. One performs a coordinate transformation and rewrites the dynamics as:

$$\begin{aligned} \frac{dz}{dt} &= -\left[\frac{1}{\Gamma_1(z)} + \frac{1}{\Gamma_2(z)}\right]\frac{dV(z)}{dz} + \xi_z(z,t), \\ \frac{dx}{dt} &= -\frac{1}{2}\left[\frac{1}{\Gamma_1(z)} - \frac{1}{\Gamma_2(z)}\right]\frac{dV(z)}{dz} + \xi_x(z,t). \end{aligned} \tag{2.1.2}$$

where, $\xi_z(z,t) = \sqrt{2k_BT}\left[\frac{\eta_1(t)}{\sqrt{\Gamma_1(z)}} - \frac{\eta_2(t)}{\sqrt{\Gamma_2(z)}}\right]$ and $\xi_x(z,t) = \sqrt{k_BT}\left[\frac{\eta_1(t)}{\sqrt{2\Gamma_1(z)}} + \frac{\eta_2(t)}{\sqrt{2\Gamma_2(z)}}\right]$ are linear combination of white noise, such that the auto correlation of noise at various times is $\langle \xi_z(z,t_1)\xi_z(z,t_2)\rangle = 2k_BT\left(\frac{1}{\Gamma_1(z)} + \frac{1}{\Gamma_2(z)}\right)\delta(t_1-t_2)$ and $\langle \xi_x(z,t_1)\xi_x(z,t_2)\rangle = \frac{k_BT}{2}\left(\frac{1}{\Gamma_1(z)} + \frac{1}{\Gamma_2(z)}\right)\delta(t_1-t_2)$. Note that $\langle \xi_z(z,t)\rangle = 0$ and $\langle \xi_x(z,t)\rangle = 0$ only because we are considering it as an Itô process [54].

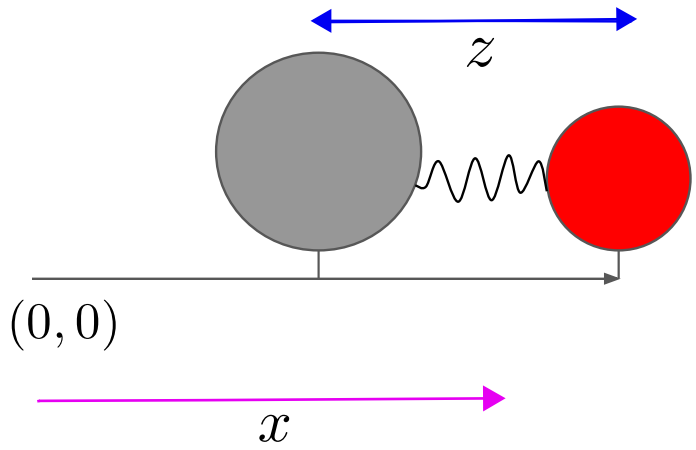

Figure 2.2: Schematic of a dimer after coordinate transformation in one dimension.

In dynamics (2.1.2), the configuration space (z-space) has decoupled from that of CM of the system. Importantly, the equilibrium fluctuations are determined solely by the configuration variable z in this model, making it the primary coordinate governing the system's thermal noise characteristics. Thus, one could write the equilibrium distribution function using the corresponding Fokker-Planck equation.

The equilibrium distribution of the configuration coordinate z, according to a standard Itô process (see Appendix D), under the condition of detailed balance [23, 42, 44, 45, 55, 56] being

$$\begin{aligned} P(z) &= \frac{A}{k_B T\left(\frac{1}{\Gamma_1(z)}+\frac{1}{\Gamma_2(z)}\right)} e^{-V(z)/k_B T} \\ &= \frac{A}{D(z)} e^{-V(z)/k_B T}, \end{aligned} \tag{2.1.3}$$

where A is a normalization constant, and $D(z) = k_B T\left(\frac{1}{\Gamma_1(z)}+\frac{1}{\Gamma_2(z)}\right)$ is effective diffusivity of the dimer in configuration space. The average velocity of the configuration variable and centre of mass, which are functions of the internal/configuration coordinate (z), are then evaluated using the equilibrium distribution of the configuration coordinate. We define $\langle \mathcal{G}(z)\rangle = \int_{z_1}^{z_2} \mathcal{G}(z)P(z)dz$, where $\mathcal{G}(z)$ is an arbitrary function.

Now, we evaluate the average velocity of the internal coordinate, where the configuration space is within the range z_1 to z_2 (say) in thermal equilibrium.

$$\begin{aligned} \left\langle \frac{dz}{dt} \right\rangle &= -\left\langle \left[\frac{1}{\Gamma_1(z)}+\frac{1}{\Gamma_2(z)}\right]\frac{dV(z)}{dz}\right\rangle \\ &= -\int_{z_1}^{z_2}\left[\frac{1}{\Gamma_1(z)}+\frac{1}{\Gamma_2(z)}\right]\frac{dV(z)}{dz}P(z)\,dz \\ &= -\int_{z_1}^{z_2}\frac{A}{k_B T}\frac{dV(z)}{dz}e^{-V(z)/k_B T}\,dz \\ &= A\int_{z_1}^{z_2}\frac{d}{dz}[e^{-V(z)/k_B T}]dz \\ &= A\int_0^0 d[e^{-V(z)/k_B T}] \equiv 0. \end{aligned} \tag{2.1.4}$$

where $e^{-V(z)/k_B T}$ vanishes at $V(z)\to\infty$ at $z = z_1, z_2$ with respect to finite energy

scale corresponding to thermal noise. The presence of a non-zero average current in configuration space will produce entropy, violating the condition of detailed balance in thermal equilibrium. Thus, the vanishing of average current or velocity of the internal coordinate z for any confining potential ensures the stationarity of the distribution, and ensures the system has equilibrated in z space.

Next, we evaluate the average CM velocity of the system using the equilibrium distribution.

$$\begin{aligned} v = \left\langle \frac{dx}{dt} \right\rangle &= -\frac{1}{2} \left\langle \left[\frac{1}{\Gamma_1(z)} - \frac{1}{\Gamma_2(z)} \right] \frac{dV(z)}{dz} \right\rangle \\ &= -\frac{1}{2} \int_{z_1}^{z_2} \left[\frac{1}{\Gamma_1(z)} - \frac{1}{\Gamma_2(z)} \right] \frac{dV(z)}{dz} P(z)\, dz \\ &= -\frac{1}{2} \int_{z_1}^{z_2} \frac{A}{k_B T} \left(\frac{\Gamma_2(z) - \Gamma_1(z)}{\Gamma_2(z) + \Gamma_1(z)} \right) \frac{dV(z)}{dz} e^{-V(z)/k_B T}\, dz \\ &= \frac{A}{2} \int_{z_1}^{z_2} dz \left[\left(\frac{\Gamma_2(z) - \Gamma_1(z)}{\Gamma_2(z) + \Gamma_1(z)} \right) \frac{d}{dz} [e^{-V(z)/k_B T}] \right] \neq 0 \end{aligned} \tag{2.1.5}$$

The term $\left[\frac{1}{\Gamma_1(z)} - \frac{1}{\Gamma_2(z)}\right]$ is the *structural symmetry breaking* term. It's evident that when there is broken structural symmetry, that is $\Gamma_1(z) \neq \Gamma_2(z)$ in the presence of a confining potential $V(z)$, the CM can attain a nonzero steady velocity.

The Vanishing of internal current, $\left\langle \frac{dz}{dt} \right\rangle \equiv 0$, in general, for any choice of Γ_i and $V(z)$ ensures thermal equilibrium, where nonzero uniform centre of mass current, $\left\langle \frac{dx}{dt} \right\rangle$ is resulting in a Galilean transformation of the frame which will not disturb any equilibrium physics.

It is important to note that constant damping $\Gamma_1 \neq \Gamma_2$ alone cannot break the symmetry of the system to produce net CM motion. The responses of the dimer's constituents (for constant unequal damping) remain equal and opposite during both attractive (confining) and repulsive (excluded volume) interactions. This symmetry in the response ensures that any fluctuation-driven motion remains reversible over long timescales, preventing the emergence of sustained, directed motion. One can also see from above that when damping coefficients are constants but unequal, $\left\langle \frac{dx}{dt} \right\rangle \propto \int_0^0 d[e^{-V(z)/k_B T}] \equiv 0$, where $e^{-V(z)/k_B T}$ vanishes at $V(z) \to \infty$ at $z = z_1$, z_2 with respect to finite energy scale corresponding to thermal noise. This is why homogeneous diffusion is not seen to result in any directed motion, whereas a non-

homogeneous diffusion can. To validate the analytical predictions, we compare them with numerical simulations in the next section:

2.2 Comparison with Simulation

The damping function is modeled as a linear combination of the Heaviside/unit-step function Θ. The Heaviside function is zero for negative arguments and unity otherwise. We choose damping function: $\Gamma_i(z) = \gamma_i\Theta(z-z_{min})+\mu_i(1-\Theta(z-z_{min}))$, where μ_i and γ_i break the damping symmetry by differing below and above z_{min}.

$$\Gamma_i(z) = \begin{cases} \mu_i, & z < z_{min} \\ \gamma_i, & z \geq z_{min} \end{cases}$$

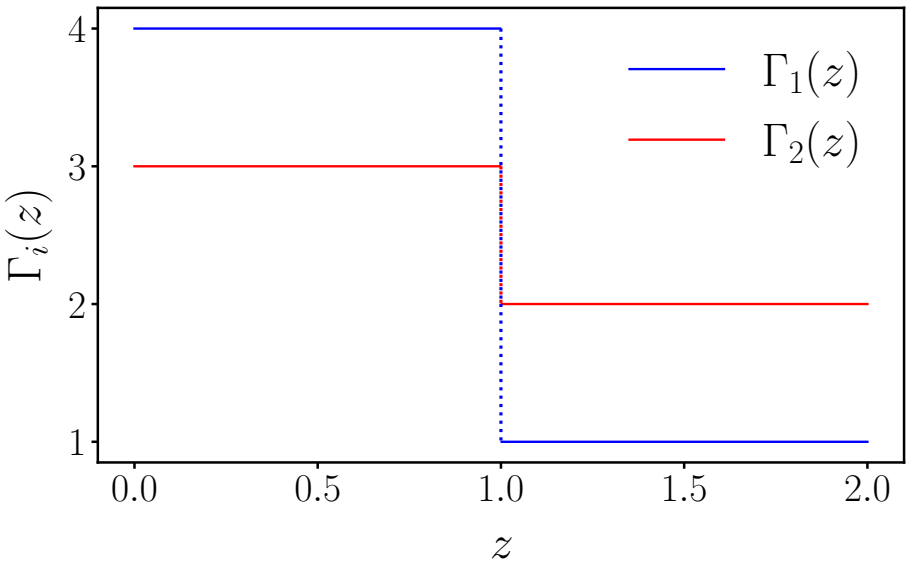

Figure 2.3: Variation of damping coefficient as a function of the internal coordinate for both constituents, used in the simulation. The parameters used are $\gamma_1 = 1$, $\gamma_2 = 2$, $\mu_1 = 4$, $\mu_2 = 3$ and $z_{min} = 1$.

The intra-dimer potential $V(z)$ is modeled by a harmonic potential in the simulations. $V(z) = \frac{\alpha}{2}(z - z_{min})^2$, which is repulsive below equilibrium separation z_{min} and attractive above it. α is the spring constant and represents the strength of intra-dimer interaction.

2.3 Simulation units to Physical units

In our simulations, the reference length scale $r_{\min}$ and the thermal energy scale k_BT are set to unity. Consequently, all lengths (such as particle positions and interparticle separations) are expressed in units of $r_{\min}$, and all energies in units of k_BT. We also choose the damping coefficients Γ_i to be of order unity, ensuring that the corresponding diffusivities $D_i = \frac{k_BT}{\Gamma_i}$ are also of order unity in simulation units.

To relate the simulation units to physical units, consider a micron-sized particle immersed in water. In such a system, $r_{\min}$ corresponds to the particle radius (approximately 1μm), and $k_BT \approx 4\times10^{-21}$ J at room temperature (300 K). With water viscosity $\eta \approx 10^{-3}$ Pa.s, the Stokes drag is given by $\Gamma = 6\pi\eta r_{\min} \approx \times10^{-8}$ kg/s. A unit of damping in simulation units corresponds to a damping of 10^{-8} kg/s for a micron-sized particle in physical units. Equivalently, a diffusivity $D \sim 1$ in simulation units corresponds to a real diffusivity of order

$$D = \frac{k_BT}{\Gamma} \approx \frac{10^{-21}}{10^{-8}} = 10^{-13}\,\mathrm{m}^2/\mathrm{s},$$

The parameter values used throughout the simulations are listed in Table 5.1. These values are kept constant across all simulations, unless stated otherwise.

Symbol	Parameter	Simulation value
k_BT	Thermal energy	1
$r_{\min}$	Reference length scale	1
γ_1	Damping coefficient	1
γ_2	Damping coefficient	2
μ_1	Damping coefficient	4
μ_2	Damping coefficient	3
α	Bond stiffness (intra-dimer)	100
Δt	Integration time step	10^{-4}

Table 2.1: Fixed simulation parameters (in dimensionless/simulation units)

We now, present the results for the symmetry-broken dimer system in Fig. 2.4, which illustrate the system's behavior under Heaviside function damping. Fig. 2.4(a) demonstrates an excellent agreement between the simulated and theoretical probability density (denoted by $\rho(z)$, instead of $P(z)$ here). The presence of the Heaviside

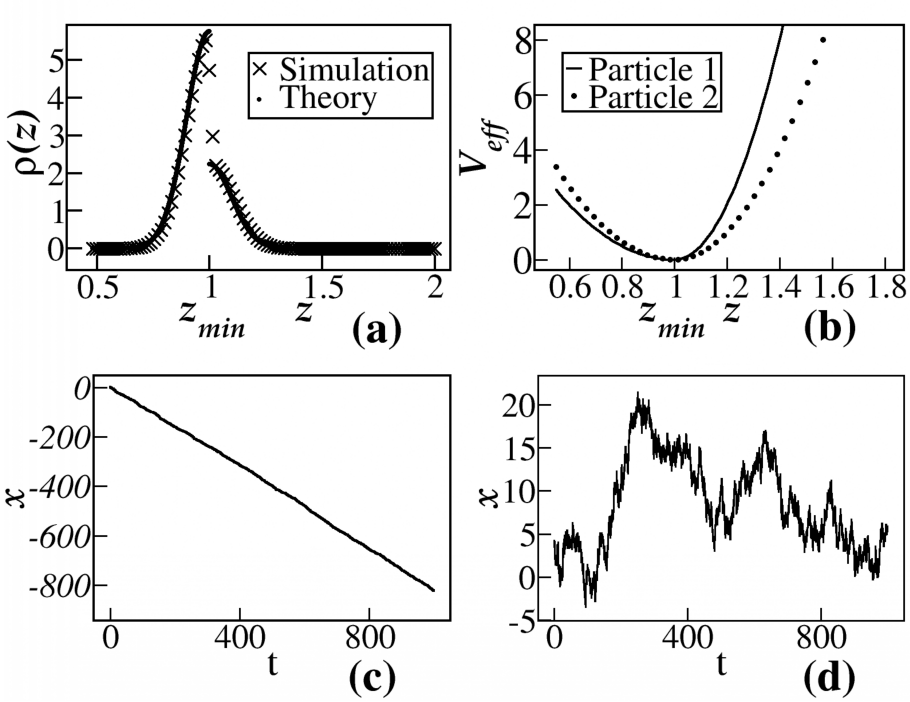

Figure 2.4: System behavior with Heaviside-function damping. (a) Matching of simulated and analytical Itô probability density. (b) Asymmetric effective potential of constituents. (c) Directed motion of the center of mass (CM) due to broken symmetry. (d) No net CM motion in the symmetry-unbroken case, $\gamma_1 = \gamma_2 = 1, \mu_1 = \mu_2 = 3$.

function in the damping term causes a discontinuous change in diffusivity around z_{min}, leading to a discontinuity in the probability density at z_{min}. Fig. 2.4(b) illustrates the effective potential $(V(z)/\Gamma_i(z))$ experienced by each particle both below and above the equilibrium separation. Due to the asymmetry in the effective potentials experienced by the constituents on either side of z_{min} (consequence of differential response of damping below and above z_{min}), directed transport emerges, as shown in Fig. 2.4(c). Finally, Fig. 2.4(d) depicts a scenario where no structural symmetry breaking occurs (damping symmetry remains unbroken). In this case, the system exhibits purely Brownian fluctuations, resulting in no net transport. We use the following damping parameters $\gamma_1 = \gamma_2 = 1, \mu_1 = \mu_2 = 3$ to generate Fig. 2.4(d), keeping the remaining parameters unchanged.

2.4 Physics of the Symmetry-Broken Hetero-dimer Model

Being in the overdamped limit, the internal forces (corresponding to confining potential) get rescaled by their respective damping coefficients (Eq. 2.1.1). Broken damping symmetry disrupts the balance of these rescaled forces. The effective potential of one monomer becomes steeper than the other. This breaks the inversion symmetry and creates a force imbalance $-\frac{1}{2}\left[\frac{1}{\Gamma_1(z)} - \frac{1}{\Gamma_2(z)}\right]\frac{dV(z)}{dz}$, on average in the configuration space as seen in Eq.(2.1.2). This physically means that monomer with higher damping loses more momentum in comparison to one with lower damping, creating a net force imbalance. This force imbalance induces motion. However, in the overdamped regime, a net force cannot persist. Instead, this imbalance is exactly counteracted by the system's overall damping, on average, allowing the dimer to move with a steady velocity in a force-free manner, driven by homogeneous, isotropic bath fluctuations. The symmetry-broken dimer thus filters the Brownian fluctuation to produce rectified transport [51].

At this point, it becomes important to discuss the sources of energy and energy conservation. Our system is a passive system with no active source for propulsion, like an external force, active force, or external energy source. Our system has broken damping symmetry and is placed in a homogeneous, isotropic heat bath. The heat bath continuously injects energy via thermal fluctuations. Let's closely examine what is happening in our system:

Step 1: Initial Condition ($t = 0$). Suppose the dimer is placed in a homogeneous, isotropic thermal bath at temperature T. The bath consists of randomly colliding molecules, which impart stochastic forces (thermal noise) to the two monomers of the dimer.

Step 2: Early Dynamics ($t > 0$) Each monomer experiences random thermal kicks from the bath, representing the injection of energy from the environment. Due to the broken damping symmetry, the two monomers dissipate this injected energy and momentum at different rates. The monomer with higher damping acts like a *strong sink*, quickly converting the injected (stochastic) kinetic energy into heat and

dissipating it back to the bath. As a result, the monomer with higher damping loses momentum faster, responding more sluggishly to the thermal kicks. The monomer with lower damping, by contrast, dissipates energy at a slower rate and retains its momentum towards the other constituent particle for a longer duration, making it more responsive to fluctuations and responds more efficiently to the stochastic kicks. This differential response creates an imbalance: the less-damped monomer undergoes larger displacements inward compared to the more-damped one. In a system with inertia, this would result in acceleration, but in the overdamped limit, inertia is negligible, and by definition, the system cannot sustain a net force. Instead, this force imbalance is immediately countered by the overall damping of the system, on average, ensuring that velocity evolves smoothly rather than accelerating indefinitely. The overdamped limit corresponds to $m \to 0$, $\zeta \to \infty$, such that $\Gamma = m\zeta$ is finite. ζ^{-1} is the velocity relaxation timescale. This process occurs on a time scale $\zeta^{-1} = \frac{m}{\Gamma}$. This implies that the system relaxes to equilibrium almost instantaneously, allowing the velocity to adjust immediately to any force imbalance without any inertial delay in comparison to other time scales in the overdamped limit.

Step 3: Emergence of Steady Directed Motion The system thus reaches a steady state where both monomers are in dynamic "mechanical" equilibrium while thermal energy is continuously injected by the bath, it is also being dissipated back into the bath by the same amount, on average. This creates a constant, steady velocity in one direction.

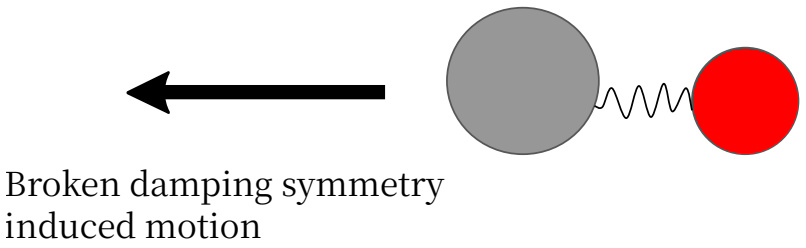

Figure 2.5: Schematic of symmetry broken dimer exhibiting directed motion in 1D driven by isotropic, homogeneous thermal fluctuations.

The following section provides a deeper examination of energy conservation, energy extraction, and consistency with the laws of Thermodynamics.

2.5 Perpetual motion Vs Perpetual motion machine

The dimer system exhibits persistent directed motion in equilibrium, but it is not a perpetual motion machine. Using both the terms interchangeably can create a source of confusion. Let's clarify this:

Perpetual Motion: A perpetual motion system refers to an object that moves indefinitely.

Perpetual Motion Machine: A hypothetical device that operates indefinitely without an external energy source. There are two main types:

1. **First Kind:** A machine that produces more energy than it consumes, effectively creating energy from nothing. It would keep running forever without any energy input, directly violating the **First Law of Thermodynamics**. Example: A wheel that spins indefinitely without any external force or energy source.

2. **Second Kind:** A machine that extracts useful work solely from equilibrium thermal fluctuations, without any external gradient. This type violates the **Second Law of Thermodynamics**. Example: An engine that continuously extracts work from a single temperature bath without expelling heat.

Does our system violate the laws of Thermodynamics?

The First law of thermodynamics states that: *Energy is conserved and heat and work are both forms of energy.*

The Kelvin-Planck statement of the second law of thermodynamics states that:

It is impossible to construct a cyclic device (or a device operating in a cycle) that functions as a heat engine and converts all the heat absorbed from a single reservoir entirely into work without any other effect.

First, our system does not extract energy. The rectified motion observed in our model arises from an interplay between thermal fluctuations and asymmetric dissipation, but it does not correspond to the extraction of useful work.

Since we are considering a closed composite system consisting of the dimer and the heat bath, no energy is being extracted from the composite system by any

third agent, ensuring energy conservation. Any attempt to extract energy from the composite system by third agent would initiate a transient process in which the bath would begin to lose temperature, as no real bath has infinite heat capacity. The transient would persist until the bath temperature drops to a point where the dimer's velocity (roughly being proportional to the square root of the temperature [51]) is no longer sufficient to drive dimer against a barrier. In such a case, the dimer would come to rest. Therefore, there can be no perpetual extraction of energy enabling the dimer to move indefinitely against a global barrier. Thus, perpetual energy extraction is impossible, meaning the system cannot generate continuous work against some global barrier or some external agent.

In the absence of external agent, since no net energy is harvested from the bath in a way that could be used to perform external work, the symmetry-broken dimer system does not function as a heat engine. Therefore, the model remains consistent with the laws of Thermodynamics. The symmetry-broken dimer moves in perpetual motion but is not a perpetual motion machine of the second kind and remains consistent with the laws of thermodynamics.

2.6 Detailed Balance

Detailed balance is a fundamental principle of equilibrium systems, ensuring that microscopic transition rates between states remain symmetric. However, the dimer model presents an intriguing case, an equilibrium system exhibiting persistent directed motion. This raises the question: *Does detailed balance still hold in such a scenario?*

To understand why the uniform motion of a symmetry-broken dimer in equilibrium does not violate this condition, we analyze the underlying physics. Our model is inhomogeneous in the configuration frame. In our model, the interaction potentials depend only on relative coordinates between particles, and not on their absolute positions. Importantly, this coordinate-dependent damping does *not* necessarily break equilibrium or violate detailed balance. As shown rigorously within the Itô interpretation of stochastic dynamics, we obtain a steady-state distribution that by setting *local probability current to zero*, thus satisfying detailed balance even in the presence of inhomogeneous damping. The equilibrium distribution $P(z)$

becomes:

$$P(z) = \frac{A}{D(z)} \exp\left(-\frac{V(z)}{k_B T}\right),$$

where $D(z)$ is the position-dependent diffusivity (inversely related to damping) and $V(z)$ is potential associated with system and A is a normalisation constant. This distribution compensates for the dynamical inhomogeneity and maintains equilibrium.

Moreover, the heat bath is assumed to be *homogeneous* (identical properties everywhere) and *isotropic* (exhibiting the same behavior in all directions). These properties ensure that the bath does not distinguish between different absolute positions or orientations of the system and does not favor any particular direction of motion. Because of this, the bath does not impose a preferred reference frame, meaning that the system's *center-of-mass motion* is just as valid as any other Galilean state. Consequently, the probability of finding the center of mass at any location remains constant, ensuring that equilibrium conditions are maintained.

Since the system operates in the *overdamped regime*, the *net force is zero* in equilibrium. However, a *steady nonzero velocity* can still exist. The *entropy production rate*, given by the product of force and flux, remains zero because the net force is zero. This implies that *no entropy* is produced, and the entropy remains constant. Another way to say it is, a symmetry-broken dimer moving with a constant average velocity in a heat bath does not exchange energy with the bath, on average. The thermal properties of the bath remain unchanged, and no additional entropy is being generated.

Thus, the *dimer* system can remain in a state of *mechanical equilibrium* (net force is zero), while also maintaining *thermal equilibrium*. This shows that a symmetry broken mesoscopic object moving with constant velocity *does not* disturb the equilibrium state of the bath.

2.7 Discussion on Feynman-Smoluchowski-Lippmann Ratchet

Often, it has been argued in the literature that the Feynman-Smoluchowski-Lippmann ratchet often prohibits the possibility of rectified transport in equilibrium.

We address the following below.

The Smoluchowski–Feynman-Lippmann ratchet [57] is a well-known thought experiment originally introduced by Lippmann, studied further by Smoluchowski, and popularised by Feynman, which was proposed to investigate the possibility of extracting useful work from thermal fluctuations, exploring the possibility of violating the second law of thermodynamics. The device consists of a ratchet and pawl system connected to vanes immersed in a heat bath. The ratchet is intended to convert random thermal kicks into directed motion, thereby creating the illusion of work extraction from equilibrium thermal noise.

Feynman's analysis showed that such a device cannot produce directed motion without an external temperature gradient. If the system is in thermal equilibrium, thermal fluctuations from both sides are statistically balanced, and no net motion occurs. This conclusion is consistent with the second law, as the absence of a temperature gradient ensures that entropy production remains zero on average.

However, this analysis is based on systems where symmetry is either unbroken or broken solely through temperature differences. Our model introduces a distinct mechanism of symmetry breaking: damping asymmetry in the absence of temperature gradients. Unlike the Smoluchowski–Feynman ratchet, where temperature asymmetry drives directed motion, our model employs spatially varying damping to maintain a constant average velocity in thermal equilibrium. Importantly, in our system, the average velocity emerges due to the broken-symmetry in the dissipation landscape, not due to an external drive or temperature gradient.

2.8 Conclusion

In this chapter, we show that a simple symmetry broken structured object can remain in state of *mechanical equilibrium* and show *directed transport* in a state of thermal equilibrium. This work points towards the possibility of time reversal symmetry-broken equilibrium state, like that of macroscopic bodies following Newton's first law, or like that in a dissipation-less super current. Such a uniform motion can exist in equilibrium because the system moves in a force-free condition.

3

Symmetry-Broken Dimer model in Presence of a Force

In the previous chapter, we examined how a symmetry-broken dimer can filter Brownian motion and generate directed transport by harnessing fluctuations from a homogeneous, isotropic heat bath in equilibrium in one dimension. However, we established that an external agent cannot extract energy from the bath perpetually. Any attempt to extract energy would drive the system out of equilibrium, causing a local temperature drop in the bath and triggering heat and material transport within the bath, leading to entropy production. This would happen until the bath reaches a temperature, below which the velocity of dimer would not be sufficient to drive against the barrier.

In this chapter, we consider a situation in which our heat bath is thermally connected to a much bigger reservoir (surrounding), which replenishes it all the time by exchanging energy so that its temperature doesn't fall and its equilibrium is maintained. This would be a non-equilibrium steady state. For example, consider a water tank exposed to sunlight. Here, the water tank acts as the bath, while the sun establishes its coupling to the larger environment. The exposure to sunlight can maintain the water tank at a nearly constant temperature over a long timescale, even as the bath (water tank) loses energy to a system immersed in it. We explore how the coupling between thermal fluctuations from a heat bath, which is maintained at

a constant fixed temperature (courtesy of its interaction with a bigger reservoir) and a symmetry-broken mesoscopic structure, can enable efficient heat-to-work conversion (enable energy extraction) in the presence of an external load. In our analysis, we employ an overdamped model, which necessarily describes a slow process. This approach is common in modeling such systems because, even under non-equilibrium conditions, one can still meaningfully define thermodynamic quantities like temperature for slow processes. This chapter is adapted from Ref. [52].

3.1 Symmetry-Broken Dimer Model in Presence of a Force

Consider a structural symmetry broken dimer constrained in one-dimensional space with monomer's coordinates x_1 and x_2 ($x_1 > x_2$), configuration-dependent damping coefficients $\Gamma_i(z)$, $i \in \{1, 2\}$, in contact with an isotropic, homogeneous heat bath in thermal equilibrium at temperature T. Monomers are bound by an attractive potential, and at short distances, there acts a repulsive potential which prevents the particles from passing through each other. The constituents obey local Stokes-Eintein relation, $D_i(z) = k_B T/\Gamma_i(z)$, $z = x_1 - x_2$ is configuration coordinate, $D_i(z)$ is configuration dependent diffusivity of the i^{th} constituent. $\eta_i(t)$ is Gaussian white noise associated with i^{th} constituent, of unit strength with zero mean $\langle \eta_i(t) \rangle = 0$ and no temporal and inter-particle correlation i.e. $\langle \eta_i(t_1)\eta_j(t_2) \rangle = \delta_{ij}\delta(t_1 - t_2)$. F is a constant external global force against which the dimers move. The time scale of the dynamics that we are considering here is larger than the time scale over which the temperature and the diffusivity gets defined and, therefore, it is an overdamped dynamics.

The following equations governs the dynamics of monomers of a dimer:

$$\begin{aligned} \frac{dx_1}{dt} &= \frac{1}{\Gamma_1(z)}\Big[F - \frac{\partial V(z)}{\partial x_1}\Big] + \sqrt{\frac{2k_BT}{\Gamma_1(z)}}\,\eta_1(t), \\ \frac{dx_2}{dt} &= \frac{1}{\Gamma_2(z)}\Big[F - \frac{\partial V(z)}{\partial x_2}\Big] + \sqrt{\frac{2k_BT}{\Gamma_2(z)}}\,\eta_2(t). \end{aligned} \tag{3.1.1}$$

A simple coordinate transformation to the center of mass (CM) $x = \frac{x_1+x_2}{2}$ and

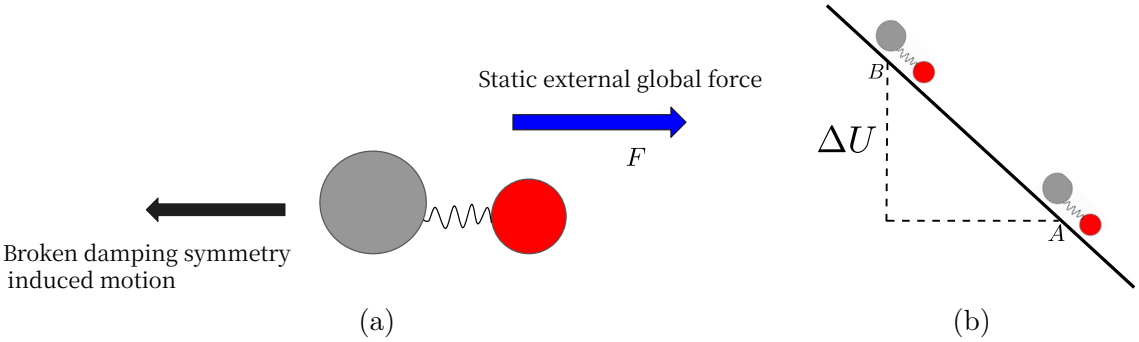

Figure 3.1: (a) Schematic showing ratcheting of dimer against external force. (b) Exact same motion shown in the potential landscape. The tilted black line corresponds to the potential due to the global force. As the dimer moves uphill against the global force from A to B, it gains mechanical (potential) energy.

internal coordinate frame $z = x_1 - x_2$, one can rewrite the equation as:

$$\begin{aligned}\frac{dz}{dt} &= F\left[\frac{1}{\Gamma_1(z)} - \frac{1}{\Gamma_2(z)}\right] - \left[\frac{1}{\Gamma_1(z)} + \frac{1}{\Gamma_2(z)}\right]\frac{dV(z)}{dz} + \xi_z(z,t),\\ \frac{dx}{dt} &= \frac{F}{2}\left[\frac{1}{\Gamma_1(z)} + \frac{1}{\Gamma_2(z)}\right] - \frac{1}{2}\left[\frac{1}{\Gamma_1(z)} - \frac{1}{\Gamma_2(z)}\right]\frac{dV(z)}{dz} + \xi_x(z,t). \quad (3.1.2)\end{aligned}$$

where the stochastic noise's, $\xi_z(z,t) = \sqrt{2k_BT}\left[\frac{\eta_1(t)}{\sqrt{\Gamma_1(z)}} - \frac{\eta_2(t)}{\sqrt{\Gamma_2(z)}}\right]$ and $\xi_x(z,t) = \sqrt{k_BT}\left[\frac{\eta_1(t)}{\sqrt{2\Gamma_1(z)}} + \frac{\eta_2(t)}{\sqrt{2\Gamma_2(z)}}\right]$ are linear combination of white noise, such that the auto-correlation of noise at various times is $\langle\xi_z(z,t_1)\xi_z(z,t_2)\rangle = 2k_BT\left(\frac{1}{\Gamma_1(z)} + \frac{1}{\Gamma_2(z)}\right)\delta(t_1 - t_2)$ and $\langle\xi_x(z,t_1)\xi_x(z,t_2)\rangle = \frac{k_BT}{2}\left(\frac{1}{\Gamma_1(z)} + \frac{1}{\Gamma_2(z)}\right)\delta(t_1 - t_2)$.

The dynamics of z can also be written as:

$$\frac{dz}{dt} = \left[F\frac{\Gamma_2(z) - \Gamma_1(z)}{\Gamma_2(z) + \Gamma_1(z)} - \frac{dV(z)}{dz}\right]\left[\frac{1}{\Gamma_1(z)} + \frac{1}{\Gamma_2(z)}\right] + \xi_z(z,t). \quad (3.1.3)$$

We again recognize the complete decoupling of CM coordinate from internal coordinate. The Smoluchowski equation resulting from the standard Kramers-Moyal expansion for the internal coordinate is of the form (see Appendix D)

$$\begin{aligned}\frac{\partial P(z,t)}{\partial t} &= -\frac{\partial}{\partial z}\left[h(z)P(z,t) - \frac{\partial D(z)P(z,t)}{\partial z}\right] \\ &= -\frac{\partial J(z,t)}{\partial z}.\end{aligned} \tag{3.1.4}$$

In the above equation, $P(z,t)$ is the probability density, and $h(z)$ is the drift velocity. We find that for our model,

$$\begin{aligned}h(z) &= \left(F\frac{\Gamma_2(z)-\Gamma_1(z)}{\Gamma_2(z)+\Gamma_1(z)} - \frac{dV(z)}{dz}\right)\left(\frac{1}{\Gamma_1(z)}+\frac{1}{\Gamma_2(z)}\right) \\ &= \frac{1}{k_BT}\left(F\frac{D_2(z)-D_1(z)}{D_2(z)+D_1(z)} - \frac{dV(z)}{dz}\right)\Big(D_1(z)+D_2(z)\Big).\end{aligned} \tag{3.1.5}$$

and $D(z) = k_BT\left(\frac{1}{\Gamma_1(z)}+\frac{1}{\Gamma_2(z)}\right) = D_1(z)+D_2(z)$, is the effective diffusivity for the internal coordinate.

We observe that the CM coordinate x has decoupled from the internal coordinate z even under the influence of a global force. Now, we assume that this external force is sufficiently weak, ensuring that the system operates within the linear response regime. In this regime, the equilibrium probability density provides a reasonable approximation for evaluating physical quantities near equilibrium. Accordingly, we set the current density in configuration space to zero ($J(z) = 0$), as the system remains close to equilibrium. The following distribution (near equilibrium or weakly-non equilibrium) $P(z)$ emerges:

$$\begin{aligned}P(z) &= \frac{A}{D(z)}\exp\left(\frac{\int_{z_1}^{z} dz'\left(F\frac{\Gamma_2(z')-\Gamma_1(z')}{\Gamma_2(z')+\Gamma_1(z')} - \frac{dV(z')}{dz'}\right)}{k_BT}\right) \\ &= \frac{A}{D(z)}e^{-V(z)/k_BT}e^{\int_{z_1}^{z} dz'(F/k_BT)\frac{D_2(z')-D_1(z')}{D_2(z')+D_1(z')}}\end{aligned} \tag{3.1.6}$$

where A is a normalization factor. Note that we assume that the configuration

space is within range z_1 to z_2 (say).

The stationarity of the distribution is ensured by the fact that the average internal current identically vanishes

$$\langle\frac{dz}{dt}\rangle = A \times \int_{z_1}^{z_2} dz \frac{d}{dz} \exp \frac{\int_{z_1}^{z} dz' \left(F\frac{\Gamma_2(z')-\Gamma_1(z')}{\Gamma_2(z')+\Gamma_1(z')} - \frac{dV(z')}{dz'}\right)}{k_B T} \equiv 0 \tag{3.1.7}$$

under the consideration that the Boltzmann factor $\exp\left(\int_{z_1}^{z} dz' \left(F\frac{\Gamma_2(z')-\Gamma_1(z')}{\Gamma_2(z')+\Gamma_1(z')} - \frac{dV(z')}{dz'}\right)/k_B T\right)$ vanishes at $z = z_1$ and at $z = z_2$ with respect to finite energy scale.

Now, the average CM velocity v becomes:

$$v = \langle\frac{dx}{dt}\rangle = \left\langle \frac{F}{2}\left[\frac{1}{\Gamma_1(z)} + \frac{1}{\Gamma_2(z)}\right]\right\rangle + \left\langle \frac{-1}{2}\frac{dV(z)}{dz}\left[\frac{1}{\Gamma_1(z)} - \frac{1}{\Gamma_2(z)}\right]\right\rangle. \tag{3.1.8}$$

The first term $\left\langle \frac{F}{2}\left[\frac{1}{\Gamma_1(z)} + \frac{1}{\Gamma_2(z)}\right]\right\rangle$ in the above equation represents the motion induced by global force and will always drive system downhill the global potential.

The second term $\left\langle \frac{-1}{2}\frac{dV(z)}{dz}\left[\frac{1}{\Gamma_1(z)} - \frac{1}{\Gamma_2(z)}\right]\right\rangle$ as seen in previous chapter represents the motion due to broken structural symmetry and will only produce a center of mass motion when there is the structural symmetry breaking present i.e. $\Gamma_1(z) \neq \Gamma_2(z)$. By the adjustment of the values of $\Gamma_1(z)$ and $\Gamma_2(z)$ (or, more physically, the Stokes radii of the particles) we can make this part of the center of mass motion to counteract or even overcome that due to the global force and make the system move against the global force. In such a scenario, the thermal energy of the bath would be directly converted into the potential energy of the system as shown in Fig. 3.1(b), where dimer moves from A to B uphill against the global potential and gains potential energy.

Note that from the expression of average centre of mass velocity (Eq. 3.1.8), there exists a critical value of force at which the transport due to force is counterbalanced by that due to that of broken-symmetry. In such a situation, the system would come to a halt. The value of that particular force at which this happens is called *stall force* F_{stall}. In the context of energy extraction, efficiency is meaningful only for force

values less than or equal to the stall force. For $F > F_{\text{stall}}$, the dimer moves along the direction of the applied force, precluding any possibility of extracting useful work from thermal fluctuations. The efficiency of a dimer in working against the force F is the ratio of available power output and thermal energy per unit time. We define the efficiency as $\eta = \frac{|Fv|}{k_B T}$. We next turn to a detailed comparison of simulation and analytical results.

3.2 Simulation Results

The parameters used in the simulation remain the same as shown in the previous chapter in table 5.1(unless stated otherwise). In this chapter of the thesis, we have an additional parameter global static force F, which has been fixed to 1.5 in the simulations.

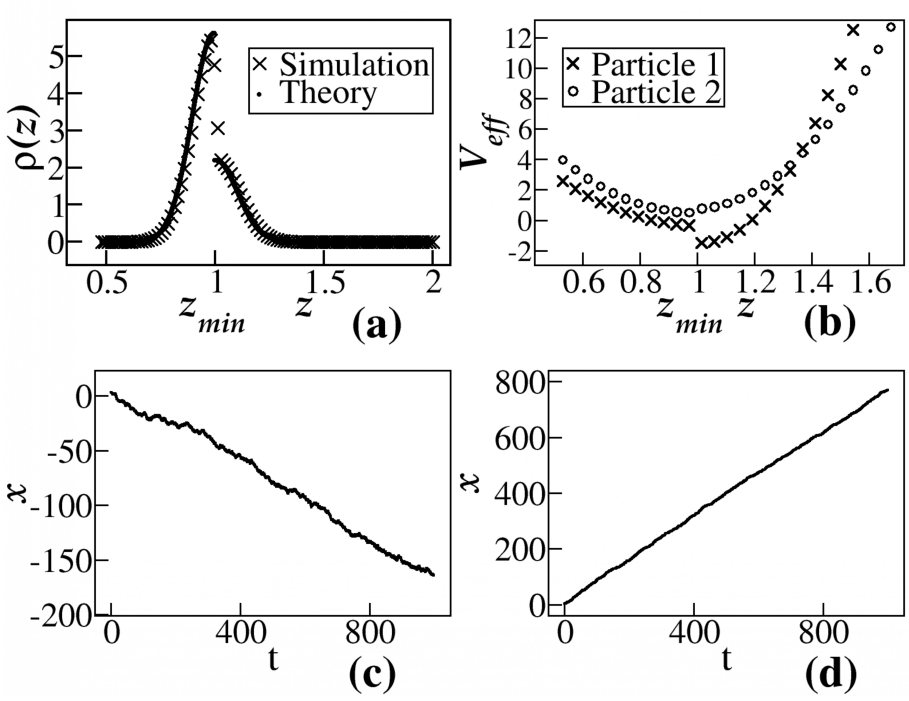

Figure 3.2: System behavior with Heaviside-function damping for $F = 1.5$. (a) Probability density, (b) Effective potential, and (c) Directed motion of CM are shown. (d) Force-driven motion of CM in the positive direction for symmetry unbroken dimer (symmetrical damping coefficients) $\gamma_1 = \gamma_2 = 1, \mu_1 = \mu_2 = 3$ and $F = 1.5$.

A unit force in simulation for a micron sized particle corresponds to $k_BT/r_{min} = 10^{-21}/10^{-6} = 10^{-15}N$ in physical units. We now compare the analytical results with the simulation ones in the next section to validate our analysis.

The probability density obtained from simulations is in quantitative agreement with the analytical Itô solution when an external force is applied as shown in Fig. 3.2(a). This agreement serves as a key validation, indicating that the externally applied force chosen in the simulation is small enough for the system to operate within the linear response regime. The presence of external force F changes the effective potential experienced by each constituent $\frac{1}{\Gamma_i(z)}\int dz[\frac{dV}{dz} + (-1)^i F]$, as shown in Fig. 3.2(b). Comparing this force-modified effective potential to the one in the absence of force (see Fig. 2.4(b)) from the previous chapter), one observes a clear change in the potential landscape. As a consequence of this altered landscape, the CM travels a shorter distance than in the zero force case, as depicted in Fig. 3.2(c) compared to Fig. 2.4(c).

Now, it was evident from Fig. 2.4(d) in the previous chapter that a *symmetry unbroken* dimer would show no net motion in the absence of an external force. However, in its presence, the *symmetry unbroken* dimer moves systematically in the direction of force in the positive x direction as visible from Fig. 3.2(d) for the same set of parameters except $F = 1.5$. Thus, the external force tends to drive the dimer in the positive x direction.

In the context of a dimer broken by symmetry, the motion induced by external force opposes the direction of motion induced by symmetry breaking in Fig. 2.4(c), which again explains why the dimer travels a shorter distance in the current case (Fig. 3.2(c)) compared to the zero external force scenario shown in previous chapter in Fig. 2.4(c).

We compile the results from various regimes together in the Fig. 3.3 to compare the motion of the center of mass for both symmetry-broken and symmetry-unbroken dimers, under equilibrium (or weakly non-equilibrium) as well as under the application of a weak external force. This comparative visualization helps clarify the differences in their dynamical behavior. The damping parameters for the symmetry-unbroken dimer used are $\gamma_1 = \gamma_2 = 1, \mu_1 = \mu_2 = 3$, whereas the parameters for the symmetry-broken dimer are $\gamma_1 = 1, \gamma_2 = 2, \mu_1 = 4, \mu_2 = 3$. The rest of

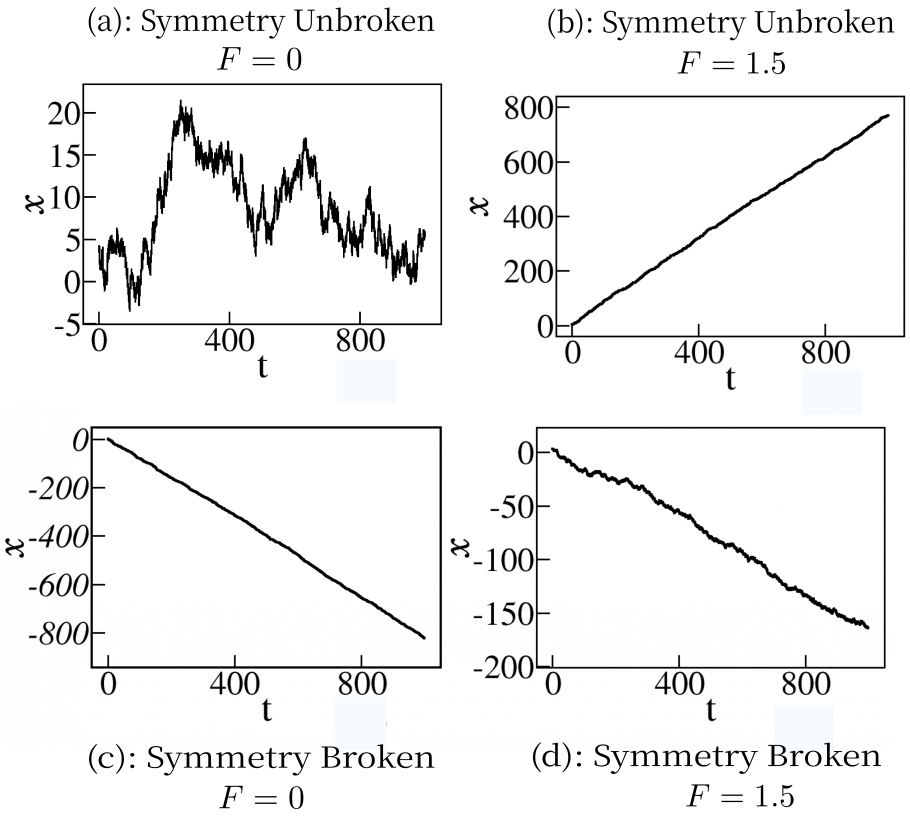

Figure 3.3: Trajectories of dimer shown under varying external forces and damping symmetries. (a) $F = 0$ and symmetrical damping: no net motion, (b) $F = 1.5$ and symmetrical damping: net drift in positive x direction, (c) $F = 0$ and Broken symmetry: net motion in negative x direction (d) $F = 1.5$ and broken symmetry: damping asymmetry drives motion left while force drives it right; the competition results in net motion toward negative with less displacement.

the simulation parameters are the same as stated in table 5.1. In the absence of external force, a symmetry-unbroken dimer exhibits purely Brownian motion with no net displacement, as evident from Fig. 3.3(a). Upon applying an external force, as shown in Fig. 3.3(b), the symmetric dimer drifts in the direction of the force along the positive x axis, as expected. In contrast, Fig. 3.3(c) illustrates the case of a *symmetry-broken* dimer in the absence of any applied external force. The *symmetry broken* dimer exhibits net motion in the negative x direction, transport arising from the broken damping symmetry. Lastly, in Fig. 3.3(d), we examine the case where both damping asymmetry and an external force are present. The intrinsic asymmetry drives the dimer in the negative x direction, while the external force tends to push

it in the positive x direction. For the chosen parameters, the damping asymmetry-induced transport dominates, resulting in net motion against the direction of the applied force, thus performing mechanical work. This behavior demonstrates that the system is able to harness thermal fluctuations from the heat bath and convert them into directed motion, effectively storing energy as mechanical (potential) energy by climbing an energy gradient (potential energy landscape due to external force) as shown in schematic in Fig. 3.1(b). In this way, equilibrium thermal noise, when coupled with spatial damping asymmetry, can be rectified to perform useful work in the presence of an external force. The heat bath, maintained at a constant temperature, thereby enables an inchworm-like symmetry-broken dimer to ascend a potential ramp, converting thermal energy into potential energy.

The parameters in the system can control the propensity of motion. We examine how the average CM Velocity depends on individual model parameters at $F = 1.5$. The interplay between these factors determines how effectively the system converts thermal energy into mechanical work.

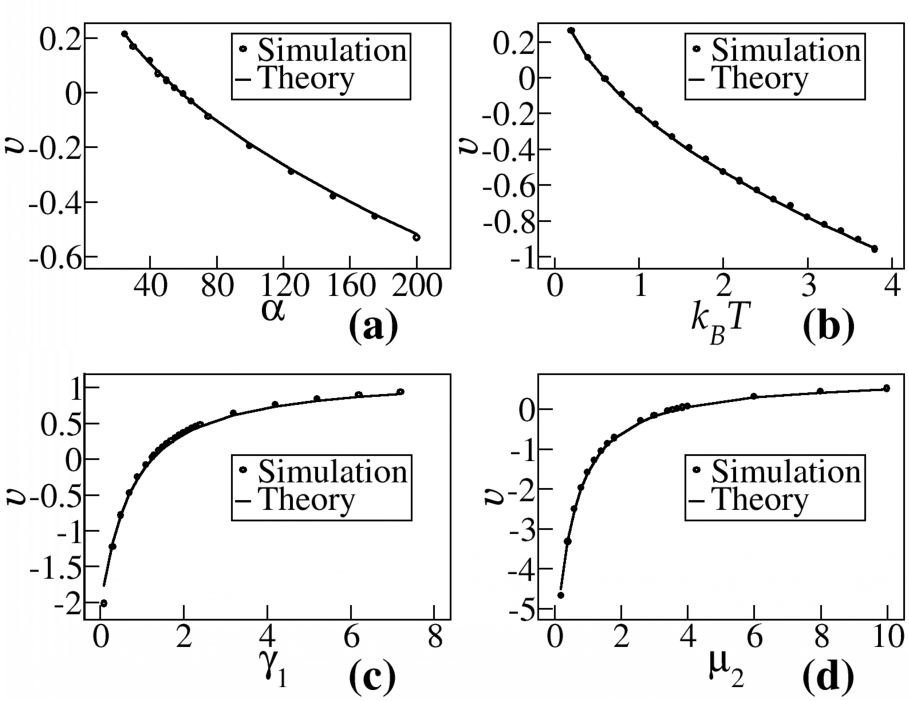

Figure 3.4: Variation of the average velocity of CM shown against system parameters with $F = 1.5$, keeping rest of the parameters fixed as in table 5.1.

Figure 3.4(a) shows how the average CM velocity depends on the interaction parameter α, in the presence of a constant external force F. The external force tends to drive the system in the positive x-direction. However, as α increases, the interaction potential becomes steeper, and the strength of the symmetry-breaking internal force grows. This eventually counteracts the effect of the external force, reducing the net CM velocity to zero at $\alpha = 58.6$. Beyond this point, the system moves in the negative x-direction, indicating that internal symmetry-breaking dominates the external drive. While this reversal is clearly visible in Fig. 3.4(a), it's important to note that α cannot be increased arbitrarily, as excessively steep potentials violate the assumption of slow, overdamped dynamics. To monitor this, we use the efficiency η; values of $\eta \approx 1$ signal a breakdown of the overdamped approximation.

Fig. 3.4(b) illustrates the dependence of the average center-of-mass velocity on thermal energy k_BT. At $k_BT = 0.586$, the velocity drops to zero, indicating a balance between the external force and the symmetry-induced ratcheting effect. Beyond this point, increasing thermal fluctuations enhance the ratcheting mechanism, leading to net motion opposite to the direction of the applied force.

Figures 3.4(c) and (d) show the variation of centre of mass velocity with damping parameters. The divergence of the average center-of-mass velocity as the parameters γ_i and μ_i approach smaller values. This divergence arises from the growing differences $|\gamma_1 - \gamma_2|$ and $|\mu_1 - \mu_2|$, which enhance asymmetry in the system. As these differences increase, the relevant timescales shorten, potentially pushing the system beyond the regime of slow, overdamped dynamics (for fixed time step of simulation). This can result in a breakdown of the model's validity, particularly if the system approaches or exceeds the efficiency bound (analogous to the Carnot limit) imposed in our analysis.

We next understand how the efficiency of ratcheting depends on system parameters. The linear dependence of the average center-of-mass velocity on the external force, as shown in Fig. 3.5(a) serves as another confirmation for our linear regime modeling. Moreover, we identify the *stall force* as approximately $F \approx 1.96$. This force marks the transition point where the asymmetry-induced spontaneous motion is exactly counterbalanced by the applied force, resulting in no net transport. Furthermore, Fig. 3.5(b) shows that the efficiency of the system in converting thermal energy into mechanical work, displays a non-monotonic behavior with respect to the

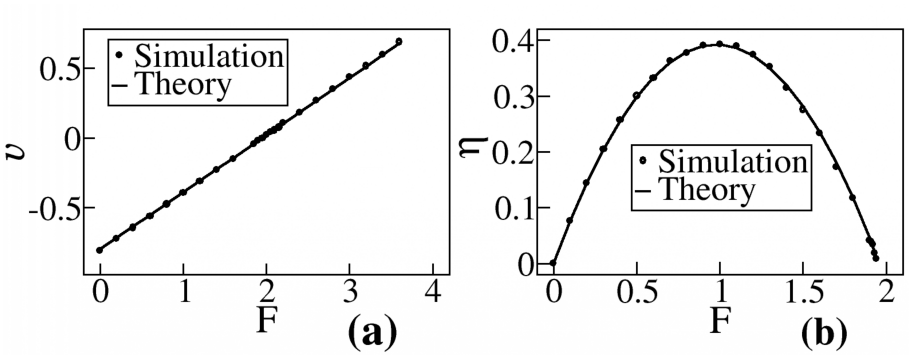

Figure 3.5: Variation of the average center-of-mass velocity and ratcheting efficiency as functions of the applied external force. The results illustrate the linear response behavior and highlight the existence of an optimal force that maximizes efficiency.

applied force. Initially, as the force increases, efficiency improves, reaching a peak of around 40% around $F \approx 1.0$. Beyond this point, further increases in the force reduce the efficiency Thus, average velocity of the center of mass and the efficiency of ratcheting against an external force are sensitive to the system parameters.

Finally, we examine the dependency of efficiency of ratcheting depends on system parameters. These include the degree of damping asymmetry, the inter-particle interaction potential, and thermal energy. The interplay among these factors determines the extent to which the system can rectify equilibrium fluctuations and convert thermal energy into useful mechanical work.

Fig. 3.6(a) shows excellent matching of simulation generated and analytically obtained values of efficiency for the model. At lower thermal energies, the system shows limited efficiency, as the thermal fluctuations are insufficient to drive the ratchet mechanism effectively. However, as thermal energy increases, the efficiency rises, reflecting the increasing contribution of thermal fluctuations to the directed motion. With further increase in thermal energy, efficiency starts decreasing. This non-monotonic behavior underscores the delicate interplay between thermal energy and the system's efficiency, with an optimal range of thermal energy that maximizes the ratcheting efficiency. Understanding this relationship is crucial for designing systems that leverage thermal fluctuations for optimal energy extraction or directed transport.

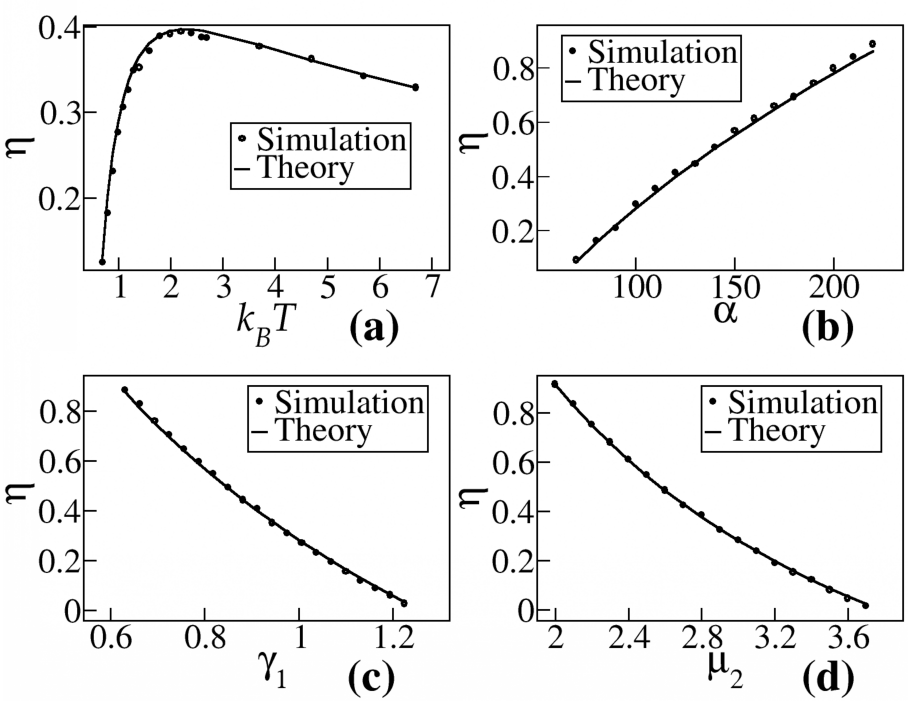

Figure 3.6: Dependence of efficiency on thermal energy, spring parameter, and damping coefficient of the system for $F = 1.5$.

The efficiency also increases with the interaction(spring) parameter α. As evident from Fig. 3.6(b), η and would eventually exceed unity at sufficiently large α. However, such high values of α indicate a breakdown of the overdamped theory, so we restrict our analysis to much smaller values. Notably, α represents the inverse square of a characteristic time scale for a unit mass. A very large α corresponds to an extremely short time scale, which contradicts the assumption of slow overdamped dynamics. Therefore, one cannot arbitrarily increase α without violating the theoretical framework.

Furthermore, Fig.'s 3.6(c) and (d) illustrate how efficiency varies with the damping parameters. The differences in γ_i and μ_i serve as indicators of broken symmetry. As these differences increase or decrease, the efficiency correspondingly rises or falls, emphasizing the crucial role of symmetry breaking in enhancing transport efficiency.

3.3 Conclusion

In this chapter, we have investigated the dynamics and energetics of a symmetry-broken dimer (inchworm-structured ratchet system), capable of extracting useful work from thermal fluctuations in a heat bath, in the presence of an opposing (external) force. Our analysis, based on an overdamped Langevin framework, focuses on slow dynamical regimes where notions of thermodynamic quantities such as temperature remain meaningful despite the non-equilibrium setting. Within this framework, we have demonstrated that a significant component of the energy driving the ratchet arises purely from fluctuations of the bath, a feature absent in conventional flashing or rocking ratchet models, where efficiency is primarily tied to external driving forces. Conventional ratchet models typically treat particles as point-like, attributing all symmetry-breaking to external potentials. The other key insight from our study is that the structure of the moving object itself, not just the landscape it moves through, can serve as a source of asymmetry and energy conversion.

4

Interacting Symmetry-Broken Dimers in Higher Dimensional Space

In the second chapter, we laid the groundwork for understanding how equilibrium fluctuations can drive directed transport in a structured, symmetry-broken dimer confined to one dimension. In the third chapter, we introduced a constant external load opposing the dimer's motion and demonstrated how this symmetry-broken dimer extracts energy from the heat bath (which is maintained at constant temperature by the aid of a much bigger reservoir) to move against this load.

In this chapter, we extend the study of the symmetry-broken dimer operating in the absence of external force from one dimension to higher dimensions, focusing exclusively on pure equilibrium conditions. Unlike in one dimension, where rotation is forbidden, the presence of rotational degree of freedom in higher dimensions can average out axial asymmetry and potentially disrupt the directional transport observed in one dimension. A central question we explore in this chapter is: *Whether rectified transport can still emerge (in pure equilibrium conditions) under some conditions without an external non-equilibrium source or drive?*

To explore such a possibility, we perform numerical simulations of interacting symmetry-broken dimers undergoing Brownian motion in the presence of coordinate-dependent damping. We look at many-body effects of these objects in two-dimensional space. This chapter is adapted from Ref. [58].

4.1 Many Body Dimer Model

We consider a system of N interacting, symmetry-broken dimers confined within a two-dimensional circular domain in contact with an isotropic, homogeneous thermal bath at constant temperature T. Each dimer consists of two bonded monomers (or constituents) that differ in their dissipative properties (as seen in Chapter 2), leading to internal asymmetry through coordinate-dependent damping, which depends on monomer separation. In the context of Fig. 4.1, the two bonded monomers correspond to a silver and a red constituent (interacting by a harmonic potential in figure) that together form a dimer. This damping asymmetry between both constituents (red and silver) gave rise to a persistent directional bias in one dimension, as discussed in previous chapters.

The two monomers in each dimer attract one another, except at very short distances, where excluded volume interactions generate repulsion. They are connected by a stiff but flexible harmonic bond that maintains the internal separation near an equilibrium length while still allowing fluctuations driven by thermal noise.

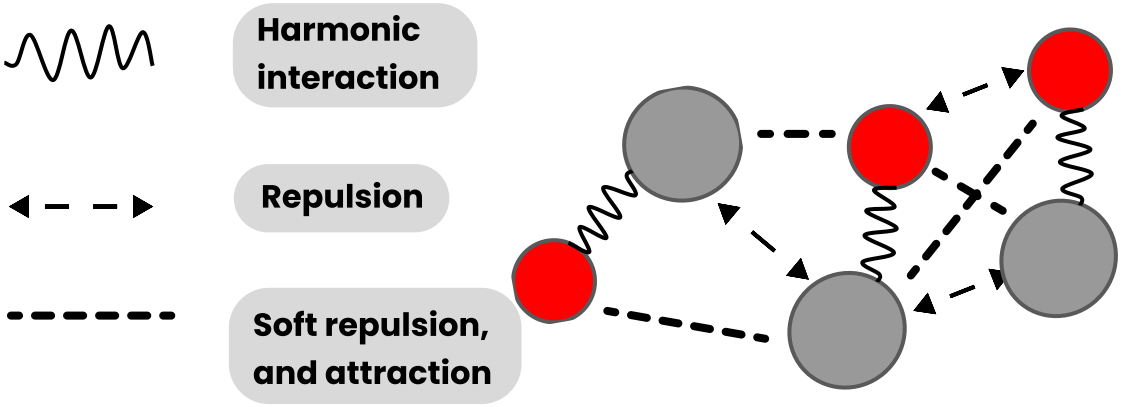

Figure 4.1: Schematic of many dimer model.

Interactions between different dimers are designed to suppress free rotation and enable structure formation. In this setup, the similar constituents of different dimers i.e., those with the same form of damping repel each other within a defined proximity. In regard to Fig. 4.1, it means that the red constituents of different dimers (as well as the silver constituents of different dimers) share the same damping profile and thus repel each other. Conversely, dissimilar constituents of different dimers attract

each other within a certain distance, while the excluded volume interaction ensures that they do not overlap at small distances. Thus, in the context of Fig. 4.1, these interactions occur between the red and silver constituents of different dimers. This choice of dipolar interaction is made to restrict the rotational degree of freedom of the system; other interaction forms could similarly achieve this effect. To ensure that the system remains spatially bounded and the emergent structures can be clearly visualized, all particles are confined within a circular domain of fixed radius. The confinement helps prevent diffusion out of view and makes the observation of collective motion more tractable.

4.1.1 Coordinate Definitions and Notation

Let $i, j \in \{1, 2, \ldots, N\}$ denote dimer indices. Coordinates $\mathbf{r}_1^i$ and $\mathbf{r}_2^i$ are positions of constituent 1 and constituent 2 of the i-th dimer, where the origin of coordinates is at the center of the circular boundary. We define the separation vector as $\mathbf{r}^i = \mathbf{r}_1^i - \mathbf{r}_2^i$, and denote magnitudes as $r^i = |\mathbf{r}^i|$, $r_1^i = |\mathbf{r}_1^i|$ and $r_2^i = |\mathbf{r}_2^i|$. Moreover, $m/m' \in \{1, 2\}$ correspond to constituent identification index. Thus, $r_m^i = |\mathbf{r}_m^i|$.

To define inter-dimer separations between same (like) constituent ($m = m\prime$) of different dimers ($i \neq j$), we define $\mathbf{r}_{mm}^{ij} = \mathbf{r}_m^i - \mathbf{r}_m^j$ and $r_{mm}^{ij} = |\mathbf{r}_{mm}^{ij}|$ is the magnitude of separation between same constituent (same index m) of different dimers (different indices i and j).

We define inter-dimer separations between different (unlike) constituent ($m \neq m\prime$) of different dimers ($i \neq j$), $\mathbf{r}_{mm'}^{ij} = \mathbf{r}_m^i - \mathbf{r}_{m'}^j$ and $r_{mm'}^{ij} = |\mathbf{r}_{mm'}^{ij}|$ is the magnitude of separation between unlike constituents of different dimers.

4.1.2 Interaction Potential

The dimers interact by the following interactions:

Intra-Dimer Bonding Potential

The interaction potential V_h between primary constituents of a dimer (constituent 1 and constituent 2 of i^{th} dimer) is harmonic in simulations:

$$V_h(r^i) = \frac{\alpha}{2}(r^i - r_{\min})^2,$$

where α is the fixed bond stiffness/spring constant and $r_{\min}$ is the equilibrium intra-dimer bond length.

Inter-Dimer Interaction Potentials

Like-Monomer Repulsion: The potential $V_l(|\mathbf{r}_m^i - \mathbf{r}_m^j|)$ is harmonic repulsive in nature maintaining interaction between similar (like) constituents of different dimer $(i \neq j)$ has the following structure in our simulations.

$$V_l(r_{mm}^{ij}) = \begin{cases} \frac{1}{2}\kappa_l(r_{mm}^{ij} - r_l)^2 & r_{mm}^{ij} < r_l \\ 0 & r_{mm}^{ij} \geq r_l \end{cases}$$

r_l is the fixed distance below which the same constituents of different dimers start feeling repulsive force and κ_l measures strength of repulsion.

Unlike-Monomer Interaction: The interaction between dissimilar constituents $(m \neq m')$ of different dimers $(i \neq j)$ is modeled using a piecewise potential $V_u(|\mathbf{r}_m^i - \mathbf{r}_{m'}^j|)$. This combines a truncated and shifted *Lennard-Jones* potential for attraction and a harmonic potential for short-range repulsion. The construction ensures that both the potential and the force vanish smoothly at the cutoff r_c and above it, enabling efficient integration without requiring very small time steps, even for large well depths.

$$V_u(r_{mm'}^{ij}) = \begin{cases} (\tilde{\Phi}_u - V_{LJ}^*) + F_{LJ}^* \times (r_{mm'}^{ij} - r_c), & \text{if } r_{mm'}^{ij} \leq r' \\ (V_{LJ} - V_{LJ}^*) + F_{LJ}^* \times (r_{mm'}^{ij} - r_c), & \text{if } r' < r_{mm'}^{ij} \leq r_c \\ 0 & \text{if } r_{mm'}^{ij} > r_c \end{cases}$$

with the *Lennard Jones (LJ)* form :

$$V_{LJ}(r_{mm'}^{ij}) = 4\epsilon \left[\left(\frac{\sigma}{r_{mm'}^{ij}} \right)^{12} - \left(\frac{\sigma}{r_{mm'}^{ij}} \right)^{6} \right],$$

where ϵ sets the interaction strength, σ is the characteristic length scale and $r' = 2^{\frac{1}{6}}\sigma$ corresponds to the potential minimum of LJ potential. The constants $V_{LJ}^* = V_{LJ}(r_c)$

and $F^*_{LJ} = -\left.\frac{dV_{LJ}(r^{ij}_{mm'})}{dr^{ij}_{mm'}}\right|_{r=r_c}$ are the values of standard Lennard-Jones potential and force magnitude (radial derivative of potential) at cutoff distance $r_c = 4\sigma$.

The shifted harmonic repulsion is given by:

$$\tilde{\Phi}_u(r^{ij}_{mm'}) = \frac{k_u}{2}(r^{ij}_{mm'} - r')^2 - \epsilon,$$

where $k_u$is the repulsion strength.

Confinement Potential

Particles are confined within a circular domain of radius R via a harmonic repulsive boundary potential $V_b(r^i_m)$:

$$V_b(r^i_m) = \begin{cases} 0 & r^i_m < R \\ \frac{1}{2}k_{bo}(r^i_m - R)^2 & r^i_m \geq R \end{cases}$$

k_{bo} sets the repulsion strength, and R is the confinement radius. The potential is zero inside the domain and increases quadratically outside to gently repel particles back into the domain.

4.1.3 Thermal Noise Terms

The noise term $\boldsymbol{\eta}^i_m(t)$ represent independent vector Gaussian white noise acting on m^{th}constituent of the i^{th} dimer, expressed in Cartesian components as:

$$\boldsymbol{\eta}^i_m(t) = \eta^i_{mx}(t)\,\hat{x} + \eta^i_{my}(t)\,\hat{y}, \quad \text{for } m = 1, 2.$$

Each component $\eta^i_{m\mathcal{S}}(t)$ (with $\mathcal{S} \in \{x, y\}$ is a spatial component book-keeping variable) represents a Continuous, Markov, independent, zero-mean Gaussian white noise process with unit variance, delta-correlated in time and mutually uncorrelated across dimer indices, constituent labels, and spatial components:

$$\langle \eta^i_{m\mathcal{S}}(t) \rangle = 0,$$

$$\langle \eta^i_{m\mathcal{S}}(t)\eta^j_{m'\mathcal{S}'}(t') \rangle = \delta_{ij}\,\delta_{mm'}\,\delta_{\mathcal{S}\mathcal{S}'}\,\delta(t - t').$$

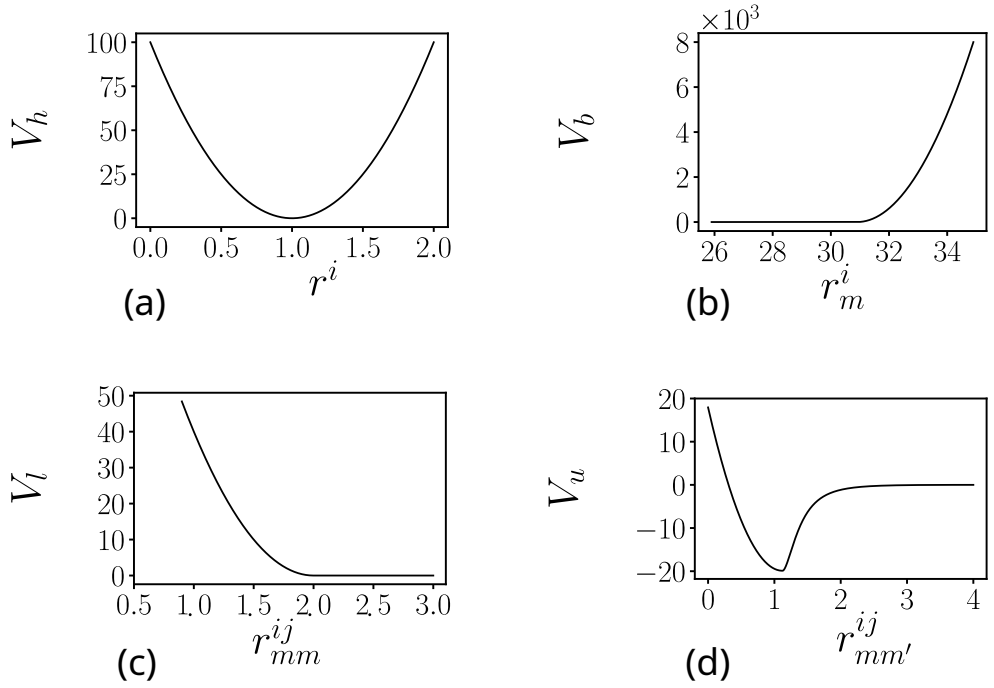

Figure 4.2: Representative profile of potentials with typical parameters used in simulation: (a) Intra-dimer harmonic potential: $\alpha = 200$, $r_{min} = 1$. (b) Confining potential: $k_{bo} = 1000$, $R = 31$. (c) Similar constituent (like monomer) interaction potential: $\kappa_l = 80$, $r_l = 2$. (d) Dissimilar constituent (unlike monomer) interaction potential: $k_u = 60$, $\epsilon = 20$, $\sigma = 1$.

4.1.4 Damping Function

Each m^{th} monomer of i^{th} dimer experiences damping dependent $\Gamma_m(r^i)$, which depends on the internal dimer coordinate r^i:

$$\Gamma_m(r^i) = \frac{a_m}{1 + \exp[-\lambda_m(r^i - r_{\min})]} + b_m,$$

where a_m, b_m, and λ_m are tunable parameters controlling the amplitude, baseline, and steepness of the damping profile. r_{min} is the equilibrium separation between constituents of the dimer. The damping symmetry of the dimer is broken by choosing unequal value of one (or more) tunable parameter(s) for either monomer of the dimer.

It is important to note that the damping in this model is only function of the con-

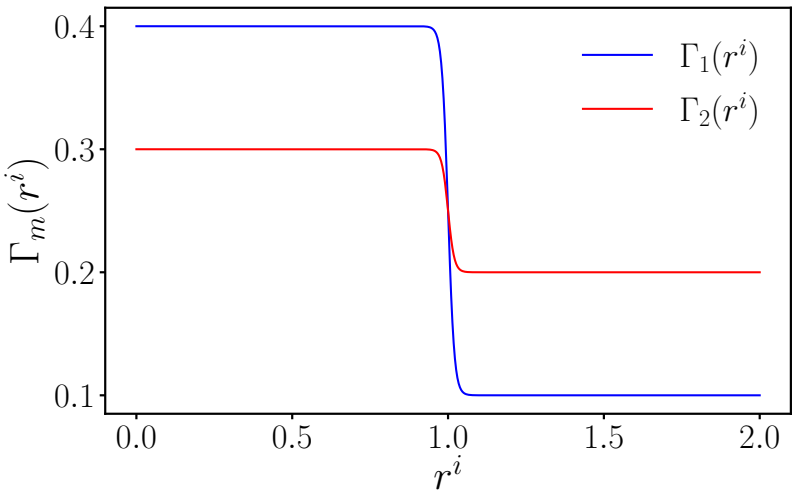

Figure 4.3: Damping profile for typical parameters used in simulation : $r_{min} = 1$, $a_1 = -0.3$, $b_1 = 0.4$ and $\lambda_1 = 100$; and $a_2 = -0.1$, $b_2 = 0.3$ and $\lambda_2 = 100$ (unless stated otherwise).

figuration (or separation) coordinate r^i of an individual dimer and does not depend on the interparticle separation of different dimers. Additionally, the circular confinement is treated as a purely geometric boundary without introducing hydrodynamic interactions or coordinate-dependent effects. This is a simplified approach, however, enough to reveal intended results in the present context. Typical parameters used in the simulation which amount to broken symmetry dimer is shown in Fig. 4.3.

4.1.5 Stochastic Equations of Motion

The dynamics for monomer $m/m' \in \{1, 2\}$ of the i^{th} dimer is governed by the following overdamped Langevin equations:

$$\frac{d\mathbf{r}_m^i}{dt} = -\frac{1}{\Gamma_m(r^i)} \nabla_{\mathbf{r}_m^i} \mathcal{V}_m^i + \sqrt{\frac{2k_B T}{\Gamma_m(r^i)}}\, \boldsymbol{\eta}_m^i(t).$$

where $\mathcal{V}_m^i$ include all potentials acting on m^{th} monomer of the i^{th} dimer. These include the contributions from intra-dimer, inter-dimer and confining potential acting

on the m^{th} constituent of i^{th} dimer.

$$\mathcal{V}_m^i = -\nabla_{\mathbf{r}_m^i}\left[V_h(r^i) + V_b(r_m^i)\right] - \nabla_{\mathbf{r}_m^i}\sum_{\substack{j\\ j\neq i}}\left[V_l\left(r_{mm}^{ij}\right) + \sum_{\substack{m'=1\\ m'\neq m}}^{2} V_u\left(r_{mm'}^{ij}\right)\right]$$

Explicitly, these have the following form:

$$\mathcal{V}_1^i = -\nabla_{\mathbf{r}_1^i}[V_h(r^i) + V_b(r_1^i)] - \nabla_{\mathbf{r}_1^i}\sum_{\substack{j\\ i\neq j}}\left[V_l(|\mathbf{r}_1^i - \mathbf{r}_1^j|) + V_u(|\mathbf{r}_1^i - \mathbf{r}_2^j|)\right]$$

$$\mathcal{V}_2^i = -\nabla_{\mathbf{r}_2^i}[V_h(r^i) + V_b(r_2^i)] - \nabla_{\mathbf{r}_2^i}\sum_{\substack{j\\ i\neq j}}\left[V_l(|\mathbf{r}_2^i - \mathbf{r}_2^j|) + V_u(|\mathbf{r}_2^i - \mathbf{r}_1^j|)\right]$$

4.2 Simulation Methodology

The dynamics in position coordinate representation is transformed to $4N$ coupled Brownian equations in cartesian system of coordinates for our simulation. Dimers are initialized in random configuration in a two-dimensional circular confinement and Euler-Maruyama algorithm (see Appendix C) is implemented to simulate these $4N$ coupled Brownian dynamics equations. All simulations use a new random seed each time step. The following updating scheme is used in simulations:

(1) Assign random positions to dimers at beginning of the simulation.

(2) Corresponding to the positions, calculate the respective forces.

(3) Update the position of each dimer using the forces calculated in step (2) by employing explicit Euler-Maruyama discretization scheme.

(4) Go back to step (2) and repeat.

4.3 Simulation Details

All simulations are performed in the overdamped regime using Brownian dynamics, where the thermal energy k_BT and the equilibrium bond length r_{min} are set to unity and serve as the fundamental reference scales for energy and length, respectively. The parameters expressed in simulation units can be rescaled using appropriate reference values similar to ones discussed in previous chapters. Tables 4.1, 4.2, 4.3 and 4.4 display the parameters used in the simulation.

Symbol	Length Scale	Value
$r_{\min}$	Equilibrium bond length	1
r_l	Interaction range (like monomers)	1.8 to 3 (varied)
σ	LJ interaction width (unlike monomers)	1 to 2 (varied)
r_c	Cutoff distance for LJ-like potential	4σ
R	Circular arena radius	31

Table 4.1: Length scales and cutoff distances used in the simulations.

Symbol	Interaction	Value
α	Intra-dimer bond stiffness	200
κ_l	Like-monomer repulsion strength	80
ϵ	Unlike-monomer attraction strength	20
k_u	Harmonic repulsion stiffness (unlike monomers)	60
k_{bo}	Boundary wall stiffness	1000

Table 4.2: Interaction strength parameters used in the simulation.

Symbol	Parameter	Value
a_1	Sigmoidal damping (monomer 1)	-0.3
b_1	Sigmoidal offset (monomer 1)	0.4
λ_1	Damping steepness (monomer 1)	100
a_2	Sigmoidal damping (monomer 2)	-0.1
b_2	Sigmoidal offset (monomer 2)	0.3
λ_2	Damping steepness (monomer 2)	100

Table 4.3: Parameters for sigmoidal coordinate-dependent damping profiles.

Symbol	Parameter	Value
k_BT	Thermal energy	1
N	Number of dimers	30
Δt	Time step	10^{-5} to 10^{-4} (varied)

Table 4.4: Other simulation parameters.

4.4 Results

Emergent Collective Motion in Interacting Dimer Systems

While a symmetry-broken dimer exhibits directed motion in one dimension [1], this behavior is generally lost in higher dimensions due to its ability to rotate freely. In two dimensions, the directional bias is effectively averaged out over time, resulting in no sustained net motion for an isolated dimer.

However, when multiple such dimers interact, new forms of organized behavior can emerge. The inter-dimer forces and geometric constraints introduced by interactions can suppress rotational freedom and lead to the spontaneous formation of structured assemblies. Within these structures, the directional biases of individual symmetry broken dimers no longer cancel out. Instead, they become aligned or coordinated, allowing the system to regain and even amplify coherent motion at the collective level.

In the following subsections, we present a range of structures that emerge under different interaction regimes, and we examine how collective motion arises from the interplay of broken symmetry, thermal fluctuations, and confinement within these formations. In particular, by varying σ and r_l, and adjusting the time step accordingly while keeping other parameters fixed (shown in table's 4.1, 4.2, 4.3, 4.4), we observe how these structural and dynamical patterns emerge. Simulations are run for each set of interaction parameters under both symmetry-broken ($\Gamma_1(r^i) \neq \Gamma_2(r^i)$) and symmetry-unbroken ($\Gamma_1(r^i) \equiv \Gamma_2(r^i)$) conditions and can be found in the Journal website and in the Youtube links attached in caption of figures.

4.4.1 Chain formation: Emergent flocking

In a class of simulations characterized by moderately long repulsive interactions range between similar constituents and controlled attraction range between dissimilar ones ($\sigma = 1.5$, $r_l = 3$), we observe the spontaneous formation of linear aggregates of dimer *chains*. These structures display persistent, coherent translation across the system, evocative of *flocking behavior* commonly attributed to self-propelled or ac-

[1] For completeness, we analyze the behavior of a single dimer confined to one dimension under sigmoidal damping, which is summarized in the Appendix E. The qualitative results in one dimension remain the same as discussed in previous chapters.

tive matter systems.

What makes these chains particularly remarkable is that the motion emerges in a system entirely governed by thermal noise and conservative interactions, with no external drive or alignment rule. The key lies in the broken symmetry of damping: due to coordinate-dependent damping(friction) experienced by the constituents, the stochastic response to isotropic thermal noise becomes biased along the internal axis of the dimer. When several such dimers come together in a mutually aligned configuration, their individual tendencies to move along their axes align, resulting in coherent translational motion of the entire chain.

The constituent dimers effectively freeze into an orientation-locked state, giving rise to motion as a single object. The chain behaves like an extended nonrigid filament moving through the heat bath, not due to any imposed force but because of a subtle re-weighting of stochastic responses encoded in the Itô equilibrium distribution. This phenomenon exemplifies equilibrium-induced flocking, made possible by the spontaneous filtering of Brownian noise due to coordinate-dependent damping.

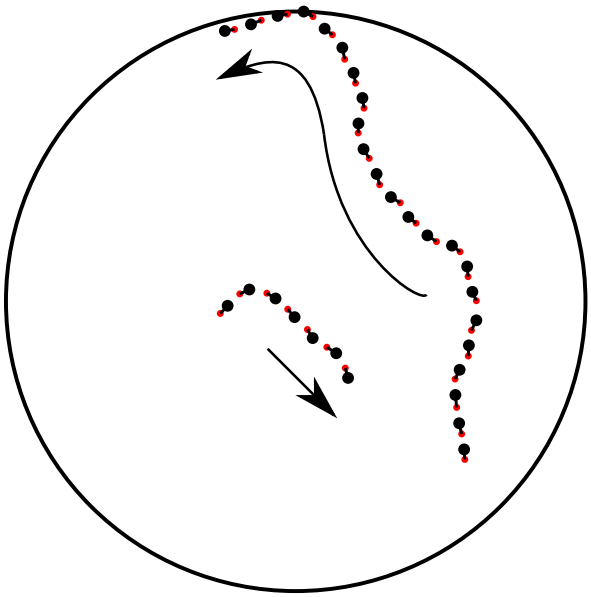

Figure 4.4: Snapshot of Flocks, where the arrow denotes the instantaneous direction of motion of the center of mass. Parameters: ($\sigma = 1.5$, $r_l = 3$ and $\Delta t = 10^{-4}$). See video here.

4.4.2 Swarming: Ferromagnetic-Like Alignment

In a different parameter regime ($\sigma = 2$, $r_l = 3$), particularly at longer times and with adjusted interaction ranges, the system evolves into *dynamic swarming clusters* that move coherently as a unit. These swarms remain structurally fluid, stochastically reconfiguring at the boundary of the structure they form, while maintaining a stable global direction of motion. The resulting collective state, where assembly of dimers move in near-unison, is analogous to *ferromagnetic ordering* in spin systems but realized here through alignment of velocity vectors in physical space rather than spins.

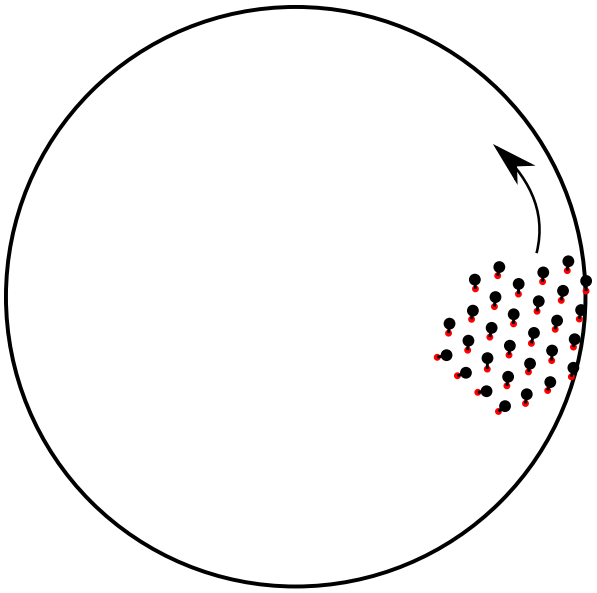

Figure 4.5: Snapshot of Ferromagnetic like ordered dimers or Swarms, where arrow denotes the instantaneous direction of motion of center of mass. Parameter: ($\sigma = 2$, $r_l = 3$) and $\Delta t = 10^{-5}$. See video here.

The emergent swarming motion (similar to flocking case) stems from two complementary factors: local conservative interactions that promote spatial clustering and partial orientation alignment, and *broken symmetry* in damping, which biases the response of each dimer to stochastic forces along its internal axis. These two ingredients, acting together, give rise to large-scale dynamical coherence in an otherwise passive system.

As a result, the system self-organizes into a traveling band, reminiscent of the collective motion seen in Vicsek-type models [59–61] of active matter, but here, without any explicit alignment rule or external propulsion. This demonstrates that directional consensus can arise naturally in thermal systems, provided that the internal structure of the constituents introduces state-dependent asymmetry in how they interact with the heat bath. These findings show that swarming without activity is not only possible, but a natural consequence of structured response and state-dependent internal asymmetry.

Origin of Rotation in Many Body Clusters

In the next few examples, we observe that a group of dimers self-organizes into compact clusters that rotate coherently around a central axis. The origin of this rotation lies in the *intrinsic directional bias* of each dimer, which arises from the *broken symmetry in its damping profile*. In one dimension, an isolated dimer tends to drift from its low damping end toward its high damping end aided by thermal fluctuations. However, in two dimensions, a freely rotating dimer experiences no net rectification, as its orientation changes over time and the directional bias averages out.

When multiple such dimers come into close proximity, the inter-dimer interactions (non-angular in nature) defined in the model drive them to assemble into configurations. Within these closed-loop structures, each dimer retains its internal drive but is geometrically constrained and unable to translate freely in its preferred direction. Instead, the collective effect of these constrained, biased motions manifests as a *net torque* on the entire cluster.

Crucially, this torque is not imposed externally, it emerges *spontaneously from the coordinated motion of asymmetrically damped particles* fluctuating under thermal noise. The result is a persistent, steady rotation of the entire cluster, driven by equilibrium fluctuations and sustained by internal asymmetry. This phenomenon exemplifies how microscopic directional biases, when coupled with spatial confinement and interactions, can convert random thermal energy into organized, macroscopic motion, even in systems that *obey detailed balance*.

Occasionally, the torque generated by one part of the cluster can counteract with torques from other parts, depending on the spatial arrangement. This can occur

due to asymmetric geometry within the structure or local misalignment of dimer orientations. In some cases, the entire cluster may also be structurally unstable, undergoing shape changes over time. Such reconfigurations can alter or interrupt the rotation.

4.4.3 Crystal-Like Structures with Coherent Rotation

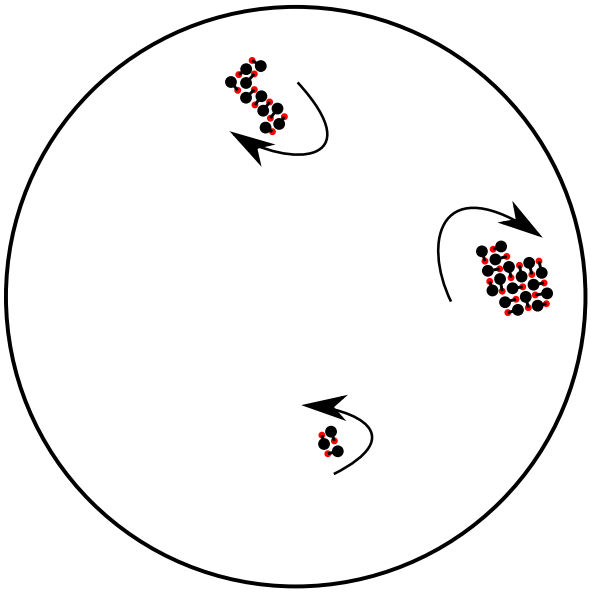

Figure 4.6: Snapshot of many-body crystal like structures with coherent rotation. Parameter: $\sigma = 1$, $r_l = 1.8$ and $\Delta t = 10^{-5}$. See video here.

In a slightly different parameter regime of small repulsion and attraction range $\sigma = 1$, $r_l = 1.8$, the system exhibits the spontaneous formation of *crystal-like* structures compact, ordered assemblies of dimers stabilized by conservative inter-dimer interactions. While these clusters resemble static solids in structure, they display a remarkable dynamical feature: persistent, coherent rotation around their collective center of mass. In Fig 4.6, the crystal like structures with the direction of coherent rotation are shown.

These crystalline clusters are dynamically stable yet structurally soft. Their internal ordering remains intact over time, though individual dimers may fluctuate slightly or form transient defects. Still, the clusters often complete many revolutions with

minimal distortion. At small times, dimers form chiral symmetry-broken tri-dimer and quad-dimer which then combine and form a large chiral-symmetry broken rectangular lattice like structures which rotate depending upon the broken symmetry following the direction of motion of the individual dimers.

4.4.4 Rotating Triangular Clusters: Chiral Asymmetry from Damping Asymmetry

In the parameter regime with small repulsion range $r_l = 2.2$ between similar constituents of different dimers and higher attractive range $\sigma = 2$ between different constituent of different dimers, *rotating triangular cluster*, typically composed of three (or more) dimers arranged in a compact, loop-like configuration emerges. These clusters rotate coherently around their collective center of mass.

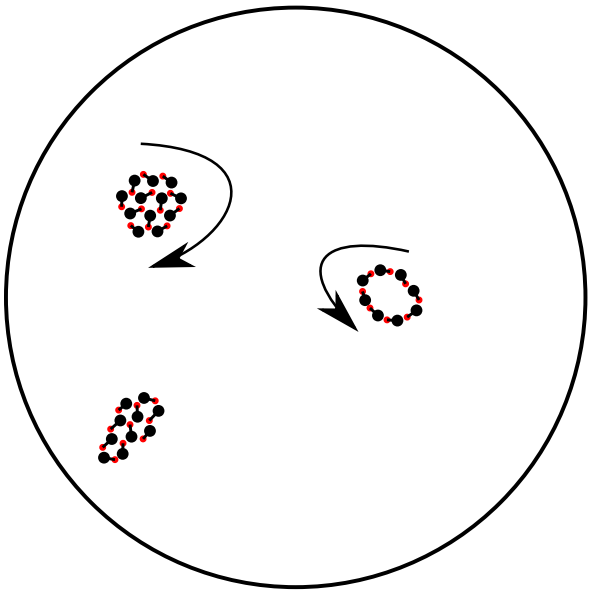

Figure 4.7: Snapshot of triangular patterned rotators. Parameter : $\sigma = 2$, $r_l = 2.2$ and $\Delta t = 10^{-4}$. See video here.

This arrangement of constrained, directionally biased dimers in a two-dimensional domain generates a net torque on the entire structure, converting stochastic thermal fluctuations into sustained rotational motion even without any external force. The

overall effect is that the cluster as a whole begins to spin steadily. As stated above in some configurations, the local torques produced by individual dimers can partially oppose each other, reducing or even temporarily cancelling the net rotation. This is what is happening in one of the structure shown in Fig. 4.7. The direction of rotation is not predetermined, rather, it is chosen stochastically due to the structure formed and chirality encoded in the damping asymmetry of the individual dimers during self-assembly, demonstrating a thermal fluctuation-driven emergence of macroscopic chirality from built-in damping asymmetry.

Phase plot of Emergent structures discussed so far

We now present snapshots of the emergent structural phases exhibiting net transport as a consequence of broken damping symmetry, as discussed above. Since these phases are inherently dynamic, corresponding movies comparing symmetry broken with symmetry unbroken structures, illustrating their time evolution are provided in the captions of Fig. 4.8. All the sub-figures in Fig. 4.8 comprise of parts, where the figure in the circle gives a snapshot of the dimer configurations, other vector-plots show velocity of these structures on average over a given time interval.

The phase shown in Fig. 4.8(a) corresponds to the flocking behavior illustrated in Fig. 4.4. The translation motion of CM of structure II over some time interval is shown where the direction of motion is represented by arrows. Linear queued chains of dimers formed in this regime as shown in Fig. 4.8(a). Fig. 4.8(b) corresponds to swarming parameter regime illustrated in Fig. 4.5. Initially small cyclic chains of associated tri-dimer and quad-dimer are formed. The intermediate structures formed by the association of the three and four dimers when exist in a closed loop always rotate in a particular direction dictated by the direction of motion of individual dimers. At large times, many-body interactions in this parameter regime leads to parallel aligned dimers akin to ferromagnetic order. This eventually forms a single cluster that swarms through on the confined plane. This is also clear by seeing the phase plot of its CM.

In Fig. 4.8(c) and Fig. 4.8(d), we display the local time averaged velocity vector of one member of each cluster depicted by arrow with the tail of arrow being fixed at local time averaged position of the member as seen from centre of masses of respective cluster. The average angular velocity of each cluster in 4.8(c) and 4.8(d) is

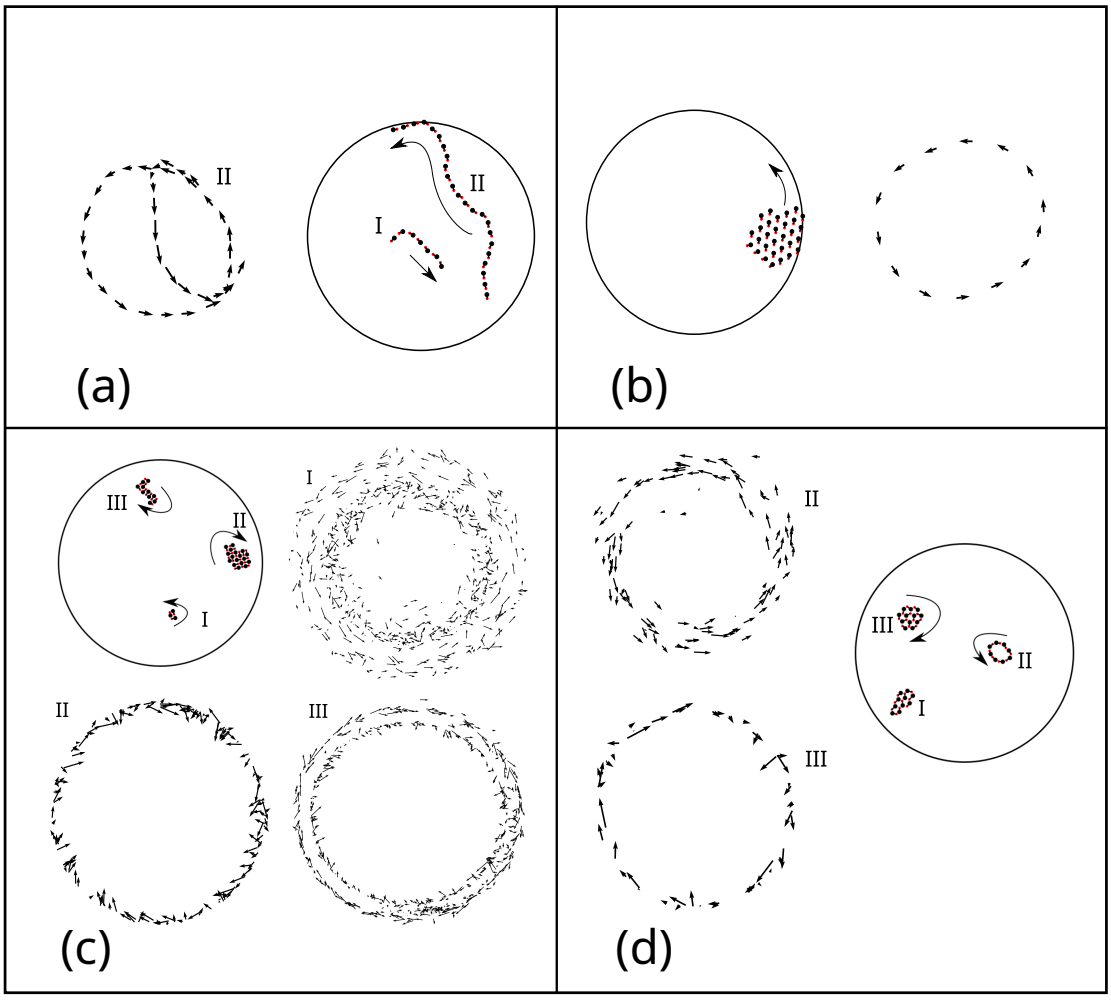

Figure 4.8: Parameters: 4.8(a): $\sigma = 1.5$, $r_l = 3$, and $\Delta t = 10^{-4}$; 4.8(b): $\sigma = 2$, $r_l = 3$, and $\Delta t = 10^{-5}$. The movie of the time evolution of configurations in 4.8(a) and 4.8(b), sped up by ten times and five times respectively, is attached here: 4.8(a) and 4.8(b). Parameters: 4.8(c): $\sigma = 1$, $r_l = 1.8$, and $\Delta t = 10^{-5}$; 4.8(d): $\sigma = 1$, $r_l = 2.2$, and $\Delta t = 10^{-4}$. The movie of the time evolution of structures in 4.8(c) and 4.8(d), sped up by ten times and one and a half times respectively, is attached here: 4.8(c) and 4.8(d).

evaluated by first doing a long-time average over time series of angular velocity of each member of cluster, and then doing an arithmetic average over all the particles constituting a cluster. For obvious reasons, this averaging is done on clusters when no particle entered or left the cluster and number of particles in cluster remain fixed.

Fig. 4.8(c) shows snapshot of results of simulation, which correspond to crystal like rotating structures as shown in Fig. 4.6. Three members form a cluster in I as shown in Fig. 4.8(c), they are less compactly arranged, therefore, fluctuations are more. The cluster II is more dense and thus strength of binding forces is more than thermal fluctuation responsible for displacing dimers considerably from their mean position with respect to centre of mass of cluster. This is responsible for the velocity-plot being less fluctuating. The cluster III undergoes rearrangement in its structure depicted by transition of arrows from one phase line to other and the less fluctuation in velocity plot is obviously attributed to compactness of structure. To see a smoothed velocity plot in Fig. 4.8(c), a local average over velocity and position over time duration equivalent to 200 subsequent recorded positions is performed for cluster II. The local (small time) average angular velocity on calculation came out to be about 0.2 per step of iteration in clockwise direction. We checked that the average angular velocity and qualitative nature of phase plot does not change appreciably by average obtained over time duration corresponding to 100, 150, 250, 300 subsequent recorded positions. Similar scheme is followed for plotting phase plot of other clusters of Fig. 4.8(c). The average angular velocity of clusters I, II and III are found to be 4.6, 0.2 and 0.59 per step of iteration respectively with averaged direction of rotation indicated by arrows in vector plot figure.

In Fig. 4.8(d), we show snapshot of results for simulation, where dimers arrange themselves in triangular lattice like structures that shows uni-directional rotation. This phase corresponds to the structures illustrated in Fig. 4.7. Some Clusters undergoes rearrangement by forming contracting or expanding dimer ring like structure that rotates in one direction, and this is why the velocity plot shows spread, while others forms a more compact structure with uni-directional rotation, thus, the phase plot is less fluctuating. For smoothing out the trajectories of cluster II, a local time averaged velocity and position over time corresponding to subsequent 10 positions

is taken into account. The average angular velocity on calculation came out to be about 2.8 per step of iteration in anti-clockwise direction which does not change appreciably by doing a local overage over 5 or 15 subsequent position instead of 10. Similar scheme is followed for other clusters. The steady state average value of angular velocity of cluster I, II and III in 4.8(d) were found out to be 0, 2.8 and 0.38 per step of iteration.

4.5 Quantitative Measure of Broken Symmetry Induced Collective Transport

Directed transport in many-body systems discussed above arises due to the broken symmetry introduced via coordinate-dependent damping. This is evident from the simulation videos linked in Fig. 4.8 and in earlier figures, which compare symmetry-broken and symmetry-unbroken cases under identical interaction parameters. To move beyond qualitative observation and develop a quantitative understanding of how broken symmetry leads to motion, we define suitable order parameters that characterize the dynamics of different types of collective behavior.

We see that a cluster of symmetry-broken dimers show net transport in the system, whereas a cluster of symmetry-unbroken dimers show random jiggling. Now, the net transport can be translational, or rotational or a mixture of both. Inspired from [62–64], a meaningful order parameter ϕ is defined to quantify a net translation motion along circular boundary for the structures formed in the parameter regimes of Fig.'s 4.4 and 4.5. We define an instantaneous measure $\phi(t_k)$ that measures relative directional alignment and motion of group of dimers with respect to circular boundary of a cluster at time t_k.

$$\phi(t_k) = \frac{1}{N^*}\Big|\sum_{i=1}^{N^*} \frac{\boldsymbol{v}_i(t_k)\cdot\hat{e}_{\theta_i}(t_k)}{|\boldsymbol{v}_i(t_k)|}\Big|,$$

where, N^* denotes total numbers of dimers constituting a cluster at time t_k. Velocity $\boldsymbol{v}_i(t_k)$ is that of the centre of mass of the i-th dimer at time t_k as shown in Fig. 4.9. Angle $\theta_i(t_k)$ is the polar angle made by dimer's centre of mass to x-axis at time t_k, $\hat{e}_{\theta_i}(t_k) = -\sin\theta_i(t_k)\hat{x} + \cos\theta_i(t_k)\hat{y}$ is the instantaneous tangential unit vector corresponding to i-th dimer. $\phi(t_k) = 1$ would imply that all dimers of a cluster are aligned

and moving in same tangential direction along inner circumference of circle at a time instant t_k. A schematic description of the quantity used in $\phi(t_k)$ is shown in Fig. 4.9.

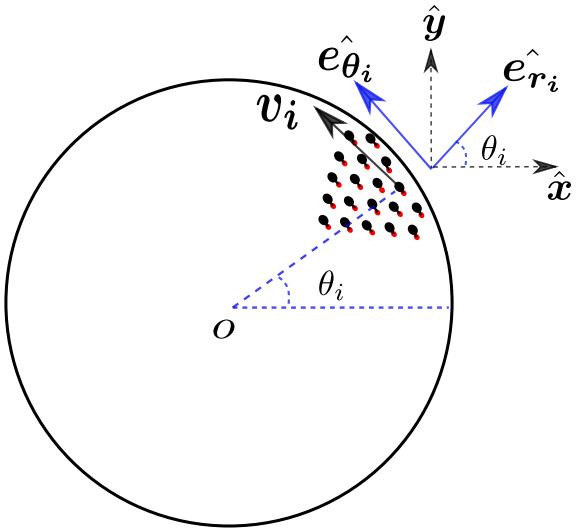

Figure 4.9: Polar angle θ_i, it's corresponding polar unit vectors and velocity $\boldsymbol{v}_i$ shown for the i-th dimer.

To characterize the persistence of collective alignment over time, we generate a time series of the instantaneous alignment measure $\phi(t_k)$, This time series is then divided into several shorter segments, and for each segment, we compute a local time-averaged quantity, denoted ϕ_M, defined as: $\phi_M = \frac{1}{M}\sum_{k_1}^{k_1+M}\phi(t_k)$, where k_1 is the starting time index of the segment, and M is the number of time points within the interval. This averaging helps smooth out short-time fluctuations and captures sustained directional coordination during each segment. The final order parameter ϕ, representing the overall degree of tangential alignment throughout the simulation, is obtained by averaging over all such local segments: $\phi = \langle\phi_M\rangle = \frac{1}{N'}\sum_{j'=1}^{N'}(\phi_M)^{j'}$, where $N^{'}$ is the total number of segments, and $j^{'}$ indexes each segment.

In all cases, to quantify motion using the order parameters ϕ and Ω (will be defined on next page), we vary only the steepness parameter λ_2 (which quantifies damping) of monomer 2, while keeping all other parameters fixed. The amplitude parameters $a_i$and baseline parameters b_i of the damping profiles are chosen to be identical for both monomers of each dimer. The steepness parameter λ_1 of monomer 1 is held constant throughout. When the steepness parameters of both monomers

are equal, the damping profiles become identical, resulting in a symmetry-unbroken case where no net transport is expected. By systematically varying λ_2, we explore the emergence of spontaneous directed motion as symmetry is broken.

Thus, Fig. 4.10 confirms that broken symmetry corresponds to a net collective transport for flocking (Fig. 4.4) and swarming regime (Fig. 4.5. This broken symmetry vanished at $\lambda_1 = \lambda_2 = 100$, for the order parameter ϕ.

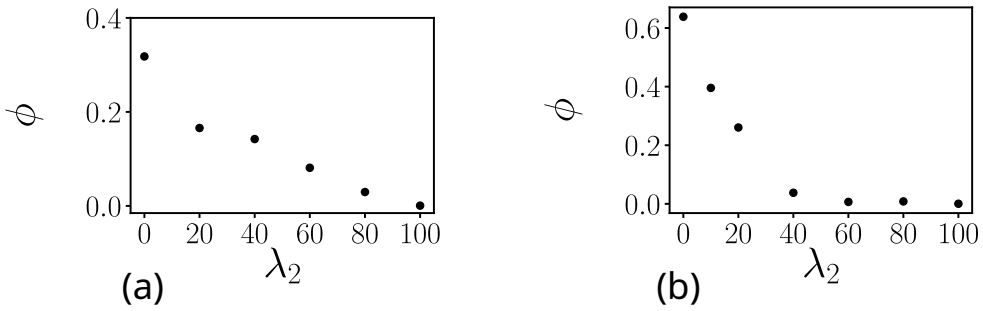

Figure 4.10: Variation of order parameter ϕ with λ_2, keeping other damping parameters fixed: $a_1 = a_2 = -0.3$, $b_1 = b_2 = 0.4$ and $\lambda_1 = 100$. The interaction parameters for Fig. 4.10 (a) and (b) are for the exact same regimes that correspond to kind of motion shown in Fig. 4.4 and 4.5 respectively.

To quantify rotational motion as observed in Fig's. 4.6 and 4.7, we define an order parameter Ω that captures overall local unidirectional rotation of dimer clusters.

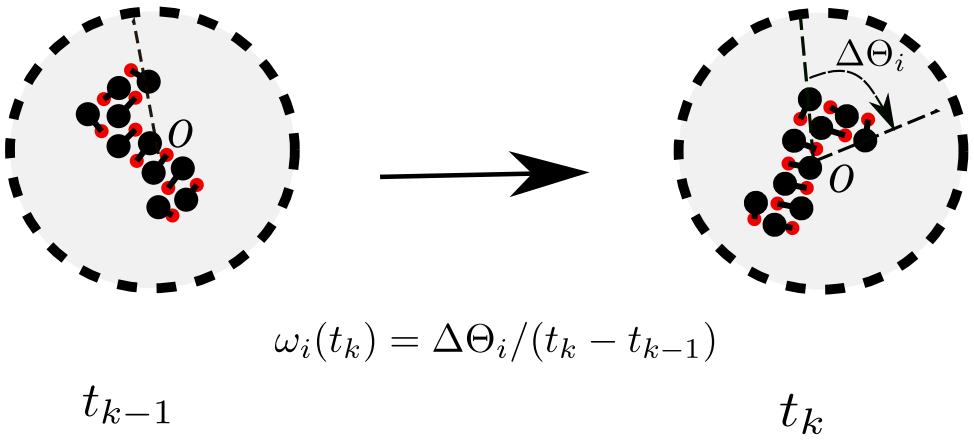

Figure 4.11: Polar angle $\Delta\Theta_i$ swept by i-th dimer of a cluster, with respect to center of mass of cluster O as time elapses from t_{k-1} to t_k. The instantaneous angular velocity of i-th dimer calculated as: $\omega_i(t_k) = \frac{\Delta\Theta_i}{t_k - t_{k-1}}$.

For each dimer i in a stable cluster, the instantaneous angular speed at time t_k is defined as the polar angle $\Delta\Theta_i$ swept by the dimer around the cluster's center of mass between two successive time instants t_{k-1} and t_k: $\omega_i(t_k) = \frac{\Delta\Theta_i}{t_k - t_{k-1}}$ as shown in Fig. 4.11. The time-averaged angular speed for dimer i in the cluster is calculated as: $\bar{\omega}_i = \frac{1}{N'}\left|\sum_{k=k_2}^{k_2+N'} \omega_i(t_k)\right|$, where k_2 marks the start of the averaging window, and N' is the number of time steps in the average. Finally, the order parameter Ω representing the steady rotational motion of the cluster is defined as the arithmetic average of angular speed ω_i over all N'' dimers (members) in the cluster, $\Omega = \langle\bar{\omega}_i\rangle = \frac{1}{N''}\sum_{i=1}^{N''}\bar{\omega}_i$.

A non-zero value of order parameter Ω for all λ_2 except $\lambda_2 = 100$, tells us that the system has broken symmetry and constitutes a net average motion.

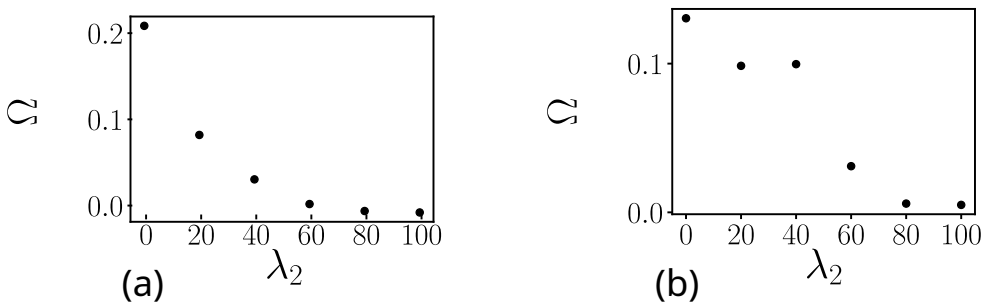

Figure 4.12: Variation of order parameter Ω with λ_2, keeping other damping parameters fixed : $a_1 = a_2 = -0.3$, $b_1 = b_2 = 0.4$ and $\lambda_1 = 100$. The interaction parameters for Fig. 4.12 (a) and (b) are for the exact same regimes that correspond to kind of motion shown in Fig. 4.6 and 4.7 respectively.

Even with the same parameters λ_2, a_i, and b_i, different clusters may exhibit different values of Ω due to variations in internal dimer arrangements and inherent stochasticity induced by thermal fluctuations.

4.6 Other Emergent Configurations

Competing Orders and Local Anti-Alignment In addition to coherent translational and rotational states, the system can also exhibits *antiferromagnetic-like spatial ordering* as shown in Fig. 4.13 in a parameter regime comprising long attraction and repulsion range $\sigma = 2$, $r_l = 2.2$. These configurations arise from competing local preferences imposed by the damping asymmetry and steric constraints,

leading to patterns that lack global alignment but show local anti-alignment. Here the alignment of dimers in one direction generates a stronger torque than the anti-torque produced by the opposing alignments, driving rotational motion despite the local anti-alignment. The link to the video can be found here.

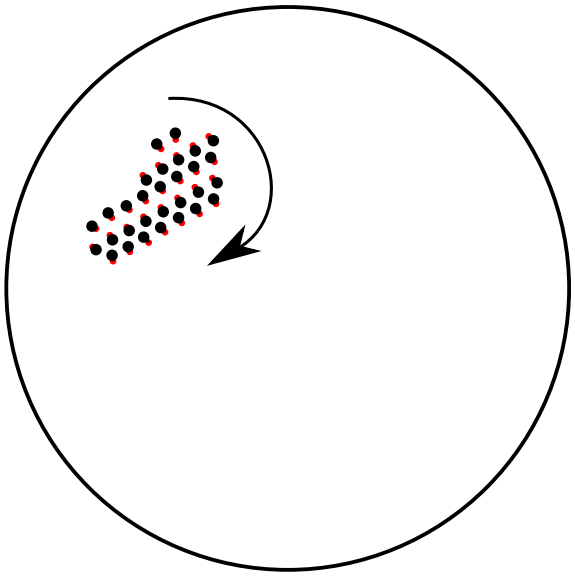

Figure 4.13: Snapshot of Anti-ferromagnetic like ordered dimers showing spontaneous rotation. Parameter: $\sigma = 2$, $r_l = 2.2$ and $\Delta t = 10^{-5}$. See video here.

Emergent Rotating Clusters: Between Vortex and Swarm

In a parameter regime of intermediate attraction and repulsion range $\sigma = 1.5$, $r_l = 2$, many-body dimers organize into a loosely bound rotating cluster, exhibiting persistent and coherent angular motion. While a central region behaves like a rigidly rotating core, this core is not static, it can slowly shift its position within the cluster over time, reflecting the fluid and adaptive nature of the system. The outer layer remains highly dynamic: dimers continuously rearrange, flip orientation, and intermittently join or leave the main vortex structure. This leads to a hybrid state, combining global rotational coherence characteristic of a vortex with the local plasticity and reconfiguration typical of swarming. The cluster as a whole exhibits sustained angular momentum and global chiral order, while the local structure remains fluid and adaptable.

The interplay between a transiently stable core and a responsive periphery allows the system to sustain collective motion while adapting to fluctuations, all within an

equilibrium framework. The link to the video can be found here.

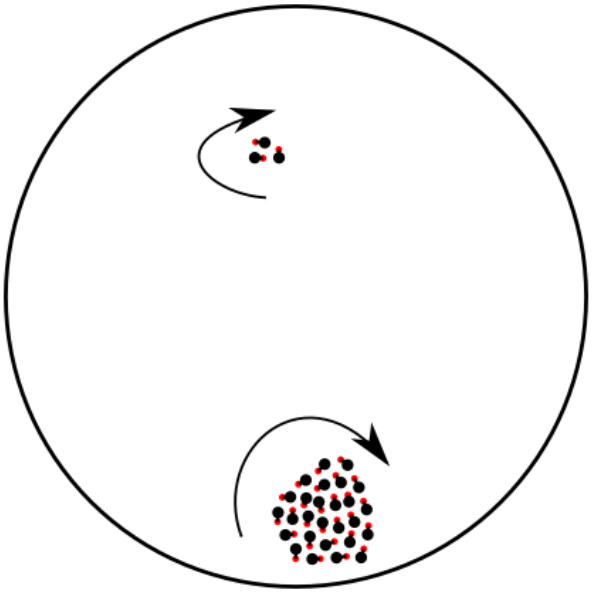

Figure 4.14: Snapshot of more emergent structures showing chiral symmetry broken rotating structures. Parameter: $\sigma = 1.5$, $r_l = 2$ and $\Delta t = 10^{-5}$

Table 4.5: Summary of simulation parameters and corresponding emergent behaviors shown

Label	σ	r_l	Δt	**Observed Behavior**
(a)	1.5	3.0	10^{-4}	Flocking behavior with coherent transport
(b)	2.0	3.0	10^{-5}	Swarming behavior with clustered transport
(c)	1.0	1.8	10^{-5}	Crystal like structures rotation in broken chiral symmetry
(d)	1.0	2.2	10^{-4}	Chiral symmetry broken triangular structures
(e)	2.0	2.2	10^{-5}	Anti-ferromagnetic structure with rectified rotation
(f)	1.5	2.0	10^{-5}	Hybrid swarm-vortex rotating structures

4.7 Conclusion

In this chapter, we have explored thermal fluctuation driven collective/directed transport of many-body interacting dimers in equilibrium whose constituent particles have a coordinate-dependent damping and diffusion related by the Stokes-

Einstein (fluctuation-dissipation) relation. The coordinate-dependent damping/diffusion in a homogeneous, isotropic heat-bath drives this coordinated motion in the absence of any active force. The most striking consequence of the existence of such motions under Itô distribution is that the pathway of structure formation in complex molecules or collections of them may not only be determined by fluctuations over a free energy surface, but complemented by characteristic motions at different free energy states. Moreover, the results shown here provides a minimal and tractable novel approach for understanding how chirality can organize motion at mesoscopic scales in soft-matter systems using equilibrium fluctuations.

These results challenge the conventional assumption that directed transport requires non-equilibrium conditions, and open up new possibilities for understanding fluctuation-driven organization in biological systems, soft matter, and synthetic active materials. Our findings underscore the importance of incorporating spatial inhomogeneities in theoretical descriptions of equilibrium systems and provide a foundation for exploring novel forms of passive transport in structured thermal environments.

5

Non-Equilibrium Transients in Itô Dynamics: Effects and Consequences

In the preceding chapters, we examined how spatial asymmetries in damping can drive spontaneous rectified transport in both single and many-body systems under equilibrium or near-equilibrium conditions, as described within the Itô framework. These studies demonstrated that detailed balance does not preclude the emergence of steady directed motion when equilibrium fluctuations are coupled to spatially varying damping (or mobility) in a structured symmetry-broken object.

In this chapter, we investigate non-equilibrium transient transport phenomena that emerge in systems with spatially varying diffusivity within the rigorous framework of Itô dynamics. At the heart of these effects lies the principle that gradients in diffusivity can induce transient directed motion even in the absence of external forces. One manifestation of this is the phenomenon of entropic pulling: a diffusion gradient(or diffusivity-dependent entropy gradient) driven transient transport towards regions of high entropy. From another perspective, the same mechanism gives rise to what we term a diffusion diode, wherein the system exhibits asymmetric transport due to an underlying diffusion (or entropic) gradient. While the former emphasizes the thermodynamic tendency of the system to maximize accessible microstates, the latter highlights the functional outcome: directional bias in transport. These are not distinct phenomena but rather two interpretations of a

common underlying process transport driven by internal gradients in diffusivity (entropy). This unified view provides a powerful lens through which to understand directional motion in soft and biological matter, where such gradients arise naturally from confinement, crowding, or environmental heterogeneity.

These mechanisms are particularly relevant for biological systems at sub-micron scales, where motion is dominated by diffusion and viscous damping, and where spatial inhomogeneities such as those arising from crowded environments, membranes, or confining geometries, lead to coordinate-dependent diffusivity [24, 65–69]. This chapter is adapted from Ref. [70].

5.1 Itô Diffusion: Interpretation and Thermodynamic Implications

The equilibrium distribution $P(x)$ for a Brownian particle (BP) undergoing coordinate-dependent diffusion, in contact with a heat bath at temperature T, in the Itô interpretation (for derivation, see appendix B) is given by:

$$P(x) = C\frac{D_0}{D(x)}\exp\left(-\frac{U(x)}{k_BT}\right), \tag{5.1.1}$$

where C is a normalization constant with dimension of inverse length, $D(x)$ is the position-dependent diffusivity, D_0 is the constant bulk diffusivity, k_BT is thermal energy and $U(x)$ is the potential.

This expression can be rewritten in a more illuminating form [38] as:

$$P(x) = C\exp\left(-\frac{1}{k_BT}\left[U(x) - TS_{D(x)}\right]\right) = C\exp\left(-\frac{\mathcal{F}(x)}{k_BT}\right), \tag{5.1.2}$$

where $S_{D(x)}$ is the excess entropy arising from inhomogeneities in diffusivity or damping and $\mathcal{F}(x)$ represents the free energy, expressed as:

$$\mathcal{F}(x) = U(x) - TS_{D(x)}, \quad \text{with} \quad S_{D(x)} = k_B\log\left(\frac{D_0}{D(x)}\right). \tag{5.1.3}$$

This entropy term $S_{D(x)}$ reflects an increased density of accessible microstates in regions of reduced diffusivity. Suppose $D(x)$ represents the diffusivity of BP near

interface/other entities, then $D(x) \leq D_0$ [24]. Consequently, the inhomogeneity entropy is non-negative. A natural choice for D_0 is the constant bulk diffusivity justified by the fact that in the zero-temperature limit ($T \to 0$), spatial inhomogeneities vanish and the system becomes homogeneous with $D(x) \to D_0$, making the inhomogeneity entropy term vanish smoothly.

Phase-space perspective and minimum state volume:

To understand the origin of this entropy term, we consider the classical phase space of the Brownian particle. In quantum mechanics, Planck's constant h sets a lower bound on phase space volume per state. In classical stochastic dynamics, a similar role is played by the diffusivity D, which determines the minimum resolvable phase space volume over the relaxation time scale [23, 38].

Consider Brownian motion in a homogeneous medium with position x, mass m, velocity v, constant damping Γ (constant diffusivity D_0, where $D_0 = k_B T/\Gamma$) in contact with a thermal bath at temperature T. The velocity spread of the BP at temperature T is $\Delta v = \sqrt{k_B T/m}$, and the characteristic relaxation time is $\tau = m/\Gamma = 1/\zeta$, using $\Gamma = m\zeta$. The characteristic time ζ^{-1} is the average minimum relaxation time below which BP doesn't come in equilibrium with the bath. Therefore, in time scales shorter than ζ^{-1}, BP neither gets access to the temperature of the bath nor does the Stokes-Einstein relation hold. It means that in the characteristic time ζ^{-1}, the particle's position uncertainty is $\Delta x = \Delta v \times \tau = \Delta v/\zeta$, giving a phase-space cell size:

$$\Delta x\, \Delta v = \frac{k_B T}{m\zeta} = \frac{k_B T}{\Gamma} = D_0, \tag{5.1.4}$$

Thus, D_0 plays the role of the *minimum phase space volume* or *cell size* available to the Brownian particle in the bulk. This volume corresponds to one thermodynamic state in the bulk.

For coordinate-dependent damping, the local relaxation time is $\tau(x) = 1/\zeta(x)$, so the corresponding phase-space volume becomes $D(x)$. Hence, the number of distinguishable microstates available in a bulk-sized volume D_0 is:

$$\Omega(x) = \frac{D_0}{D(x)}. \tag{5.1.5}$$

The term $\Omega(x)$ denotes the microcanonical contribution to the entropy, represent-

ing the density of accessible states at position x. This ratio quantifies how many microstates are available to the system at a specific position x relative to the bulk. Near an interface or wall where $D(x) < D_0$, more microstates fit within the same phase-space volume, leading to a higher local entropy. A schematic is shown in Fig. 5.2. This provides a thermodynamic explanation for why a Brownian particle spends more time near interfaces, an effect that is experimentally observed.

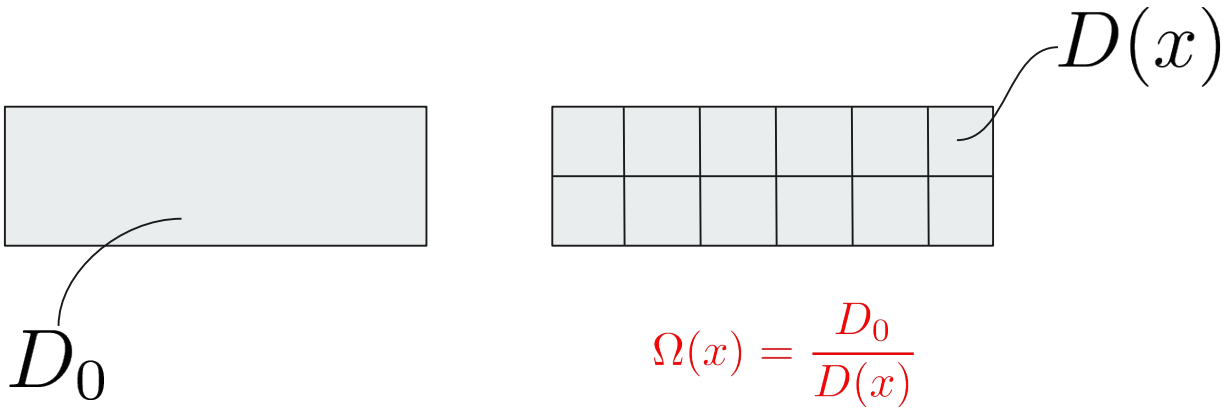

Figure 5.1: Emergence of micro-canonical entropy shown in the schematic.

For example, Carbajal-Tinoco et al. [23, 53] (insets of Fig. 4) observe a clear shift in the peak of the BP's position distribution toward confining walls, with a long tail extending into the bulk. Importantly, the same trend is observed near both the top and bottom surfaces, ruling out gravity as a cause. This behavior is consistent with the entropy-driven accumulation of probability in regions of lower diffusivity.

Emergence of Entropic pulling force:

Due to the presence of the excess entropy $S_{D(x)}$, in the presence of specially varying diffusivity/damping, the free energy landscape gets modified. As a result, one could associate an emergent thermodynamic force - an *entropic force* f_E, which reflects the system's tendency to explore regions of higher entropy.

$$f_E(x) = -\frac{d}{dx}\mathcal{F}(x) = T\frac{dS_{D(x)}}{dx} = -k_B T\frac{d}{dx}\log D(x)$$

This entropic "pulling" force drives the system toward regions of lower diffusivity (higher damping) under coordinate-dependent damping. In these regions, the density of accessible microstates is higher, favoring particle accumulation due to

increased local entropy. This mechanism arises because the system tends to move in a direction that maximizes its entropy.

While the force interpretation offers intuitive insight, it is strictly valid during the system's transient relaxation dynamics (until the position degree of freedom hasn't reached the equilibrium steady state). In this non-equilibrium transient regime, detailed balance is broken in position space, and a nonzero probability current exists. During this phase, the entropic (or so-called kinetic) force guides the system toward regions of higher entropy. However, once the equilibrium position distribution is attained, i.e., when the entropy is maximized, the probability current vanishes, detailed balance is restored, and the system reaches the Itô equilibrium distribution $P(x)$ (see Eq. 5.1.1).

5.2 Diffusion Current Density in Itô diffusion

To further clarify the origin of transport mechanisms in the Itô setting, consider the diffusion current density arising from spatially varying diffusivity and particle concentration. From the Itô Fokker-Planck (see appendix B), the diffusion current density can be expressed as:

$$-\frac{\partial}{\partial x}(D(x)P(x,t) = -D(x)\frac{\partial P(x,t)}{\partial x} - P(x,t)\frac{\partial D(x)}{\partial x}$$

The first part of this current is the well-known Fickian diffusion current due to concentration gradient, i.e., $-D(x)\frac{\partial}{\partial x}P(x,t)$, which drives the flow of particles opposite to the concentration gradient to even out the density. This part of the diffusion current always occurs irrespective of the presence of a diffusion gradient because it depends on the gradient of the particle concentration. However, the second part of the diffusion current $-P(x,t)\frac{\partial}{\partial x}D(x)$ is the diffusivity-gradient dependent legitimate diffusion current, and this current exists in the direction opposite to the diffusivity gradient. It is easy to see from this that the diffusion-gradient induced transient velocity associated with this component of the diffusion current is given by $v_{D(x)} = -\frac{\partial D(x)}{\partial x}$, reflecting a net flow from regions of higher diffusivity to lower diffusivity.

5.3 From Transients to Steady-State: Directional Response in an Itô Process

Coordinate-dependent damping and diffusion arise near boundaries or interfaces due to slow hydrodynamic modes generated by the thermal fluctuations of Brownian particles. In the following sections, we investigate the effects and implications of Itô diffusion by analyzing two simple toy models, both studied through numerical simulations. These examples aim to capture the consequences of having coordinate-dependent damping that emerges as a result of confinement. In this simplified approach, we have neglected hydrodynamic interactions between particles arising from their proximity to one another. Note that the BP is always in local equilibrium with the heat bath, thus Stokes-Einstein is always satisfied locally, i.e. $D(x) = \frac{k_B T}{\Gamma(x)}$ in the overdamped dynamics. Below, we discuss the first toy model, called the Diffusion diode model.

5.3.1 Non-Equilibrium Directional Response: Diffusion Diode Behavior

We consider a system of interacting Brownian particles confined inside a three-dimensional box maintained at thermal equilibrium in contact with a heat bath at temperature T. The particles interact with each other via excluded volume interaction and evolve via overdamped stochastic (Brownian) dynamics under the Itô interpretation.

A key feature of this model is the presence of a spatially varying damping coefficient, such that each particle's damping (thereby, diffusivity) depends on its instantaneous position within the box. This position-dependent damping sets an inhomogeneous diffusivity across the system despite the uniform thermal environment.

We set up a confinement box in the first octant, with the origin $(0, 0, 0)$ coincident on one of the corners. All distances are measured from the origin. The length of the box in y and z directions are equal by construction. The box aligned with the Cartesian axes is partitioned along the x axis into three continuous cuboidal regions: R_1, R_2, and R_3, such that R_1 and R_3 are geometrically identical and symmetric with respect to the central region R_2 as shown in Fig. 5.2. The damping

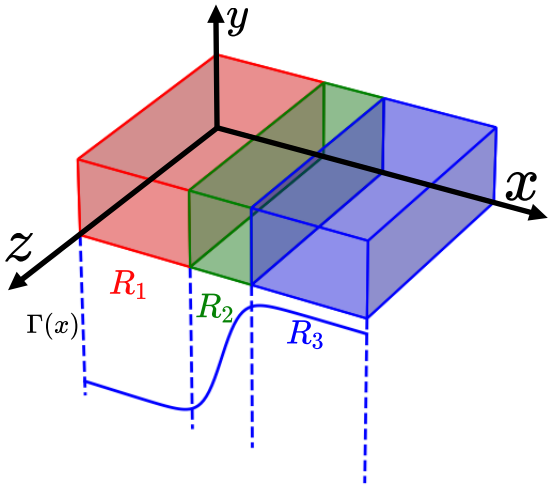

Figure 5.2: Set up of the model (not drawn to scale). The box consists of three regions R_1, R_2 and R_3, with R_1 and R_3 identical in geometry. Damping increases smoothly from R_1 to R_3, saturating in the outer regions. The box has an equal extent in y and z directions.

coefficient is chosen to be a smooth, monotonically increasing function. It remains approximately constant in R_1, increases steadily within R_2, and again saturates to a different constant value (approximately) in R_3 as evident from Fig. 5.2.

Suppose $i, j \in \{1, 2, \ldots, N\}$ denote the particle (index). Coordinate $\mathbf{r}_i$ denotes the three-dimensional position coordinate of the i^{th} particle and $\boldsymbol{\eta}_i(t)$ represent independent, three-component vector continuous, Markov, Gaussian white noises acting on the i^{th} particle, whose cartesian representation reads as:

$$\boldsymbol{\eta}_i(t) = \eta_i^x(t)\,\hat{x} + \eta_i^y(t)\,\hat{y} + \eta_i^z(t)\,\hat{z}, \quad \text{for } i = 1, 2, ..., N.$$

Each component $\eta_i^{\mathcal{S}}(t)$ (with $\mathcal{S} \in \{x, y, z\}$) has zero mean, unit variance, is delta correlated in time, and is not correlated between the labels of the constituents and the spatial components. This means, $\langle \eta_i^{\mathcal{S}}(t) \rangle = 0$, and $\langle \eta_i^{\mathcal{S}}(t_1) \eta_j^{\mathcal{S}'}(t_2) \rangle = \delta_{ij}\,\delta_{\mathcal{S}\mathcal{S}'}\,\delta(t_1 - t_2)$. The particles in this model experience excluded volume interaction and the effect of confinement potential, in case they try to cross the boundary.

The excluded volume interaction between different particles i and j is modeled

by a repulsive harmonic potential V_{ij}.

$$V_{ij} = \begin{cases} \frac{1}{2}\kappa(|\mathbf{r}_i - \mathbf{r}_j| - r_l)^2 & \text{if } |\mathbf{r}_i - \mathbf{r}_j| < r_l, \\ 0 & \text{if } |\mathbf{r}_i - \mathbf{r}_j| \geq r_l, \end{cases} \tag{5.3.1}$$

where κ measures the strength of repulsion, r_l is the proximity scale below which repulsion is felt by particles. Suppose ϕ_i represents the net potential on the i^{th} particle due to other particles, then $\phi_i = \sum_j V_{ij}(1 - \delta_{ij})$, where δ_{ij} is the standard Kronecker delta function. The corresponding force felt is $-\nabla_{\mathbf{r}_i}\phi_i$.

The confinement interaction is modeled by a piecewise harmonic repulsive potential applied independently to each Cartesian component of the particle. Suppose $b_i = \{x_i, y_i, z_i\}$ and $l_b = \{l_x, l_y, l_z\}$ constitute ordered pairs, where elements of b_i represent cartesian components of i^{th} particle's position and elements of l_b represent edge-length of the box in x, y and z direction respectively. The confining potential on i^{th} particle corresponding to each component of b_i and l_b is denoted by V_{b_i}.

$$V_{b_i} = \begin{cases} \frac{1}{2}\kappa b_i^2 & \text{if } b_i < 0, \\ 0 & \text{if } 0 \leq b_i \leq l_b, \\ \frac{1}{2}\kappa(b_i - l_b)^2 & \text{if } b_i > l_b. \end{cases} \tag{5.3.2}$$

The overall confining potential $V_c = \sum_{b_i} V_{b_i}$. $\mathbf{F}_i$ is the instantaneous force amounting to the total contribution of excluded volume interaction and the confinement felt by the i^{th} particle, in case it tries to cross the boundary. Then, the net force felt by i^{th} particle due to excluded volume and confinement effects is $\mathbf{F}_i = (-\nabla_{\mathbf{r}_i}\phi_i) + (-\nabla_{\mathbf{r}_i}V_c)$.

The damping profile chosen is a monotonically increasing, continuous, and differentiable function modeled by a hyperbolic tangent function. The following functional form of position-dependent damping Γ_i experienced by i^{th} particle, is used in simulations:

$$\Gamma_i = A \tanh \beta(x_i - x_0) + (A + 1),$$

where x_0 is shifted origin and A is the amplitude parameter, where β is the measure

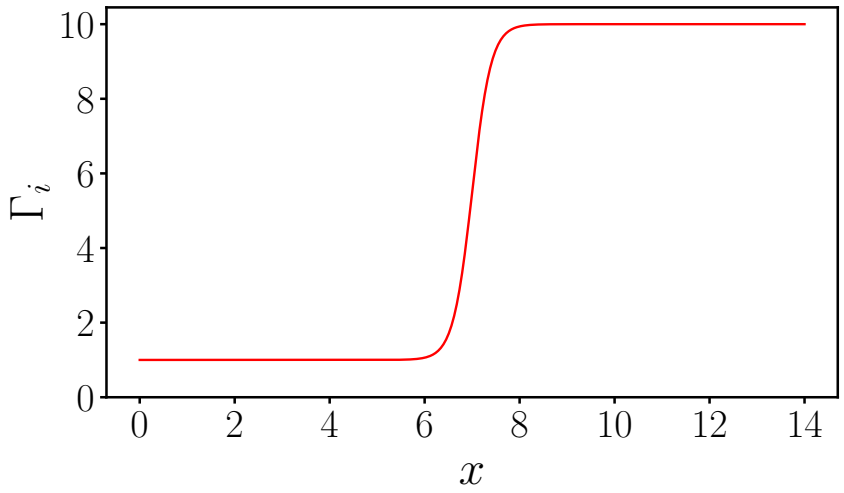

Figure 5.3: Tangent hyperbolic damping profile for typical parameters used in simulation: $A = 4.5$, $\beta = 2.5$ and $x_0 = 7$.

of the steepness of the profile in the neighbourhood of x_0 and effectively is a measure of the width of the region R_2 in x direction. The last term in the above expression of damping accounts for the vertical shifting of the standard hyperbolic tangent function to ensure that damping is always positive. We have chosen x_0 to be the midpoint of the length of the three-dimensional box in the x direction. Following overdamped stochastic differential equations govern the motion of the particles.

$$\frac{d\boldsymbol{r}_i}{dt} = \frac{\boldsymbol{F}_i}{\Gamma_i} + \sqrt{\frac{2k_BT}{\Gamma_i}}\boldsymbol{\eta}_i(t). \tag{5.3.3}$$

Simulation Details

Thermal energy k_BT and the characteristic length scale r_l are used as reference parameters for energy and length, respectively. The damping chosen is of the order unity in the simulations. The simulation parameters listed in table 5.1 are kept fixed throughout the analysis in this diffusion diode section.

To investigate the influence of the damping gradient, simulations are performed for three different values of the steepness parameter β, which controls the sharpness of the transition region R_2 along the x-axis and parameters are shown in table 5.2. A smaller width of R_2 corresponds to a higher gradient in the damping profile.

Table 5.1: Fixed Simulation Parameters

Parameter	**Value**	**Description**
k_BT	1	Thermal energy scale
$r_{\min}$	0.25	Characteristic interaction length scale
N	100	Number of particles
l_x	14	Box length in x-direction
l_y, l_z	5	Box length in y- and z-direction
κ	1000	Strength of repulsive harmonic interaction
A	4.5	Amplitude of the damping function
x_0	7	Midpoint of damping gradient along x
Δt	5×10^{-4}	Simulation time step

Table 5.2: Simulation parameters for varying damping profiles

Steepness parameter β	**Approx. width of region R_2**
2.5	4
3.3	3
5.0	2

Two Settings of the Model

We study this model under two different initial conditions: in the first setting, all particles are randomly distributed in region R_1, while in the second, they are initialized in region R_3. We generate ensembles and obtain an average over them to study quantities of interest. In either case, these initializations create a concentration gradient that, under normal (homogeneous) diffusion, would relax toward a uniform distribution across regions R_1, R_2, and R_3, with occupation numbers proportional to their respective volumes.

However, the presence of a spatially varying damping profile, treating it as an Itô process, modifies this behavior by inducing an additional transient current in the direction of higher damping (entropy). This transient current is diffusion-gradient driven, which guides particles toward high-damping regions. Equivalently, it can be interpreted as entropic gradient-driven, which pulls particles (even in the absence of external forces) to diffuse toward regions of lower diffusivity (i.e., higher damping) in order to maximize their entropy. Consequently, instead of reaching a uniform steady state as in homogeneous diffusion, the particles are non-uniformly distributed

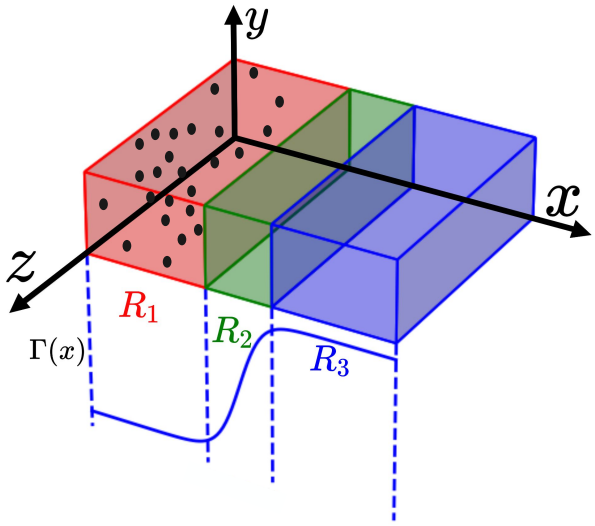

Figure 5.4: Setting I: All particles are randomly initialized in the region R_1 (schematic).

in steady state. The particles accumulate where the entropy is higher (or damping is stronger), in accordance with the Itô equilibrium steady-state distribution.

Setting I: Particles Initialized in Region R_1: Forward Bias

In this setting, particles are initially placed randomly in region R_1 as depicted schematically in Fig. 5.4. As the system evolves, the particles experience an entropic pull toward regions of higher damping, particularly towards R_3, as explained above. This causes the transient currents driven by the concentration gradient and the entropic pull to align, resulting in a **forward bias** like situation. The gradient in diffusivity acts like a one-way filter, preferentially guiding particles forward. The schematic of the resulting distribution of particles is displayed in Fig. 5.5(a).

Fig. 5.5(b) presents the time evolution of the average particle occupancy n_f in region R_3 for varying strengths of the damping gradient. n_f is obtained by performing an ensemble average over 100 independent ensembles for each value of β, which corresponds to a unique width of R_2. The narrowing of R_2 (smaller width) sharpens the gradient, boosting the entropic force and causing a higher particle accumulation in R_3, which is also evident from Fig. 5.5(b).

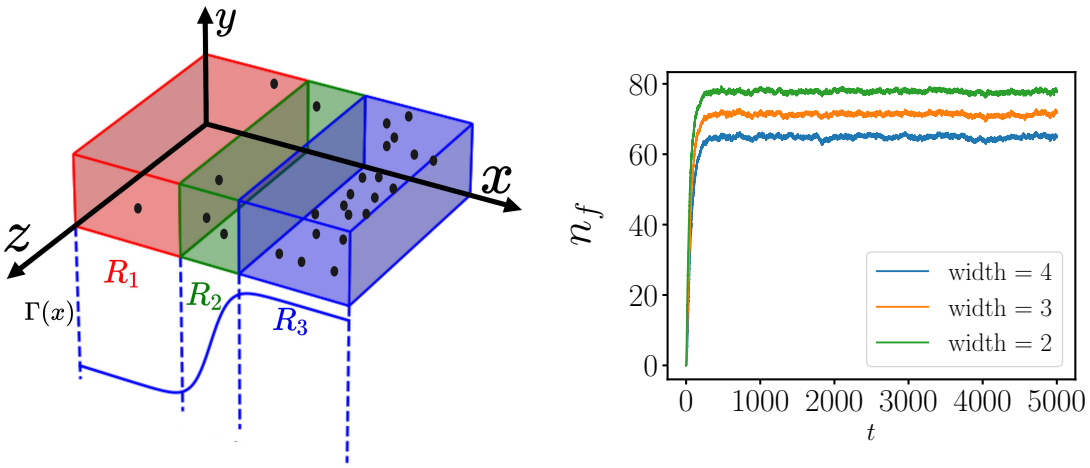

(a) (b)

Figure 5.5: Setting I: (a) Schematic of the particle distribution at large times. (b) Time evolution of the average particle occupation in region R_3, computed over 100 ensembles, for various widths of R_2 using simulation parameters stated in table 5.1 and table 5.2, showing forward bias behavior.

Setting II : Particles initialized in the region R_3: Reverse bias

.

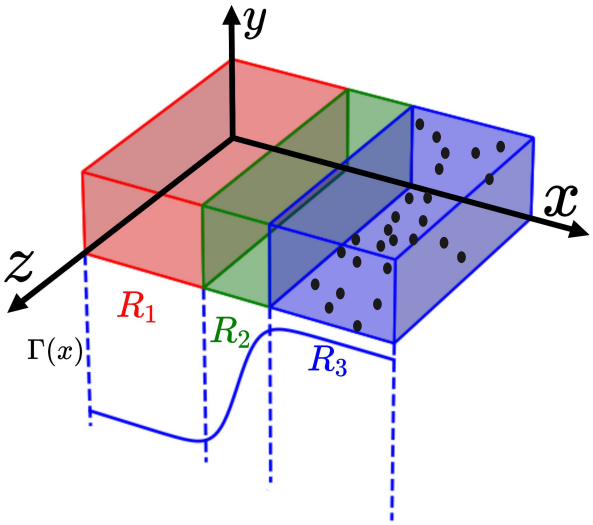

Figure 5.6: Setting II: All particles are randomly initialized in R_3 (schematic).

In this complementary setting, all particles are initially placed in region R_3 as

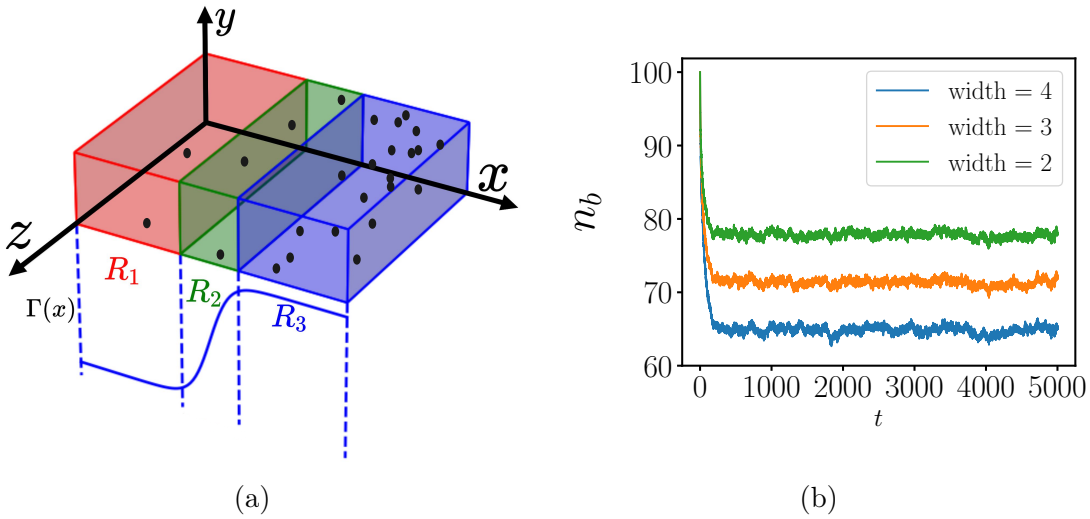

(a) (b)

Figure 5.7: Setting II: (a) Schematic of the particle distribution at large times. (b) Time evolution of the average particle occupation in region R_3, computed over 100 ensembles, for various widths of R_2 using simulation parameters stated in table 5.1 and table 5.2, showing reverse bias behavior.

shown in 5.6. As the system evolves, particles initially positioned in region R_3 encounter an opposing entropic gradient as they attempt to diffuse toward R_1. The transient currents driven by the concentration gradient and the entropic gradient act in opposite directions, creating a **reverse bias** configuration, where the entropy (or damping) gradient resists particle movement toward regions of lower damping (higher diffusivity), effectively acting as an entropic (diffusive) barrier. This barrier generates a directional bias that inhibits particle flux, preventing significant movement from R_3 to R_1. The particles eventually distribute non-uniformly in accordance with the resulting Itô distribution in this reverse bias condition, which is schematically depicted in Fig. 5.7(a).

Fig. 5.7(b) shows the time evolution of the average particle occupancy n_b in region R_3 for different damping gradient strengths. The narrowing of R_2 (smaller width) sharpens the gradient, intensifying the entropic barrier and thereby opposing particle escape from R_3. This is evident from Fig. 5.7(b), where the region with the smallest width acts as a robust barrier, effectively confining particles within region R_3 and preventing their escape, unlike larger widths where particles more easily diffuse into neighboring regions. We verify that at long times, when the average

particle occupation becomes time-independent for both settings I and II, the total diffusion current vanishes, as the product $P(x)D(x)$ remains constant, which serves as a confirmation that the system has reached equilibrium steady state, consistent with the Fokker-Planck description of an Itô process.

In the next section, we discuss the second model that we have considered in our work.

5.3.2 From Wide to Narrow: Entropic Effects on Polymer Transport

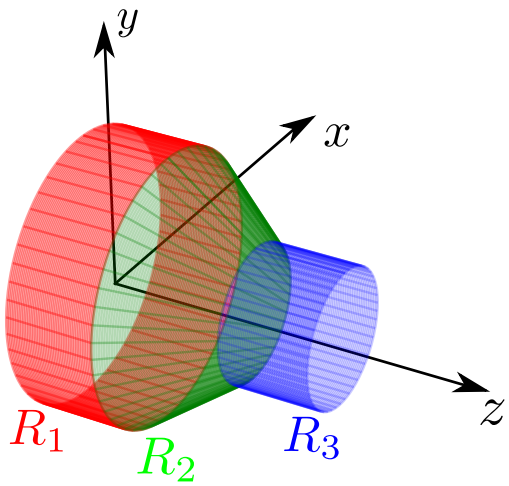

Figure 5.8: Funnel geometry (perspective view, not drawn to scale) with three regions: R_1 (cylinder, radius $\mathcal{R}$), R_2 (truncated cone, radius $\mathcal{R}$ to r), and R_3 (cylinder, radius r). The z-axis is the axis of symmetry, with the origin at the centre of the rear circular base of R_1.

In biological systems, macromolecules translocate through constricted and heterogeneous environments. These confined spaces can impose hydrodynamic effects, influencing how macromolecules move and interact. To explore the effects of hydrodynamical effects (manifested as damping/diffusivity becoming position-dependent) on a mesoscopic macromolecule (a polymer), we consider the following simple model. Consider a polymer chain composed of interacting Brownian particles confined within a three-dimensional funnel-like geometry in thermal equilibrium with a heat reservoir at temperature T. The interactions between nearest neighbors are modeled as attractive at large distances and repulsive at short distances, with all monomer pairs interacting via excluded volume forces to prevent overlap.

The funnel geometry, illustrated in Fig. 5.8, consists of three continuous regions: R_1, R_2, and R_3. Region R_1 is a hollow right circular cylindrical region of radius $\mathcal{R}$. Region R_2 is a hollow, truncated cone-shaped region (or frustum of a cone) with a big radius $\mathcal{R}$ and a small radius r. Region R_3 is a hollow right circular cylindrical region of radius r. All regions have equal length h. We set our reference point, the origin, at the centre of the rear circular base (radius $\mathcal{R}$) of the funnel, which marks the beginning of region R_1. The positive direction of the z axis is a ray coincident with the axis of symmetry of the funnel emerging from the origin towards other regions, with the x and y axes perpendicular to the z axis. The funnel's shape is designed to model the effect of spatial confinement, where the volume available for the particle motion decreases as the particle moves from the wider to the narrower regions, especially in R_2.

In a more detailed model, one could calculate the exact distance of each particle from the nearest wall and define damping as a function of this separation. However, we take a more simplified approach by modeling the damping of a particle (monomer) in each region of the funnel as inversely proportional to the radius of curvature. This approach reflects the idea that as the particle moves toward narrower regions of the funnel, such as in R_2, the radius of curvature decreases, and the available physical space for particle motion becomes more confined. As a result, the damping experienced by the particle increases, simulating the effects of proximity to the walls without explicitly calculating the distance to the periphery. This simplification is effective because it captures the essential hydrodynamic behavior, that damping increases as the particle moves closer to the boundaries [24], while remaining computationally manageable. It is important to note that in this simple model, we do not consider the hydrodynamic effect on the damping of a particle due to its neighbors. Our goal is to effectively model the effect of damping due to confinement.

Suppose $i, j \in \{1, 2, \ldots, N\}$ denote the monomer index of the polymer chain confined within a three-dimensional funnel-like geometry. Coordinate $\mathbf{r}_i$ denote the three-dimensional position coordinate of i^{th} particle. We define the separation vector as $\mathbf{r}_{ij} = \mathbf{r}_i - \mathbf{r}_j$, and denote magnitudes as $r_i = |\mathbf{r}_i|$ and $r_{ij} = |\mathbf{r}_i - \mathbf{r}_j|$. The monomer experiences following **interaction potential:**

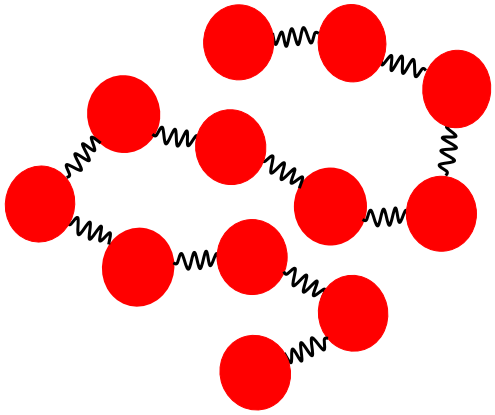

Figure 5.9: Schematic of Brownian chain (not drawn to scale)

Interaction Potential:

- **Nearest Neighbor Interaction:** The nearest neighbor monomers interaction is modeled by a harmonic potential of the form

$$V_{NN}(r_{ij}) = \frac{\alpha}{2}(r_{ij} - r_{\min})^2,$$

where α is the bond stiffness, r_{ij} is the separation between monomers i and j, and $r_{\min}$ is the equilibrium bond length.

- **Excluded Volume Interaction:** All other monomer pairs interact via a Weeks–Chandler–Andersen (WCA) potential, given by

$$V_O(r_{ij}) = \begin{cases} 4\epsilon \left[\left(\frac{\sigma}{r_{ij}}\right)^{12} - \left(\frac{\sigma}{r_{ij}}\right)^{6} \right] + \epsilon, & r_{ij} < 2^{1/6}\sigma \\ 0, & r_{ij} \geq 2^{1/6}\sigma \end{cases},$$

where ϵ is the interaction strength and σ is the interaction range.

The z coordinate determines the region a particle occupies in the funnel, which in turn specifies the cross-sectional radius $s(z)$. The radius of cross-section $s(z)$ is related to z-coordinate as:

$$s(z) = \begin{cases} \mathcal{R}, & 0 \le z \le h \\ r + (2h - z)\left(\frac{\mathcal{R}-r}{h}\right), & h \le z \le 2h \\ r & 2h \le z \le 3h \end{cases} .$$

$s(z_i)$ (or s_i) will be the radius of cross-section corresponding to the coordinate z_i for the i^{th} monomer. Due to the cylindrical symmetry of the funnel, the confining potential at the boundary and the terminal ends can be conveniently expressed in cylindrical coordinates, $\{\boldsymbol{r}_i\} \equiv \{\rho_i, \phi_i, z_i\}$. ρ_i is the radial distance of the i^{th} monomer from the z-axis, and ϕ_i is the azimuthal angle in the x-y plane, defined as: $\rho_i = \sqrt{x_i^2 + y_i^2}$, $\quad \phi_i = \tan^{-1}\left(\frac{y_i}{x_i}\right)$. The funnel boundary comprises two distinct surfaces: a curved cylindrical surface and a flat circular surface at the terminal ends of the funnel along the z-axis.

- **Confinement interaction**: The confinement interaction is defined separately for these surfaces, each modeled as a harmonic repulsion. Let Φ_c and Φ_p represent the confining potentials experienced by the i^{th} monomer when it overshoots the curved cylindrical boundary and the flat(or plane) circular periphery, respectively:

$$\Phi_c(\rho_i) = \begin{cases} 0 & \text{if } \rho_i < s_i, \\ \frac{\kappa}{2}(\rho_i - s_i)^2 & \text{if } \rho_i \ge s_i. \end{cases} \quad \text{and} \quad \Phi_p(z_i) = \begin{cases} \frac{\kappa}{2} z_i^2 & \text{if } z_i \le 0, \\ 0 & \text{if } 0 < z_i < 3h, \\ \frac{\kappa}{2}(z_i - 3h)^2 & \text{if } z_i \ge 3h. \end{cases}$$

  where κ denotes the strength of the harmonic repulsion. Consequently, the overall confining potential V_B can be expressed as: $V_B = \Phi_c + \Phi_p$.

$\boldsymbol{\eta}_i(t)$ is a three-component Gaussian white noise with properties and cartesian representation, as discussed in the former section (diffusion diode) of this chapter. The damping function for any i^{th} monomer of the polymer in this model has the following simplistic form (unless stated otherwise) $\Gamma_i = \frac{A}{s(z_i)}$, where A controls damping strength.

The dynamics of the i^{th} monomer under the Itô framework is described by the stochastic differential equation:

$$\frac{d\mathbf{r}_i}{dt} = -\frac{1}{\Gamma_i}\nabla_{\mathbf{r}_i}\mathcal{V}_i + \sqrt{\frac{2k_BT}{\Gamma_i}}\,\boldsymbol{\eta}_i(t),$$

where $\mathcal{V}_i$ is the total potential acting on the i^{th} monomer, given by :

$$\mathcal{V}_i = \sum_{j=i\pm1} V_{NN}(|\mathbf{r}_{ij}|) + \sum_{\substack{j\neq i \\ j\neq i\pm1}} V_O(|\mathbf{r}_{ij}|) + V_B(\mathbf{r}_i).$$

which is the sum of the nearest-neighbor interaction potential, the interaction potential for non-neighboring monomers, and the confining potential. Note that for the end monomers, the nearest-neighbor interaction term involves only one adjacent monomer due to the absence of a second neighbor.

5.4 Simulation Details

Thermal energy k_BT and r_{min} serve as reference energy and length scales in our simulations, both normalized to unity. The damping (thus, diffusivity) is of order unity in the simulations. The parameters used in simulation are displayed in table 5.3.

Table 5.3: Simulation Parameters used in Fig. 5.10

Parameter	**Value**	**Description**
k_BT	1	Thermal energy scale (normalized)
$r_{\min}$	1	Characteristic length scale (normalized)
N	25	Number of monomers
$\mathcal{R}$	3	Rear radius of funnel
r	2	Front radius of funnel
h	27.5	Height of funnel
α	100	Strength of attractive bonding potential
ϵ	1.5	Depth of Lennard-Jones-like potential
σ	1.5	length scale in *WCA*
κ	1000	Stiffness of confinement or repulsive walls
A	4	Amplitude in damping profile
Δt	10^{-4}	Time step

Homogeneous damping vs Coordinate dependent damping:

In the first part of our exploration, we investigate the influence of spatially varying damping on transport. We compare the dynamics of a polymer under two distinct damping scenarios (or cases). Case I corresponds to damping-dependent on z coordinate as $\Gamma_i = \frac{A}{s(z_i)}$. Case II corresponds to homogeneous damping. The polymer is initialized in an identical configuration for both cases. The configuration being an unfolded linear chain aligned along the z axis, fully contained within region R_1 across all ensemble realizations for both cases. Each ensemble in the simulation is assigned a unique random-number seed, generating a distinct Gaussian noise sequence (zero mean, unit variance, no cross-correlations). This sequence is then applied identically in both the homogeneous and coordinate-dependent damping cases, ensuring that any observed differences in dynamics are attributable solely to the presence of coordinate-dependent damping/diffusivity. The time evolved trajectory of the average center of mass of the chain (of the fifty-realization ensemble) in the z direction, denoted by $\bar{z}$ for both cases, is shown in Fig. 5.10.

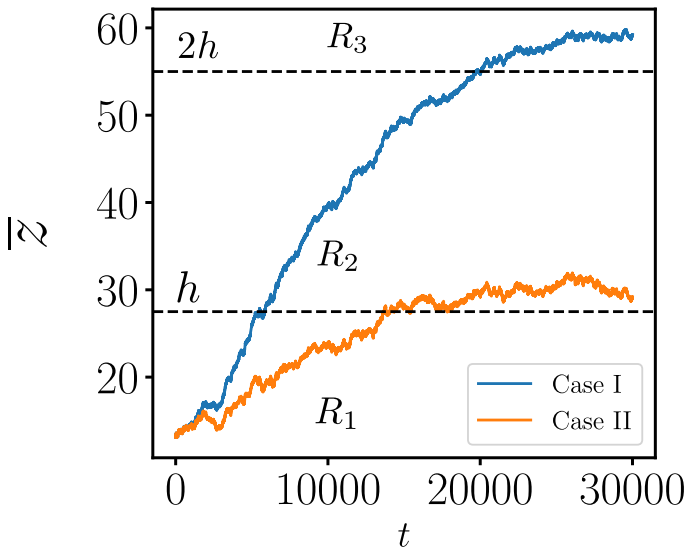

Figure 5.10: Time evolution of a chain in the presence (Case I) and absence of coordinate-dependent damping (Case II). A video illustrating the time evolution of a specific realization under both conditions is available here.

It is evident from Fig. 5.10 that under a homogeneous damping setting (case II), the polymer undergoes purely diffusive motion and meanders stochastically between regions R_1 and R_2. However, when damping is position(coordinate) dependent (case I), the polymer is entropically pulled and reaches R_3 in the same simulation time due to entropic gradient (or diffusion gradient) driven transient transport. After reaching R_3, the net transient transport ceases. It is important to note that after reaching R_3, the chain gets trapped in the region because there is an entropic barrier which opposes the transport from R_3 to R_2.
Let us emphasize what these results mean. Entropy is typically associated with spatial spreading: particles tend to diffuse from regions of confined physical space to those with larger available volume. Contrary to this expectation, we demonstrate that in systems governed by coordinate-dependent damping formulated within the Itô interpretation, it is possible for a particle or composite entity to move preferentially from a region of larger physical space to a smaller one in the complete absence of any active driving or external force. A video illustrating the time evolution of a specific realization under both conditions is available here.

Analysis of Transport Response Under Varying Damping Gradients

Now that we have established the role of the entropic (diffusion) gradient in driving transient transport, we proceed to examine the influence of varying the strength of the damping gradient (entropy gradient) on transport behavior. To isolate this effect, we remove regions R_1 and R_3 and retain only region R_2, extending its length while maintaining confinement at the boundaries. The polymer is initialized in an unfolded linear chain conformation along the z axis, fully contained within R_2 across all ensemble realizations, each corresponding to a distinct damping gradient strength. The system remains in thermal equilibrium with a heat bath at temperature T, subject to a coordinate-dependent damping profile that is linearly scaled by a parameter A.

All simulation parameters remain unchanged as shown in table 5.3 except the following: The length of region R_2, $h = 200$ and $s(z_i) = r + (h - z_i)\left(\frac{\mathcal{R}-r}{h}\right)$, while the functional form of damping $\Gamma_i = \frac{A}{s(z_i)}$ remains same.

To systematically assess the impact of the damping gradient, strength parameter A is varied, keeping $s(z_i)$ fixed. The diffusion gradient induced transient velocity $(\overline{v_z})$[1] of the system in z direction refers to the average net displacement of center of mass of particle in z direction in a specified time interval, divided by the duration of that interval, $\overline{v_z} = \overline{(z(t) - z(t_0)}/(t-t_0)$. From the diffusion current density section of this chapter, we know that the diffusion gradient transient velocity associated with i^{th} monomer is $v_i = -\frac{\partial D(z_i)}{\partial z_i}$. Using this one can easily show that $\overline{v_z} = -\frac{\partial D(\bar{z})}{\partial \bar{z}} = -\frac{k_B T}{A}\frac{ds(\bar{z})}{d\bar{z}}$. It is clear that as A increases, $\overline{v_z}$ decreases. The results shown in Fig. 5.11 are obtained by ensemble averaging over 200 independent realizations. This trend is evident in Fig. 5.11(a).

Fig. 5.11 (b) further illustrates the relationship between the transient center-of-mass velocity $\overline{v_z}$ and the inverse damping strength A^{-1}. A linear fit confirms a proportional relationship between the diffusion gradient induced transient velocity and the diffusivity strength (inverse damping strength).

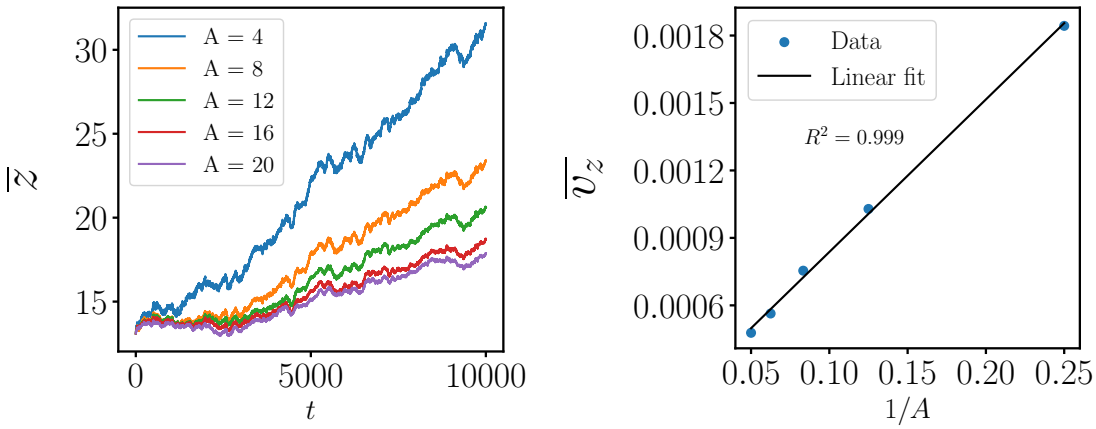

(a) (b)

Figure 5.11: Time evolution of the polymer trajectory and diffusion gradient-driven transient center-of-mass velocity in the z direction under varying damping (diffusion) gradient strengths displayed, highlighting the impact of gradient steepness on transient transport dynamics.

[1]It is actually $v_{\bar{z}}$, but we will continue to denote it as $\overline{v_z}$.

5.5 Conclusion

In this chapter, we showed that the Itô equilibrium distribution consists of the canonical Boltzmann weight and a micro-canonical-like density of states that captures the spatial inhomogeneity arising from the coordinate dependence of diffusivity. In the special case of homogeneous diffusion, this micro-canonical prefactor becomes uniform and is effectively absorbed into the normalization constant, thereby remaining hidden. We reveal how this micro-canonical part corresponds to an additional entropy source arising from coordinate-dependent damping. This additional entropy results in an emergent force of entropic origin and drives transient transport, effectively relocating particles to more constricted space even against a concentration gradient. We demonstrated how the presence of coordinate-dependent damping under the Itô formulation can create an entropic barrier that favors particle flow in one direction but blocks it in other direction, much like a diode, which we named as *diffusion diode*. Additionally, we explored how chains of particles be spontaneously *entropically pulled* from a wide region to a much narrower one under coordinate-dependent damping, a phenomenon unattainable under homogeneous diffusion. Recently experimental findings have provide unambiguous evidence of the Entropic Pulling mechanism in the context of some biological systems [71].

6

Closing Remarks and Outlook

In this chapter, we conclude the thesis by summarizing key findings and discussing future research directions.

Results

In Chapter 2, we investigated the role of asymmetry and structure by considering a symmetry-broken dimer in one-dimensional space subject to coordinate-dependent damping within the Itô framework. Despite the system being in thermal equilibrium and free of any external forces, the symmetry-broken dimer exhibits a persistent directional motion, driven purely by the asymmetry in damping across its constituent particles. This result demonstrates that spontaneous transport can arise even in equilibrium systems when internal symmetry is broken and the dissipation landscape is inhomogeneous without introducing any correlation in bath-induced thermal noise.

In Chapter 3, we extended our analysis of the symmetry-broken dimer model to include the presence of a weak external constant global force, while maintaining spatially varying damping. Our results highlight a fundamentally different mechanism of energy extraction and conversion, rooted in the internal asymmetry of the system rather than in external modulation. We identify dimer's asymmetric structure, combined with broken symmetry in presence of a homogenous, isotropic thermal noise

and an external opposing force, enables it to rectify bath fluctuations and convert it into directed motion and mechanical work, thus contributing to the efficiency of the ratcheting.

Motivated by the insights gained from the single-dimer system in one dimension in Chapter 2 under pure equilibrium conditions, we turned to the explore many-body regime in Chapter 4. We demonstrated that even in the absence of any external force or active driving, the passive system exhibits robust collective motion including directional migration, swarming, and spontaneous rotation in the presence of coordinate-dependent damping. These phenomena arise purely from equilibrium thermal fluctuations and the asymmetry embedded in the internal structure of each dimer, coupled with the spatial variation in damping. While active contributions can coexist and enhance such motion in biological contexts, our results show that passive, equilibrium driven transport can arise as a fundamental mechanism.

In Chapter 5, we uncover how a new source of entropy arises in the presence of coordinate-dependent damping, when the dynamics are interpreted within the Itô framework. This additional entropy contribution, stemming from the spatial inhomogeneity of the damping coefficient, gives rise to a transient (non-equilibrium) entropic force which controls the transport of mesoscopic objects. Two key consequences are identified: entropic pulling, where particles exhibit spontaneous transport from regions of larger physical volume to smaller ones, and the diffusion diode effect, where diffusion becomes directionally biased allowing easier transport in one direction than the reverse one, despite the absence of any external force. These phenomena have no analogue in systems with homogeneous diffusion and underscore the rich transport behavior enabled by passive dissipation inhomogeneity.

Future Research Directions

Problem 1: Crowding induced coordinate-dependent damping : An interesting direction for future research is to explore scenarios where the presence of many particles in the vicinity induces a position-dependent damping. In such systems, the local dissipation experienced by a particle is dynamically modulated by the surrounding particle density, leading to emergent coordinate depen-

dence that arises from crowding effects. It would be interesting to look at the impact on transport, structure formation and collective dynamics.

Problem 2: Compare with Active matter dynamics A direction worth exploring for future research lies in exploring hybrid systems where passive coordinate-dependent damping coexists with active driving, such as self-propelled particle. While much of the existing work focuses on either purely passive or purely active systems, the interplay between them remains largely unexplored. In particular, it would be interesting to investigate how spatially varying damping profiles can interact with active propulsion.

Appendix

A Estimation of Characteristic Timescales in Langevin Dynamics

To justify the applicability of Langevin dynamics to model Brownian motion, it is important to identify the relevant microscopic timescales governing the interaction between a Brownian particle and the surrounding fluid [72]. Two key timescales play a central role:

1. The **microscopic fluid correlation time** τ_c, which characterizes the duration over which the random force due to molecular collisions remains temporally correlated.

2. The **momentum relaxation time of the particle** ζ^{-1}, which denotes the time required for a particle's velocity to decay under viscous damping.

A clear separation between these timescales ensures the validity of the Markovian and overdamped approximations employed in construction of Langevin description.

Molecular Correlation Time τ_c

The timescale τ_c is estimated as the time taken by a fluid (say water) molecule to traverse a typical intermolecular distance $\bar{a}$, at its root mean square (RMS) thermal speed v_{RMS}:

$$\tau_c \sim \frac{\bar{a}}{v_{\text{RMS}}}$$

To estimate $\bar{a}$, we consider water at room temperature. Using the density $\rho \approx 10^3$ kg/m^3, molecular weight $M \approx 18$ g/mol, and Avogadro's number $N_A \approx 6 \times$

10^{23} mol^{-1}, the number density of water molecules is given by $n \approx \rho N_A/M$. This yields an average molecular spacing:

$$\bar{a} \approx n^{-1/3} = \left(\frac{M}{\rho N_A}\right)^{1/3} \approx 3 \times 10^{-10} \text{ m}$$

The RMS speed of a water molecule of mass $m_{\text{H}_2\text{O}} \approx 3 \times 10^{-26}$ kg is:

$$v_{\text{RMS}} = \sqrt{\frac{k_B T}{m_{\text{H}_2\text{O}}}} \approx 4 \times 10^2 \text{ m/s}$$

Combining the above estimates, we obtain:

$$\tau_c \sim \frac{3 \times 10^{-10} \text{ m}}{4 \times 10^2 \text{ m/s}} \sim 10^{-12} \text{ s}$$

This timescale characterizes how rapidly thermal noise loses its correlation. For Langevin dynamics to be valid, the random force acting on the Brownian particle must be treated as delta-correlated white noise, an assumption justified only for $t \gg \tau_c$.

Particle Relaxation Time ζ^{-1}

The relaxation time ζ^{-1} is the timescale over which a Brownian particle's velocity decays due to viscous drag. It is given by:

$$\zeta^{-1} = \frac{m}{\Gamma} = \frac{m}{6\pi\eta R}$$

Here, m is the mass of the particle, η is the viscosity of the surrounding fluid, and R is the particle radius. Assuming a spherical particle with radius $R = 1000$ nm, and the density of water $\rho = 10^3$ kg/m^3, the particle mass is:

$$m = \frac{4}{3}\pi R^3 \rho \approx 4 \times 10^{-15} \text{ kg}$$

Using the viscosity of water at room temperature, $\eta \approx 10^{-3}$ N $\cdot$ s/m^2, we estimate:

$$\zeta^{-1} \approx \frac{4 \times 10^{-15}}{6\pi \times 10^{-3} \times 10^{-6}} \sim 10^{-7} \text{ s}$$

This is significantly larger than τ_c, by approximately five orders of magnitude, confirming a well-separated timescale hierarchy.

Timescale Hierarchy and Validity of the Langevin Description

The hierarchy

$$\tau_c \ll \zeta^{-1} \ll \tau_{\text{diff}}$$

(where τ_{diff} is the diffusive timescale over which appreciable spatial displacement occurs) justifies several key approximations in Langevin modeling:

- Thermal noise can be approximated as delta-correlated white noise for $t \gg \tau_c$.
- The inertial term can be neglected in the overdamped limit for $t \gg \zeta^{-1}$.
- Genuine diffusive behavior sets in only for times $t \gg \zeta^{-1}$, after the particle velocity equilibrates.

In summary, for a consistent Langevin description, the dynamics must be probed in the regime $t \gg \zeta^{-1} \gg \tau_c$. For times shorter than τ_c, hydrodynamic memory effects and detailed molecular interactions become important, necessitating more refined microscopic models.

B Derivation of Itô distribution

Consider a Brownian particle moving in one spatial dimension x, subject to a force $F(x)$. The particle experiences position-dependent damping, denoted by $\Gamma(x)$, leading to a drift velocity $\nu(x) = \frac{F(x)}{\Gamma(x)}$. The diffusion coefficient of the particle $D(x)$ is related to it's damping by local Stoke's-Einstein relation $D(x) = \frac{k_B T}{\Gamma(x)}$, where k_B is the Boltzmann constant and T is the absolute temperature of bath.

Trajectory based approach

The stochastic dynamics of such a system, interpreted in the Itô sense, is governed by the following overdamped Langevin (or Brownian) equation:

$$\frac{dx}{dt} = \nu(x) + \sqrt{2D(x)}\eta(t), \tag{B1}$$

where $\eta(t)$ is a continuous, Markov, temporally delta correlated white noise of zero mean $\langle \eta(t) \rangle = 0$ and unit strength, and $\langle \eta_i(t_1)\eta_j(t_2) \rangle = \delta_{ij}\delta(t_1 - t_2)$.

Equation (B1) provides a trajectory-level description of the system, where individual realizations represent distinct time evolutions of the particle's position. Each realization corresponds to a specific random path that the particle follows, determined by the initial conditions and the stochastic noise term.

Probability based approach

There also exists an alternate but equivalent description. Instead of tracking the path of a single particle, the focus shifts to the probability distribution of the particle's position. This statistical approach considers the likelihood of the particle being at a given location at a specific time. It is formalized through the Fokker-Planck equation. The Fokker-Planck equation corresponding to the equation (B1) treating it as an Itô process [44, 73] is:

$$\begin{aligned} \frac{\partial}{\partial t}P(x,t) &= -\frac{\partial}{\partial x}[\nu(x)P(x,t)] + \frac{\partial^2}{\partial x^2}[D(x)P(x,t)] \\ &= -\frac{\partial}{\partial x}J(x,t) \end{aligned}$$

where $P(x,t)$ is the probability density of particle and $J(x,t) = \nu(x)P(x,t) - \frac{\partial}{\partial x}D(x)P(x,t)$, is the probability current density. The first term in $J(x,t)$ corresponds to drift current density, and the second term to diffusion current density [38, 42, 44, 52, 73–77]. Now, the equilibrium distribution is obtained by setting the total probability current to zero, that is $J(x) = 0$ (condition for detailed balance), the following equilibrium distribution $P(x)$ results:

$$P(x) \quad = \quad C\frac{D_0}{D(x)}\exp\left(\int dx\frac{\nu(x)}{D(x)}\right)$$

Here, C is a constant with dimensions of inverse length, and D_0 is the bulk diffusivity away from any interface to which $D(x)$ converges as the Brownian particle makes its excursion away from an interface. This distribution is referred to as **generalized/modified Boltzmann distribution or Itô-distribution** in [42–45]. Now, if the force $F(x)$ can be written as negative gradient of a conservative potential $U(x)$, the drift velocity takes the form: $\nu(x) = -\frac{1}{\Gamma(x)}\frac{\partial}{\partial x}U(x)$. In the presence of a conservative potential $U(x)$, the **Itô distribution** takes its most familiar form, $P(x)$ thus becomes [42, 44, 52, 58].

$$P(x) = C\frac{D_0}{D(x)}\exp\left(-\frac{U(x)}{k_BT}\right). \tag{B2}$$

This is often written in literature as:

$$P(x) = \frac{\mathcal{C}}{D(x)}\exp\left(-\frac{U(x)}{k_BT}\right).$$

where, $\mathcal{C} = CD_0$ is new normalization constant with dimensions of speed.

C Discretization of Langevin Equation as an Itô process

Continuous-Time Langevin Equation

The overdamped Langevin equation (as discussed in the preceding appendix) in the presence of coordinate-dependent damping is given by:

$$\frac{dx(t)}{dt} = \nu(x) + \sqrt{2D(x)}\,\eta(t) \tag{C1}$$

Discretizing Time and Space

Discretize continuous time into discrete steps of size Δt, so that $t_k = k\Delta t$ for $k = 0, 1, 2, 3, \ldots$. The continuous space is also a discretized space so that $x_k = x(t_k)$ and the discrete version of noise is $\eta_k = \eta(t_k)$.

We discretize continuous time as:

$$t_k = k\Delta t, \quad k = 0, 1, 2, \ldots \tag{C2}$$

We define the discrete version of continuous variables like position and noise as:

$$x_k = x(t_k), \quad \eta_k = \eta(t_k) \tag{C3}$$

Itô Discretization of the Langevin Equation

Itô disretization means that during the time evolution of equation (C1) from t_k to t_{k+1}, all functions of the position, such as the drift term $\nu(x)$ and the diffusion coefficient $D(x)$, are evaluated at the beginning of each time interval.

Therefore, the discrete-time version of the Langevin equation (C1) interpreted as Itô process is written as

$$\frac{x_{k+1} - x_k}{\Delta t} = \nu(x_k) + \sqrt{2D(x_k)}\,\eta_k$$

Discrete Delta Function Approximation

In the discrete setting, the Dirac delta function $\delta(t - t')$ is approximated as [78]:

$$\delta_{\Delta t}(t_k - t_{k'}) = \begin{cases} \frac{1}{\Delta t}, & -\frac{\Delta t}{2} < |t_k - t_{k'}| < \frac{\Delta t}{2} \\ 0, & \text{otherwise} \end{cases} \tag{C4}$$

One can verify that by defining $t = t_k - t_{k'}$, the discrete delta function $\delta_{\Delta t}(t)$ converges to the Dirac delta function in the limit $\Delta t \to 0$:

$$\lim_{\Delta t \to 0} \delta_{\Delta t}(t) = \begin{cases} \infty & \text{for } t \to 0 \\ 0 & \text{otherwise} \end{cases} \tag{C5}$$

Additionally, the integral over the delta function is normalized to unity:

$$\int_{-\infty}^{\infty} \delta_{\Delta t}(t)\, dt = 1 \tag{C6}$$

A shorthand notation for the discrete time delta function employs the Kronecker delta $\delta_{kk'}$, defined as:

$$\delta_{kk'} = \begin{cases} 1 & \text{if } k = k' \\ 0 & \text{otherwise} \end{cases} \tag{C7}$$

Thus, the discrete delta function can be expressed as:

$$\delta_{\Delta t}(t_k - t_{k'}) \approx \frac{\delta_{kk'}}{\Delta t} \tag{C8}$$

Discrete Noise Term and Scaling

The continuous-time Gaussian white noise $\eta(t)$ satisfies the correlation:

$$\langle \eta(t)\eta(t') \rangle = \delta(t - t')$$

Upon discretizing time into steps of size Δt, with discrete times $t_k = k\Delta t$, the correlation becomes

$$\langle \eta(t_k)\eta(t_{k'}) \rangle = \delta_{\Delta t}(t_k - t_{k'}) = \frac{\delta_{kk'}}{\Delta t}$$

Thus, the covariance of the discrete noise samples $\eta_k = \eta(t_k)$ is

$$\boxed{\langle \eta_k \eta_{k'} \rangle = \frac{1}{\Delta t}\, \delta_{kk'}}$$

Thus, the variance of η_k scales as:

$$\langle \eta_k^2 \rangle = \frac{1}{\Delta t} \tag{C9}$$

Thus, η_k scales as:

$$\eta_k \simeq O(\Delta t^{-1/2}).$$

Each noise sample's variance diverges as $\Delta t \to 0$

Scaling Noise for Finite Variance

The discretizations of Equation (C1) becomes

$$x_{k+1} - x_k = \nu(x_k)\, \Delta t + \sqrt{2D(x_k)} \Delta t\, \eta_k,$$

To ensure a finite variance as $\Delta t \to 0$, we define the scaled noise:

$$\xi_k = \sqrt{\Delta t}\, \eta_k$$

which satisfies

$$\langle \xi_k \rangle = 0, \quad \langle \xi_k \xi_{k'} \rangle = \delta_{kk'}.$$

$$\xi_k \sim \mathcal{N}(0, 1),$$

Thus, $\xi_k \sim \mathcal{N}(0, 1)$, i.e., ξ_k is an independent Gaussian random variable with zero mean and unit variance.

This scaling ensures that, although each noise sample's variance diverges as $\Delta t \to 0$, the integrated noise over a finite time interval remains finite. Practically, this means the noise increment $\xi_k = \sqrt{\Delta t}\, \eta_k$ has variance $\langle \xi_k^2 \rangle = 1$, preserving the correct continuous-time limit and allowing consistent numerical integration of the stochastic differential equation.

Discretized Langevin Equation

Using the scaled noise $\xi_k \sim \mathcal{N}(0,1)$, the discrete-time Langevin equation reads:

$$\boxed{x_{k+1} - x_k = \nu(x_k)\,\Delta t + \sqrt{2D(x_k)\Delta t}\,\xi_k,}$$

This discretization has been used to simulate the Itô process throughout the thesis. This is also referred to as the Euler-Maruyama discretization scheme.

D Derivation of Equilibrium distribution for Symmetry-Broken Dimer Model for an Itô Process

Consider the equation:

$$\frac{dz}{dt} = -\left(\frac{1}{\Gamma_1(z)} + \frac{1}{\Gamma_2(z)}\right)\frac{dV(z)}{dz} + \xi_z(z,t),$$

Where the noise term is :

$$\xi_z(z,t) = \sqrt{2k_BT}\left(\frac{\eta_1(t)}{\sqrt{\Gamma_1(z)}} - \frac{\eta_2(t)}{\sqrt{\Gamma_2(z)}}\right).$$

This can be rewritten as:

$$\dot{z} = h(z) + g_1(z)\eta_1(t) + g_2(z)\eta_2(t), \tag{D1}$$

With the following definitions for the functions:

$$h(z) = -\frac{dV(z)}{dz}\left(\frac{1}{\Gamma_1(z)} + \frac{1}{\Gamma_2(z)}\right), \quad g_1(z) = \sqrt{\frac{2k_BT}{\Gamma_1(z)}}, \quad g_2(z) = -\sqrt{\frac{2k_BT}{\Gamma_2(z)}}.$$

The formal solution to the stochastic differential equation is given by:

$$z(t+\tau) - z(t) = \int_t^{t+\tau} h(z(t'))\,dt' + \int_t^{t+\tau} g_1(z(t'))\,\eta_1(t')dt' + \int_t^{t+\tau} g_2(z(t'))\,\eta_2(t')dt'.$$

Suppose $z(t) \equiv y$. Now, let's Taylor expand various terms about y up to first order:

$$\begin{aligned} h(z(t')) &= h(y) + (z(t') - y) \times \tilde{h}(y), \\ g_1(z(t')) &= g_1(y) + (z(t') - y) \times \tilde{g}_1(y), \\ g_2(z(t')) &= g_2(y) + (z(t') - y) \times \tilde{g}_2(y), \end{aligned}$$

where, $\tilde{h}(y) = \left.\frac{dh(z(t'))}{dz(t')}\right|_{z(t')=y}$

$$z(t+\tau)-y=\int_t^{t+\tau}\Big(h(y)+\big(z(t')-y\big)\times\tilde{h}(y)\Big)\,dt'+\int_t^{t+\tau}\Big(g_1(y)+\big(z(t')-y\big)\times\tilde{g_1}(y)\Big)\,\eta_1(t')\,dt'$$
$$+\int_t^{t+\tau}\Big(g_2(y)+\big(z(t')-y\big)\times\tilde{g_2}(y)\Big)\,\eta_2(t')\,dt',$$

$$z(t+\tau)-y=\int_t^{t+\tau}dt'\big[h(y)+g_1(y)\eta_1(t')+g_2(y)\eta_2(t')\big]$$
$$+\int_t^{t+\tau}dt'(z(t')-y)\times\big(\tilde{h}(y)+\tilde{g}_1(y)\eta_1(t')+\tilde{g}_2(y)\eta_2(t').\big)$$

Now let us iterate $(z(t')-y)$ to first order in terms of $(z(t'')-y)$:

$$z(t+\tau)-y=\int_t^{t+\tau}dt'\big[h(y)+g_1(y)\eta_1(t')+g_2(y)\eta_2(t')\big]$$
$$+\int_t^{t+\tau}dt'\Big[\tilde{h}(y)+\tilde{g}_1(y)\eta_1(t')+\tilde{g}_2(y)\eta_2(t')\Big]\times$$
$$\Bigg(\int_t^{t'}dt''\big(h(y)+g_1(y)\eta_1(t'')+g_2(y)\eta_2(t'')\big)$$
$$+\int_t^{t'}dt''\big(\tilde{h}(y)+\tilde{g}_1(y)\eta_1(t'')+\tilde{g}_2(y)\eta_2(t'')\big)\times(z(t'')-y)\Bigg)$$

Separating term by term :

$$
\begin{aligned}
z(t+\tau)-y = & \int_t^{t+\tau} dt'\, h(y) + \int_t^{t+\tau} dt'\, \eta_1(t') g_1(y) + \int_t^{t+\tau} dt'\, \eta_2(t') g_2(y) \\
& + \int_t^{t+\tau} dt'\, \tilde{h}(y) \int_t^{t'} dt''\, h(y) + \int_t^{t+\tau} dt'\, \tilde{g}_1(y)\eta_1(t') \int_t^{t'} dt''\, g_1(y)\eta_1(t'') \\
& + \int_t^{t+\tau} dt'\, \tilde{g}_2(y)\eta_2(t') \int_t^{t'} dt''\, g_2(y)\eta_2(t'') + \int_t^{t+\tau} dt'\, \tilde{h}(y) \int_t^{t'} dt''\, g_1(y)\eta_1(t'') \\
& + \int_t^{t+\tau} dt'\, \tilde{h}(y) \int_t^{t'} dt''\, g_2(y)\eta_2(t'') + \int_t^{t+\tau} dt'\, \tilde{g}_1(y)\eta_1(t') \int_t^{t'} dt''\, h(y) \\
& + \int_t^{t+\tau} dt'\, \tilde{g}_1(y)\eta_1(t') \int_t^{t'} dt''\, g_2(y)\eta_2(t'') + \int_t^{t+\tau} dt'\, \tilde{g}_2(y)\eta_2(t') \int_t^{t'} dt''\, h(y) \\
& + \int_t^{t+\tau} dt'\, \tilde{g}_2(y)\eta_2(t') \int_t^{t'} dt''\, g_1(y)\eta_1(t'') + \text{Integrals of order } (z(t'')-y).
\end{aligned}
$$

Now, we need to evaluate

$$
\begin{aligned}
\langle z(t+\tau)-y \rangle = & \int_t^{t+\tau} dt'\, h(y) + \int_t^{t+\tau} dt'\, \langle \eta_1(t') \rangle\, g_1(y) + \int_t^{t+\tau} dt'\, \langle \eta_2(t') \rangle\, g_2(y) \\
& + \int_t^{t+\tau} dt'\, \tilde{h}(y) \int_t^{t'} dt''\, h(y) + \int_t^{t+\tau} dt'\, \tilde{g}_1(y) \int_t^{t'} dt''\, g_1(y)\, \langle \eta_1(t')\eta_1(t'') \rangle \\
& + \int_t^{t+\tau} dt'\, \tilde{g}_2(y) \int_t^{t'} dt''\, \langle \eta_2(t')\eta_2(t'') \rangle\, g_2(y) \\
& + \int_t^{t+\tau} dt'\, \tilde{h}(y) \int_t^{t'} dt''\, g_1(y)\, \langle \eta_1(t'') \rangle \\
& + \int_t^{t+\tau} dt'\, \tilde{h}(y) \int_t^{t'} dt''\, g_2(y)\, \langle \eta_2(t'') \rangle \\
& + \int_t^{t+\tau} dt'\, \tilde{g}_1(y)\, \langle \eta_1(t') \rangle \int_t^{t'} dt''\, h(y) \\
& + \int_t^{t+\tau} dt'\, \tilde{g}_1(y) \int_t^{t'} dt''\, \langle \eta_1(t')\eta_2(t'') \rangle\, g_2(y) \\
& + \int_t^{t+\tau} dt'\, \tilde{g}_2(y)\, \langle \eta_2(t') \rangle \int_t^{t'} dt''\, h(y) \\
& + \int_t^{t+\tau} dt'\, \tilde{g}_2(y) \int_t^{t'} dt''\, \langle \eta_2(t')\eta_1(t'') \rangle\, g_1(y).
\end{aligned}
$$

Using properties of Gaussian white noise: $\langle \eta_i(t) \rangle = 0$ and $\langle \eta_i(t)\eta_j(t') \rangle = \delta_{ij}\delta(t - t')$.

$$\begin{aligned} \langle z(t+\tau) - y \rangle = &\int_t^{t+\tau} dt'\, h(y) + \int_t^{t+\tau} dt' \int_t^{t'} dt''\, h(y)\, \tilde{h}(y) \\ &+ \int_t^{t+\tau} dt'\, \tilde{g}_1(y)\, g_1(y) + \int_t^{t+\tau} dt'\, \tilde{g}_2(y)\, g_2(y). \end{aligned} \tag{D2}$$

From the Kramers-Moyal expansion, we define:

$$D^{(1)}(y,t) = \lim_{\tau \to 0} \frac{1}{\tau} \langle z(t+\tau) - y \rangle.$$

The only terms in $\langle z(t+\tau) - y \rangle$ that survive are of order τ. Thus, we obtain:

$$D^{(1)}(y) = h(y) + \frac{1}{2} \left[\tilde{g_1}(y) g_1(y) + \tilde{g_2}(y) g_2(y) \right].$$

Similarly, the second Kramers-Moyal coefficient is defined as:

$$D^{(2)}(y,t) = \lim_{\tau \to 0} \frac{1}{2\tau} \left\langle \left[z(t+\tau) - y \right]^2 \right\rangle.$$

Now, instead of expanding this fully, we note that only terms of order τ will contribute to $D^{(2)}$.

A delta function in K dimensions contracts an integral with n differentials to an integral with $n - K$ differentials ($n \geq K$).

Thus, integrals of the form

$$\int_t^{t+\tau} dt' \int_t^{t'} dt''\, \delta(t' - t''),$$

which initially involves two differentials, will reduce to a single-variable integral due to the presence of one delta function. This remaining integral is of order τ and contributes to $D^{(2)}$.

Now, consider the integrals of the form:

$$\int_t^{t+\tau} dt' \int_t^{t'} dt'' \int_t^{t'} dt'''\, \langle \eta_i(t')\eta_i(t'')\eta_i(t''') \rangle,$$

which vanish by Wick's theorem.

However, we also encounter integrals of the form:

$$\int_t^{t+\tau} dt' \int_t^{t'} dt'' \int_t^{t''} dt''' \int_t^{t'''} dt'''' \, \langle \eta_i(t')\eta_i(t'')\eta_i(t''')\eta_i(t''''), \rangle$$

which, by Wick's theorem, do not vanish. We obtain the sum of the products of two-term pairings for all possible combinations. However, for each product of pairs, we eventually get a product of two delta functions in the four-variable integral, which contracts it to a two-variable integral of order τ^2. Hence, these terms do not contribute to $D^{(2)}$.

Therefore, we can write:

$$D^{(2)}(y,t) = \lim_{\tau\to 0} \frac{1}{2\tau} \left\langle [z(t+\tau) - y]^2 \right\rangle = \frac{1}{2} \left[g_1(y)^2 + g_2(y)^2 \right].$$

Evaluating the expectation value:

$$\langle z(t+\tau) - y \rangle = \int_t^{t+\tau} dt' h(y) + \frac{1}{2}\big(\tilde{g}_1(y) g_1(y) + \tilde{g}_2(y) g_2(y)\big). \tag{D3}$$

For the second Kramers-Moyal coefficient:

$$D^{(2)}(y,t) = \frac{1}{2}\big(g_1(y)^2 + g_2(y)^2\big). \tag{D4}$$

The corresponding Fokker-Planck equation is given by:

$$\frac{\partial P(y,t)}{\partial t} = -\frac{\partial}{\partial y}\big(h(y)P(y,t)\big) + \frac{\partial^2}{\partial y^2}\big(D(y)P(y,t)\big), \tag{D5}$$

where the diffusion coefficient is:

$$D(y) = \frac{1}{2}\big(g_1(y)^2 + g_2(y)^2\big) = D_1(y) + D_2(y), \tag{D6}$$

and

$$D_1(y) = \frac{1}{2} g_1^2(y) = \frac{k_B T}{\Gamma_1(y)}, \quad D_2(y) = \frac{1}{2} g_2^2(y) = \frac{k_B T}{\Gamma_2(y)}$$

Now, the stochastic equation corresponds to an overdamped Fokker-Planck equation given by:

$$\frac{\partial P(y,t)}{\partial t} = -\frac{\partial}{\partial y}\big[D^{(1)}(y,t)P(y,t)\big] + \frac{\partial^2}{\partial y^2}\big[D^{(2)}(y,t)P(y,t)\big]. \tag{D7}$$

Substituting the expressions for $D^{(1)}(y)$ and $D^{(2)}(y)$, we obtain:

$$\frac{\partial P(y,t)}{\partial t} = -\frac{\partial}{\partial y}\big[h(y)P(y,t)\big] + \frac{1}{2}\frac{\partial^2}{\partial y^2}\Big[\big(g_1^2(y) + g_2^2(y)\big)P(y,t)\Big]. \tag{D8}$$

Note that the spurious term arises as a consequence of the Stratonovich convention. This term has been accounted for by adding $-\frac{1}{2}\Big[\tilde{g_1}(y)g_1(y) + \tilde{g_2}(y)g_2(y)\Big]$ to the overdamped Fokker-Planck equation.

Now, let us define the diffusion coefficient:

$$D(y) \equiv D^{(2)}(y,t) = \frac{1}{2}\big[g_1^2(y) + g_2^2(y)\big]. \tag{D9}$$

Thus, the Fokker-Planck equation can be expressed as:

$$\frac{\partial P(z,t)}{\partial t} = -\frac{\partial}{\partial z}\left[h(z)P(z,t) - \frac{\partial\big[D(z)P(z,t)\big]}{\partial z}\right] = -\frac{\partial J(z,t)}{\partial z}, \tag{D10}$$

where $J(z,t)$ is the probability current.

The Fokker-Planck becomes:

$$\frac{\partial P(z,t)}{\partial t} = -\frac{\partial}{\partial z}\left[-\frac{dV(z)}{dz}\left(\frac{1}{\Gamma_1(z)} + \frac{1}{\Gamma_2(z)}\right)P(z,t) - \frac{\partial\big[D(z)P(z,t)\big]}{\partial z}\right] = -\frac{\partial J(z,t)}{\partial z}. \tag{D11}$$

In Chapter 3, we have the following equation.

$$\frac{dz}{dt} = \Big[F\frac{\Gamma_2(z) - \Gamma_1(z)}{\Gamma_2(z) + \Gamma_1(z)} - \frac{dV(z)}{dz}\Big]\left[\frac{1}{\Gamma_1(z)} + \frac{1}{\Gamma_2(z)}\right] + \xi_z(z,t).$$

with

$$h(z) = \Big[F\frac{\Gamma_2(z) - \Gamma_1(z)}{\Gamma_2(z) + \Gamma_1(z)} - \frac{dV(z)}{dz}\Big]\left[\frac{1}{\Gamma_1(z)} + \frac{1}{\Gamma_2(z)}\right],$$

$$\frac{\partial P(z,t)}{\partial t} = -\frac{\partial}{\partial z}\left[\left(F\frac{\Gamma_2(z)-\Gamma_1(z)}{\Gamma_2(z)+\Gamma_1(z)} - \frac{dV(z)}{dz}\right)\left[\frac{1}{\Gamma_1(z)}+\frac{1}{\Gamma_2(z)}\right]P(z,t) - \frac{\partial\big[D(z)P(z,t)\big]}{\partial z}\right]. \tag{D12}$$

E Symmetry-broken dimer in one dimension with sigmoidal damping

In this appendix, we present the details corresponding to the one-dimensional case of a single symmetry-broken dimer considered in Chapter 4. The dimer is confined to motion along the x axis with constituent coordinates $x_1 > x_2$, with $z = x_1 - x_2$, interaction potential $V(z) = \frac{\alpha}{2}(z - z_{min})^2$, and constituent coordinate-dependent damping described by sigmoidal profiles given by:

$$\Gamma_i(z) = \frac{a_i}{1 + \exp[-\lambda(z - z_{\min})]} + b_i,$$

as shown in Fig.1. Note that there are no inter-dimer forces because we only have a single dimer. Moreover, no confinement interaction is present.

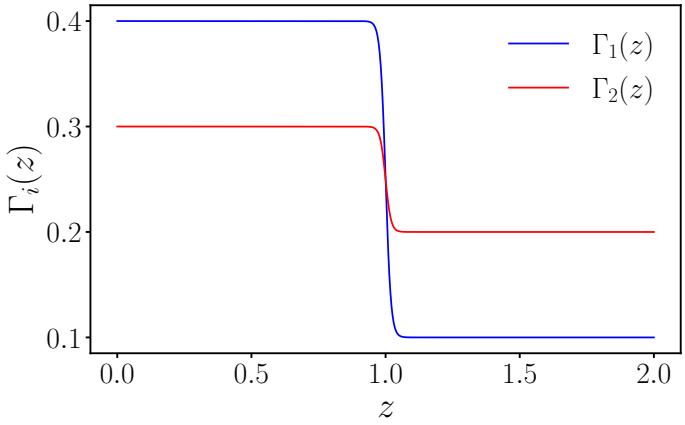

Figure 1: Variation of damping coefficient as a function of the internal coordinate for both constituents is displayed. $\Gamma_1(z) \neq \Gamma_2(z)$ corresponds to Broken symmetry. The parameters used are: $a_1 = -0.3$, $b_1 = 0.4$ and $a_2 = -0.1$, $b_2 = 0.3$, $\lambda = 100$ and $z_{min} = 1$.The interaction strength $\alpha = 200$ and time step $\Delta t = 10^{-5}$ is used in the simulation.

Corresponding to this sigmoidal damping profile, the results are displayed in Fig. 2. The simulation shows excellent agreement with the theoretically predicted probability density for the configuration coordinate, as illustrated in Fig. 2(a). Fig. 2(b) depicts how the average center-of-mass velocity of the dimer increases with temperature, while all other parameters are kept fixed. This indicates that the spontaneous rectified motion becomes stronger with increasing thermal energy.

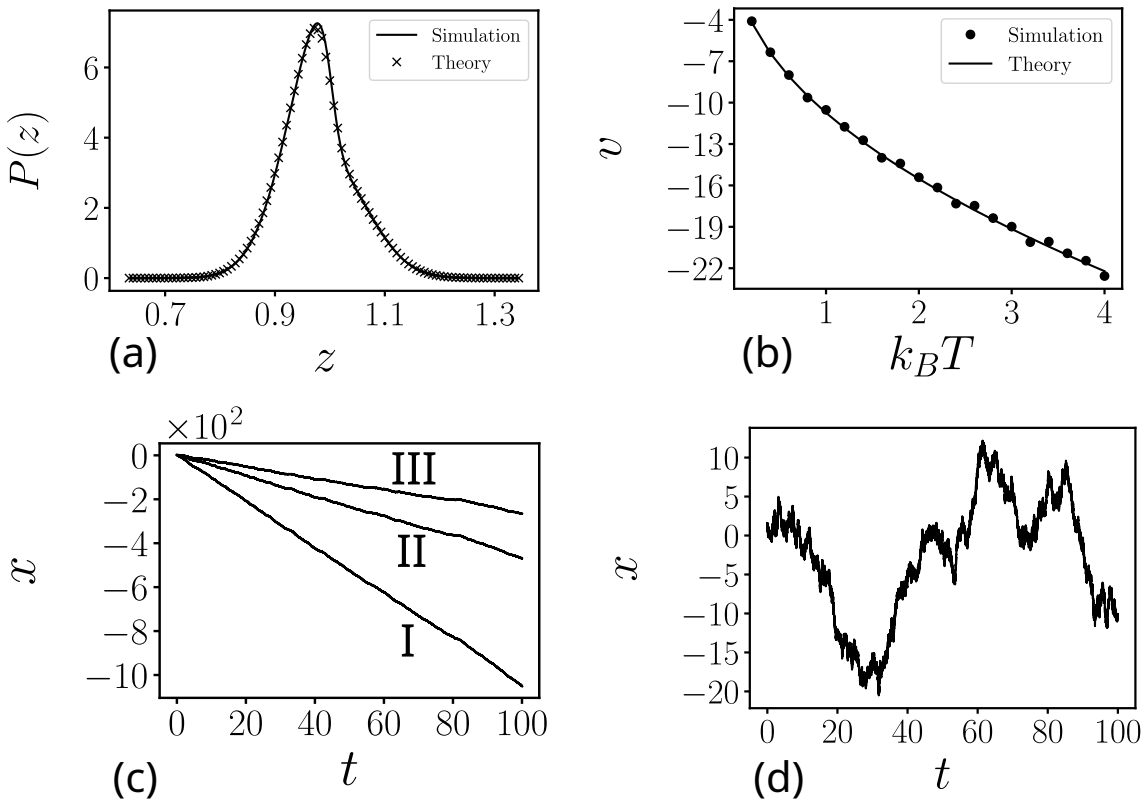

Figure 2: (a) Itô distributed configuration coordinate for a symmetry broken dimer. (b) The average CM speed of the dimer increases with thermal energy. (c) Symmetry broken dimers showing rectified transport for three different damping parameters The damping determining parameters corresponding to I, II and III are $b_1 = 0.4$, $b_2 = 0.3$; $b_1 = 0.5$, $b_2 = 0.4$ and $b_1 = 0.6$, $b_2 = 0.5$ respectively. (d) Symmetric dimer with equal damping coefficients, $a_1 = a_2 = -0.3$ and $b_1 = b_2 = 0.4$ showing no net directed motion.

In Fig. 2(c), the motion of center of mass motion is analysed for three different damping profiles. For all three cases, $a_1 = -0.3$ and $a_2 = -0.1$ are fixed and b_1 and b_2 are varied. The damping determining parameters corresponding to I, II and III in Fig. 2(c) are $b_1 = 0.4$, $b_2 = 0.3$; $b_1 = 0.5$, $b_2 = 0.4$ and $b_1 = 0.6$, $b_2 = 0.5$ respectively. These choices correspond to an overall increase in the damping experienced by the dimer from I to III, resulting in the largest center-of-mass displacement for I and the smallest for III over the same time interval. Fig. 2(d) presents the motion of center-of-mass motion in a symmetry-unbroken case with $a_1 = a_2 = -0.3$ and $b_1 = b_2 = 0.4$. As expected, no net motion is observed in this configuration.

Bibliography

[1] R. Brown, "Xxvii. a brief account of microscopical observations made in the months of june, july and august 1827, on the particles contained in the pollen of plants; and on the general existence of active molecules in organic and inorganic bodies", The philosophical magazine **4**, 161 (1828).

[2] A. Einstein et al., "On the motion of small particles suspended in liquids at rest required by the molecular-kinetic theory of heat", Annalen der physik **17**, 208 (1905).

[3] A. Einstein, *Investigations on the theory of the brownian movement* (Courier Corporation, 1956).

[4] J. Piasecki, "Centenary of MARIAN SMOLUCHOWSKI'S theory of brownian motion.", Acta Physica Polonica B **38** (2007).

[5] M. Von Smoluchowski, "Zur kinetischen theorie der brownschen molekularbewegung und der suspensionen", Annalen der physik **326**, 756 (1906).

[6] M. Smoluchowski, "Sur le chemin moyen parcouru par les molécules d'un gaz et sur son rapport avec la théorie de la diffusion", Pisma Mariana Smoluchowskiego **1**, 479 (1924).

[7] M. Smoluchowski, *Essai d'une théorie cinétique du mouvement brownien et des milieux troubles* (Acad. Litterarum Cracoviensis, 1906).

[8] M. Smoluchowski, "The kinetic theory of brownian molecular motion and suspensions", Ann. Phys **21**, 756 (1906).

[9] P. Langevin et al., "Sur la théorie du mouvement brownien", CR Acad. Sci. Paris **146**, 530 (1908).

[10] D. S. Lemons and A. Gythiel, "Paul Langevin's 1908 paper"on the theory of brownian motion"["sur la théorie du mouvement brownien,"cr acad. sci.(paris) 146, 530-533 (1908)]", American Journal of Physics **65**, 1079 (1997).

[11] C. W. Gardiner et al., *Handbook of stochastic methods*, Vol. 3 (springer Berlin, 1985).

[12] J. Perrin, "Mouvement brownien et réalité moléculaire", (1909).

[13] J. Perrin, "Mouvement brownien et molécules", J. Phys. Theor. Appl. **9**, 5 (1910).

[14] J. Perrin, *Brownian movement and molecular reality* (Courier Corporation, 2013).

[15] S. G. Brush, "A history of random processes: i. brownian movement from brown to perrin", Archive for history of exact sciences **5**, 1 (1968).

[16] G. E. Smith and R. Seth, *Brownian motion and molecular reality* (Oxford University Press, 2020).

[17] N. Pottier, *Nonequilibrium statistical physics: linear irreversible processes* (Oxford University Press, 2009).

[18] F. Reif, *Fundamentals of statistical and thermal physics* (Waveland Press, 2009).

[19] Y. Pomeau and J. Piasecki, "The langevin equation", Comptes Rendus. Physique **18**, 570 (2017).

[20] S. J. Blundell and K. M. Blundell, *Concepts in thermal physics* (Oup Oxford, 2010).

[21] V. Balakrishnan, *Elements of nonequilibrium statistical mechanics*, Vol. 3 (Springer, 2008).

[22] R. Kubo, "The fluctuation-dissipation theorem", Reports on progress in physics **29**, 255 (1966).

[23] A. Bhattacharyay, "Brownian motion near a wall: the dilemma of itô or stratonovich", Journal of Physics A: Mathematical and Theoretical (2025).

[24] L. P. Faucheux and A. J. Libchaber, "Confined brownian motion", Physical Review E **49**, 5158 (1994).

[25] G. Batchelor, "Brownian diffusion of particles with hydrodynamic interaction", Journal of Fluid Mechanics **74**, 1 (1976).

[26] E. M. Purcell, "Life at low reynolds number", American journal of physics **45**, 3 (1977).

[27] E. M. Purcell, "The efficiency of propulsion by a rotating flagellum", Proceedings of the National Academy of Sciences **94**, 11307 (1997).

[28] K. Lan, N. Ostrowsky, and D. Sornette, "Brownian dynamics close to a wall studied by photon correlation spectroscopy from an evanescent wave", Physical review letters **57**, 17 (1986).

[29] M. Feitosa and O. Mesquita, "Wall-drag effect on diffusion of colloidal particles near surfaces: a photon correlation study", Physical Review A **44**, 6677 (1991).

[30] P. Sharma, S. Ghosh, and S. Bhattacharya, "A high-precision study of hindered diffusion near a wall", Applied Physics Letters **97** (2010).

[31] K. Kasahara and T. Saiki, "Evaluation of influence of anisotropic diffusion near a wall in near-field fluorescence correlation spectroscopy of nanoparticles", Optical review **18**, 237 (2011).

[32] P. Holmqvist, J. K. Dhont, and P. R. Lang, "Colloidal dynamics near a wall studied by evanescent wave light scattering: experimental and theoretical improvements and methodological limitations", The Journal of chemical physics **126** (2007).

[33] P. E. Protter, *Stochastic integration and differential equations*, 2004.

[34] B. Oksendal, *Stochastic differential equations: an introduction with applications* (Springer Science & Business Media, 2013).

[35] C. Escudero and H. Rojas, "Itô vs Hänggi-Klimontovich", Physica Scripta **100**, 125241 (2025).

[36] M. Matse, "State-dependent diffusion of brownian particles near a boundary wall", (2015).

[37] A. W. Lau and T. C. Lubensky, "State-dependent diffusion: thermodynamic consistency and its path integral formulation", Physical Review E—Statistical, Nonlinear, and Soft Matter Physics **76**, 011123 (2007).

[38] A. Bhattacharyay, "Equilibrium with coordinate dependent diffusion: comparison of different stochastic processes", arXiv preprint arXiv:2309.06567 (2023).

[39] H. Risken and H. Risken, *Fokker-planck equation* (Springer, 1996).

[40] T. Yamada and S. Watanabe, "On the uniqueness of solutions of stochastic differential equations", Journal of Mathematics of Kyoto University **11**, 155 (1971).

[41] C. Escudero, "Fluctuation-dissipation relation, Maxwell-Boltzmann statistics, equipartition theorem, and stochastic calculus", Physica Scripta **98**, 055214 (2023).

[42] R. Maniar and A. Bhattacharyay, "Random walk model for coordinate-dependent diffusion in a force field", Physica A: Statistical Mechanics and its Applications **584**, 126348 (2021).

[43] A. Dhawan and A. Bhattacharyay, "Itô–distribution from gibbs measure and a comparison with experiment", Physica A: Statistical Mechanics and its Applications, 129599 (2024).

[44] A. Bhattacharyay, "Equilibrium of a brownian particle with coordinate dependent diffusivity and damping: generalized boltzmann distribution", Physica A: Statistical Mechanics and its Applications **515**, 665 (2019).

[45] A. Bhattacharyay, "Generalization of stokes–einstein relation to coordinate dependent damping and diffusivity: an apparent conflict", Journal of Physics A: Mathematical and Theoretical **53**, 075002 (2020).

[46] M. Sharma, A. Singh, and A. Bhattacharyay, "A model of thermophoresis of colloidal proteins in water using non-fickian diffusion currents", arXiv preprint arXiv:2602.13328 (2026).

[47] C. Escudero and C. Manada, "Itô versus Stratonovich in a stochastic cosmological model", Letters in Mathematical Physics **112**, 12 (2022).

[48] W. Hwang and M. Karplus, "Structural basis for power stroke vs. brownian ratchet mechanisms of motor proteins", Proceedings of the National Academy of Sciences **116**, 19777 (2019).

[49] P. Reimann, "Brownian motors: noisy transport far from equilibrium", Physics reports **361**, 57 (2002).

[50] R. D. Astumian, "Thermodynamics and kinetics of a brownian motor", science **276**, 917 (1997).

[51] A. Bhattacharyay, "Directed transport in equilibrium: a model study", Physica A: Statistical Mechanics and its Applications **391**, 1111 (2012).

[52] M. Sharma and A. Bhattacharyay, "Conversion of heat to work: an efficient inchworm", Physica Scripta **95**, 105004 (2020).

[53] M. D. Carbajal-Tinoco, R. Lopez-Fernandez, and J. L. Arauz-Lara, "Asymmetry in colloidal diffusion near a rigid wall", Physical review letters **99**, 138303 (2007).

[54] N. G. Van Kampen, "Itô versus Stratonovich", Journal of Statistical Physics **24**, 175 (1981).

[55] A. Dhawan and A. Bhattacharyay, "Thermal equilibrium of a brownian particle with coordinate dependent diffusion: comparison of boltzmann and modified boltzmann distributions with experimental results", arXiv preprint arXiv:2207.01228 (2022).

[56] A. Bhattacharyay, "Physical interpretation of Itô–distribution on the basis of local measurement of diffusion", arXiv preprint arXiv:2209.00995 (2022).

[57] R. P. Feynman, R. B. Leighton, M. Sands, and E. M. Hafner, "The feynman lectures on physics; vol. i", American Journal of Physics **33**, 750 (1965).

[58] M. Sharma and A. Bhattacharyay, "Spontaneous collective transport in a heat-bath", Physica A: Statistical Mechanics and its Applications **626**, 129082 (2023).

[59] T. Vicsek, A. Czirók, E. Ben-Jacob, I. Cohen, and O. Shochet, "Novel type of phase transition in a system of self-driven particles", Physical review letters **75**, 1226 (1995).

[60] H. Chaté, F. Ginelli, G. Grégoire, F. Peruani, and F. Raynaud, "Modeling collective motion: variations on the vicsek model", The European Physical Journal B **64**, 451 (2008).

[61] A. Cavagna, L. Del Castello, I. Giardina, T. Grigera, A. Jelic, S. Melillo, T. Mora, L. Parisi, E. Silvestri, M. Viale, et al., "Flocking and turning: a new model for self-organized collective motion", Journal of Statistical Physics **158**, 601 (2015).

[62] F. Alaimo, S. Praetorius, and A. Voigt, "A microscopic field theoretical approach for active systems", New Journal of Physics **18**, 083008 (2016).

[63] J. Löber, F. Ziebert, and I. S. Aranson, "Collisions of deformable cells lead to collective migration", Scientific reports **5**, 1 (2015).

[64] T. Hiraoka, T. Shimada, and N. Ito, "Collective motion in repulsive self-propelled particles in confined geometries", in Journal of physics: conference series, Vol. 921, 1 (IOP Publishing, 2017), p. 012006.

[65] D. A. Foster, R. Petrosyan, A. G. Pyo, A. Hoffmann, F. Wang, and M. T. Woodside, "Probing position-dependent diffusion in folding reactions using single-molecule force spectroscopy", Biophysical journal **114**, 1657 (2018).

[66] K. Neupane, F. Wang, and M. Woodside, "Direct measurement of sequence-dependent transition path times and conformational diffusion in dna duplex formation", Biophysical Journal **112**, 471a (2017).

[67] T. Cellmer, E. R. Henry, J. Hofrichter, and W. A. Eaton, "Measuring internal friction of an ultrafast-folding protein", Proceedings of the National Academy of Sciences **105**, 18320 (2008).

[68] B. Lin, J. Yu, and S. A. Rice, "Direct measurements of constrained brownian motion of an isolated sphere between two walls", Physical review E **62**, 3909 (2000).

[69] J. Noguchi, T. Hayama, S. Watanabe, H. Ucar, S. Yagishita, N. Takahashi, and H. Kasai, "State-dependent diffusion of actin-depolymerizing factor/cofilin underlies the enlargement and shrinkage of dendritic spines", Scientific reports **6**, 32897 (2016).

[70] M. Sharma and A. Bhattacharyay, "Entropic pulling and diffusion diode in an Itô process", Physics Letters A, 130709 (2025).

[71] V. Rukes, M. E. Rebeaud, L. W. Perrin, P. De Los Rios, and C. Cao, "Single-molecule evidence of entropic pulling by hsp70 chaperones", Nature Communications **15**, 8604 (2024).

[72] S. Dattagupta, *Diffusion: formalism and applications* (Taylor & Francis, 2013).

[73] L. Peliti and S. Pigolotti, *Stochastic thermodynamics: an introduction* (Princeton University Press, 2021).

[74] F. Sattin, "Fick's law and Fokker–Planck equation in inhomogeneous environments", Physics Letters A **372**, 3941 (2008).

[75] M. Bengfort, H. Malchow, and F. M. Hilker, "The Fokker–Planck law of diffusion and pattern formation in heterogeneous environments", Journal of mathematical biology **73**, 683 (2016).

[76] F. Vázquez and F. Márkus, "Non-Fickian particle diffusion in confined plasmas and the transition from diffusive transport to density waves propagation", Physics of Plasmas **17** (2010).

[77] B. P. Van Milligen, P. Bons, B. A. Carreras, and R. Sanchez, "On the applicability of Fick's law to diffusion in inhomogeneous systems", European journal of physics **26**, 913 (2005).

[78] L. F. Cugliandolo, "Introduction to langevin stochastic processes", Advances in Physics **73**, 3 (2024).